Plasma-beta effects on the island divertor of Wendelstein 7-X

Inaugural-Dissertation

zur Erlangung des Doktorgrades
der Mathematisch-Naturwissenschaftlichen Fakultät
der Heinrich-Heine-Universität Düsseldorf

vorgelegt von

Alexander Knieps
aus Bonn

Düsseldorf, November 2020

aus dem Institut für Laser- und Plasmaphysik
der Heinrich-Heine-Universität Düsseldorf

Gedruckt mit der Genehmigung der
Mathematisch-Naturwissenschaftlichen Fakultät der
Heinrich-Heine-Universität Düsseldorf

Berichterstatter:

1. Prof. Dr. Yunfeng Liang

2. Prof. Dr. Georg Pretzler

Tag der mündlichen Prüfung: 19.01.2021

Zusammenfassung

Das wesentliche Ziel des Wendelstein 7-X Stellaratorexperiments ist die Demonstration von Dauerstrichbetrieb mit Hochleistungsplasmen vergleichbar mit denen eines ähnlich großen Tokamaks. Zur Unterstützung der Szenarioentwicklung im Zuge der bevorstehenden Langpuls-Kampagne wurden drei seiner magnetischen Konfigurationen (Die "Standard"-, "High-Iota"- und "Low-Iota"-Konfiguration) auf ihre Empfindlichkeit gegenüber Plasma-Beta-Effekten auf ihren Randmagnetfeldtopologie untersucht. Diese Untersuchung studierte, mittels Anwendung des HINT-Codes, die Empfindlichkeit der Randfelder gegenüber Änderungen des zentralen und des volumengemittelten Plasmabetas (bis hin zu Werten von 5% respektive 2.5%). Anschließend wurden, basierend auf den Gleichgewichtsrechnungen, die zu erwartenden Effekte auf die Divertor-Wärmelasten mit einem Feldlinien-Diffusions-Code simuliert.

Laut den Simulation ist die magnetische Standardkonfiguration, in Bezug auf den Hoch-Beta-Betrieb, die vielversprechendste der drei untersuchten Kandidatinnen. Selbst in den berechneten Szenarien mit höchstem Beta bleibt in dieser Konfiguration die Magnetfeldtopologie des Inseldivertors erhalten. In der "High-Iota"-Konfiguration dagegen geht diese Struktur aufgrund von Randschichtstochastisierung verloren. Dieses Phänomen wird von punktuellen Wärmelastspitzen auf plasmaexponierten Teilen außerhalb des Divertors begleitet. In der "Low-Iota"-Konfiguration dagegen werden die $^5/_6$-Divertorinseln mit zunehmendem volumengemittelten Beta verkleinert, was einen Übergang in eine limiterartige Konfiguration nach sich zieht. Dieser Übergang wird von beträchtlichen Wärmelasten außerhalb der Divertorprallplatte, sowie von einem Wechsel der Wärmelastform auf der Prallplatte von einer divertor-typischen Linienform zu einer Limiter-artigen Kreisform, begleitet.

Die Gleichgewichtsrechnungen wurden auf drei Arten in Standardkonfiguration validiert. Zum einen wurde das berechnete Magnetfeld mit den Messungen einer eigens zu diesem Zweck entwickelten verfahrbaren Magnetsonde verglichen. Zum anderen wurde die 3D-Druckverteilung des berechneten Gleichgewichts mit experimentell gemessenen Profilen der Elektronen- und Ionen-Plasmaparameter verglichen. Zu diesem Zweck wurde ein neuartiges, mit Machine-Learning-Methoden arbeitendes, Verfahren entwickelt, welches die Messpunkte in eine Profilkoordinate abbildet, die mit der Struktur der Wendelstein 7-X-Randinseln übereinstimmt. Zu guter Letzt wurden die Wärmelastsimulationen direkt mit Infrarot-Kamera-Messungen der Divertor-Wärmelasten im Experimentbetrieb verglichen.

Synopsis

The Wendelstein 7-X Stellarator experiment aims to demonstrate steady-state operation in high-performance plasmas comparable to similarly-sized Tokamaks. To support the scenario development for its up-coming long-pulse campaign, three of its magnetic configurations (the standard-, high-iota- and low-iota- configuration) were investigated for their susceptibility to plasma-beta driven effects on their edge magnetic field topology. This investigation, performed using the HINT code, studies the edge magnetic field sensitivity against changes in both central and volume-averaged plasma beta (up to 5% and 2.5%, respectively). Based on the calculated equilibria, expected effects on the divertor heat-loads were then simulated with a field-line diffusion code.

Simulations indicate that the standard magnetic configuration is the most promising of the

three candidate configurations for high-beta operation. In the standard configuration, the island divertor topology prevails even in the highest-beta cases. Conversely, in the high-iota configuration, the island magnetic surface structure is lost due to stochastization in the edge, a phenomenon accompanied by hot-spots on plasma-facing components outside the divertor. In the low-iota configuration, the $^5/_6$ divertor islands were found to shrink away with increasing volume-averaged beta, resulting in a transition towards a limiter-like edge configuration. This transition is accompanied by substantial heat-loads outside of the main divertor plate, as well as a transition from the strike-line pattern typical for a divertor configuration towards a limiter-like heat spot on the main divertor target.

The validity of the finite-beta calculation was benchmarked experimentally in the standard configuration by three approaches. Firstly, the calculated magnetic fields were compared to direct magnetic field measurements performed with a purpose-built reciprocating magnetic probe. Secondly, the 3D equilibrium pressure distribution was compared to experimental profile measurements for electron and ion plasma parameters. For this purpose, a novel machine-learning-based system was developed to map the diagnostic observations onto flux surface labels compatible with the edge island structure of Wendelstein 7-X. Finally, the heat-load simulations were directly compared to infra-red camera measurements of the divertor heat-loads.

Declaration of authorship

I declare that the work in this dissertation was conducted in accordance with the requirements of the University's Regulations and Code of Practice for Research Degree Programmes and that it has not been submitted for any other academic award. Except where indicated by specic references in the text, the work is the candidate's own work.Work done in collaboration with, or with the assistance of, others, is indicated as such. Any views expressed in the dissertation are those of the author.

Date / location: _____ Signature: _____

Publications

As corresponding author

- Subsection 4.6.1.2,4.6.2,4.6.3 and 5.1.2 have been previously published in [1]. In this publication, the thesis author was responsible for the design and the calibration of the magnetic probe system inside the combined probe.
- Chapter 6 and section 5.3 as well as figures 1.6, 1.5 and 1.7 have been submitted to Nuclear Fusion under the title "Plasma beta effects on the edge magnetic field structure and divertor heat-loads in Wendelstein 7-X high-performance scenarios".

As co-author

- The papers [2, 3, 4, 5] all present SOL measurements obtained with manipulator probes during the divertor campaigns OP1.2a and OP1.2b. The author of this thesis has made technical contributions in the form of manipulator operation (a task shared among all members of the MPM team). Additionally, the author has participated in the design process for the manipulator probes presented therein (with the exception of the IPP-FLUC1 and the RFX-HRP probes) and in the maintenance of the manipulator diagnostics (although these responsibilities were primarily fulfilled by engineers).

References

[1] A. Knieps et al. "Design and characteristics of a low-frequency magnetic probe for magnetic profile measurements at Wendelstein 7-X". In: *Review of Scientific Instruments* 91.7 (2020), p. 073506. DOI: 10.1063/5.0002193.

[2] P. Drews et al. "Edge plasma measurements on the OP 1.2a divertor plasmas at W7-X using the combined probe". In: *Nuclear Materials and Energy* 19 (May 2019), pp. 179–183. DOI: 10.1016/j.nme.2019.02.012.

[3] Carsten Killer et al. "Characterization of the W7-X scrape-off layer using reciprocating probes". In: *Nuclear Fusion* 59.8 (June 2019), p. 086013. DOI: 10.1088/1741-4326/ab2272.

[4] J. Cai et al. "A new multi-channel Mach probe measuring the radial ion flow velocity profile in the boundary plasma of the W7-X stellarator". In: *Review of Scientific Instruments* 90 (Mar. 2019), p. 033502. DOI: 10.1063/1.5054279.

[5] P. Drews et al. “Operation of probe heads on the Multi-Purpose-Manipulator at W7-X in OP 1.2a”. In: *Fusion Engineering and Design* 146 (2019). SI:SOFT-30, pp. 2353–2355. ISSN: 0920-3796. DOI: https://doi.org/10.1016/j.fusengdes.2019.03.188.

List of Figures

Nomenclature

β_{ax} Axial beta or central beta

β_{vol} Volume-averaged beta

$\Delta^{\star}$ Grad-Shafranov elliptic operator

$\bar{f}$ Average value

ι Rotational transform

ψ Poloidal magnetic flux

$D^{\mu\nu}$ Contravariant electromagnetic displacement field density

$F_{\mu\nu}$ Covariant electromagnetic field-strength tensor

G Normalized toroidal field rB_{ϕ}

$g^{\mu\nu}$ Contravariant (inverse) metric tensor

$g_{\mu\nu}$ Covariant metric tensor

j^{μ} Contravariant current density

n_e electron density

n_I ion density

LCFS Last closed flux-surface

MHD Magneto-Hydrodynamics

MPM Multi-Purpose-Manipulator

XICS X-Ray Imaging Crystal Spectrometer

Contents

1 Introduction

Personally, I would believe nuclear fusion rightfully deserves its nickname as the "holy grail of energy production". It promises to deliver tremendous amounts of power derived from fuel available in abundance. Deuterium can be found in one in ten-thousand water molecules[1], while Tritium can be bred from Lithium inside the reactor [2]. A single fusion reaction releases over 17 MeV of energy [3]. A single ton of fusion fuel could therefore yield over 320 PJ of power, enough to power the entire city of Berlin for over a year ([4, pages 8/9 and 13] determines the annual primary energy consumption of Berlin at 270 PJ). The sheer abundance of available raw fuel, coupled with a waste-free fuel cycle (as Helium is an industrially highly useful element), makes nuclear fusion a highly attractive option in future energy production mixes.

1.1 Achieving a Self-Sustaining Burn: The Triple Product

In order to fuse, the reacting nuclei must first overcome the electrical Coulomb potential pushing them apart. Once sufficiently close, attractive nuclear forces, which are as strong as they are short-ranged, take over and merge them into a new nucleus. As the repulsive force grows with charge, hydrogen isotopes are the primary candidates for fusion at achievable temperatures. Since the nuclear force takes over easier when fusing larger nuclei (at an identical charge) due to the increased distance between the charged protons, higher neutron counts facilitate the fusion process. Out of those fusion processes producing a stable isotope, the most readily achievable one is the *Deuterium-Tritium* fusion process ($\mathrm{H}^2 + \mathrm{H}^3 \rightarrow \mathrm{He}^{5\star} \rightarrow \mathrm{He}^4 + \mathrm{n}$).

The likelihood of a nuclear reaction is characterized by its *cross-section* σ, an area-like quantity. If a test particle were to travel through a gas of target particles with density n at velocity v, the rate of fusion reactions would be given as $R = nv\sigma$. In a thermalized gas, the velocity is a random variable, and the cross-section is dependent on it. Therefore, only the mean rate can be calculated as $\langle R \rangle = n \langle \sigma(v) v \rangle$. In the technically accessible regime around 10 keV, the fusion rate coefficient $\langle \sigma(v) v \rangle$ (see figure 1.1) can be approximated as a quadratic function of the temperature, which gives the approximate fusion power as

$$P_{\text{fusion}} = \alpha n N T^2$$

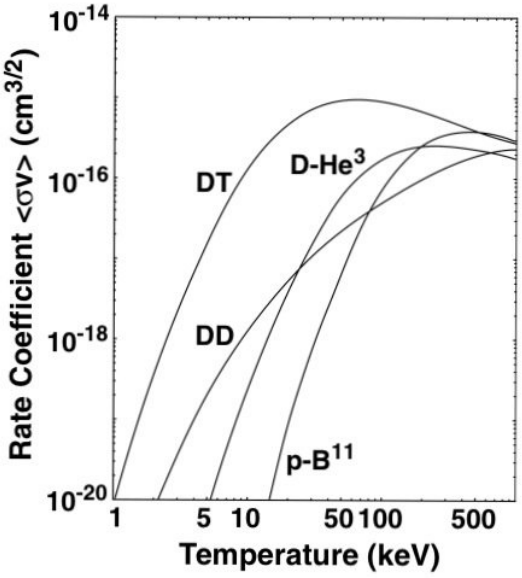

Figure 1.1: Fusion rate coefficients for different fusion reactions as functions of the temperature[5]

with N being the number of hydrogen atoms contained in the reactor. Assuming the energy leaving the reactor to be proportional to the thermal power stored in its core, we can characterize the power output by the energy confinement time τ.

$$P_{\text{out}} = \frac{Nk_BT}{\tau}$$

In a self-sustaining fusion reaction, we want $P_{\text{fusion}} \geq P_{\text{out}}$. From this requirement we obtain

$$\begin{aligned} anNT^2 &\geq \frac{Nk_BT}{\tau} \\ &\Rightarrow \\ nT\tau &\geq {}^{k_B}/_{\alpha} \end{aligned}$$

which is the ignition condition for a plasma burn, also known as the *triple-product* value.

Currently, no reactor capable of achieving a self-sustaining plasma burn is known to the author. The difference in power must therefore be continuously supplied by an external heating system. In this case, reactor operation is characterized by the *amplification factor*, which goes towards infinity as the triple product approches the ignition threshold.

$$Q = \frac{P_{fusion}}{P_{heating}} = \frac{P_{fusion}}{P_{out} - P_{fusion}} = \left(\frac{{}^{k_B}/_{\alpha}}{nT\tau} - 1 \right)^{-1}$$

Note that the amplification factor does not take into account the fact that the heating power also has to leave the reactor again. Achieving a sustained and viable reactor is therefore not given by the somewhat arbitrary $Q = 1$ threshold (which just implies a ${}^{50}/_{50}$–contribution from fusion power and external heating to the total output), but by the requirement that the output power recovered after all conversion processes (steam turbines, generators etc.) must exceed the heating power spent:

$$\begin{aligned} p_{\text{conv}} \cdot P_{\text{out}} &= p_{\text{conv}} \cdot (Q+1)\, P_{\text{heating}} \\ &\geq P_{\text{heating}} \\ &\Rightarrow \\ p_{\text{conv}} \cdot (Q+1) &\geq 1 \end{aligned}$$

with p_{conv} being the heat-to-electricity conversion efficiency of the power plant. With p_{conv}

of modern steam turbines usually being around 70% [6], a Q value of 0.45 would be required to achieve energy break-even (assuming no thermal losses prior to the turbine). Everything above that would directly translate to usable power.

1.2 Magnetic confinement concepts

The conditions in which nuclear fusion can be achieved can only be described as obscenely extreme. The required temperatures are so large that measuring them in Kelvin loses any and all degree of meaning. Instead, temperatures in fusion devices (or, more precisely, their energy scales $k_B T$) are commonly referred to in kilo-electronvolts. Given that the average fusion temperature is measured in thousands of the typical atomic/molecular binding energies, it is painfully evident that no material can bottle up such a reaction simply because it can not even *exist* at these conditions. Ironically, the circumstances responsible for this conundrum also provide us with the solution to it.

1.2.1 The magnetic bottle

Given that particles are usually completely ionized at fusion temperatures, this same statement obviously also holds for the fusion reactants themselves. At these temperatures, all electrons are stripped from the atomic nuclei, and the constituents form an overall electrically neutral two-fluid gas of electrons and nuclei, a *plasma*. Because all independently moving particles are charged, and unlike motion in a gas, the movement of plasmas is substantially impaired by magnetic fields. Charged particles can move uninhibited along the magnetic field, but Lorentz forces prohibit direct perpendicular motion and force the particles onto circular paths instead. As a result, particles can only escape perpendicularly either by drifts of these helical gyration orbits or by collisions with other plasma particles, which exchange momentum between particles and reset their movement directions. Their motion decomposes nicely into a gyration perpendicular to the magnetic field and a guiding-center motion, mostly (but not completely) along the magnetic field line. The gyration is characterized by its oscillation frequency, the *cyclotron frequency* $f_e = \frac{1}{2\pi}\frac{eB}{m}$ and its gyration radius, the *Larmor radius* $r_a = \frac{mv_\perp}{eB}$. Note that the cyclotron frequency does not depend on the particles' perpendicular velocity.

An important property of this motion is that the magnetic moment $\mu = \frac{mv_\perp^2}{2B}$ is an adiabatic invariant (conserved in first order with slow changes in B). Any local variance in B will create (by Faraday's law of induction) a looped electric field, which will modify the velocity of the atom. By Faradys's law, we know

$$\begin{aligned} m\dot{v_\perp} &= F \approx \frac{\text{area covered by loop path}}{\text{circumference of loop}} \cdot \left(\nabla \times \vec{E}\right) \\ &= e\frac{\pi r_a^2}{2\pi r_a}\dot{B} = \frac{1}{2} m v_\perp \frac{\dot{B}}{B} \\ &\Rightarrow \\ 0 &= \frac{1}{2}\frac{\dot{B}}{B} - \frac{\dot{v_\perp}}{v_\perp} = -\frac{1}{2}\frac{d}{dt}\left[\ln\left(\frac{v_\perp^2}{B}\right)\right] \\ &\Rightarrow \\ \text{const.} &= \frac{v_\perp^2}{B} \end{aligned} \tag{1.1}$$

However, this effective electric field is only visible in the co-moving frame of the particle. In the stationary device frame, the magnetic field is constant over time and the electric field vanishes. Since the Lorentz forces of the magnetic field can not perform any work, the change in the perpendicular kinetic energy must be fed from the parallel kinetic energy. The perpendicular kinetic energy (which is, as seen in equation 1.1, is proportional to the field) therefore forms a potential energy term, which creates a *magnetic mirror-force*, a force pushing particles against the parallel field gradient. This gives us a first concept for magnetic plasma confinement, the *magnetic mirror*.

1.2.2 Stellarators & Tokamaks

The strength of the magnetic mirror force depends on the magnitude of the perpendicular velocity. Any particle with $\frac{E_\parallel}{E_\perp} > \frac{B_{\max}}{B_{\min}}$ will be able to penetrate the mirror, and leak out at the end. The solution to this problem is to close off the ends by bending the magnetic field onto itself. This eliminates the end-leakage found in magnetic mirrors but replaces it with a new source of leakage: Cross-field drift. In a toroidally bent system, the parallel magnetic field is usually stronger on the inboard side. Because the Larmor radius is slightly smaller on the high-field side of the gyration, the guiding center will drift perpendicularly to the gradient (and the field). This creates a charge-separating vertical drift, where particles of one polarity will accumulate at the top and the other polarity at the bottom end of the confinement bottle. The electric field resulting from this charge imbalance will, in turn, create an outward radial drift, which will quickly push all plasma particles out of their confining field. However, not all is lost. By adding a poloidal twist to the magnetic field lines, both stages of this process can be simultaneously interrupted. As particles move along the twisted field lines, the poloidal motion will lead upward and downward displacements into each other, so the upward (or downward, depending on charge) drifts will cancel each other out. Additionally, the parallel connection from the top- to the bottom-side will allow parallel currents to cancel quickly any up-down charge imbalances, as the parallel conductivity of confined plasmas is extremely high.

This concept was first presented to the public by Lyman Spitzer in 1951 [7], and remains relevant until today. Spitzer showed that a figure-8 shaped magnetic loop generated by two circular coils can confine a plasma in a twisted magnetic bottle. His magnetic bottle design opened up the research into a large class of magnetic bottles with twisted vacuum fields, the Stellarators. Unfortunately, while Stellarators achieved orders of magnitude in confinement improvement, they could at the time not reach the confinement times predicted by *classical* plasma transport theory, and it took quite some time to understand why that was the case. The culprit was later identified in the residual magnetic mirror remaining in these machines. As the inboard field is larger than the outboard field, not all particles can make full turns across the machine but are instead trapped in localized orbits on the outboard side. A closer study of these orbits, coined *neo-classical* transport theory, revealed that - in contrast to the passing orbits circulating fully around the bottle - these trapped orbits were indeed unstable and had a tendency to drift outward. At the time, researchers attempted to find alternative configurations that would prove more stable, but analytical solutions for these orbits were rare, and computers were not powerful enough at the time to explorer larger configuration spaces.

All the more did a shock go through the western fusion research community when Russian

researchers around Andrej Sacharov and Igor Tamm revealed the T1 device [8, Please note that Tamm and Sacharov are not mentioned as authors, as their involvement was classified at the time], which showed confinement numbers beyond what was believed practically achievable. Sacharov and Tamm had employed a completely different strategy to achieve the poloidal twist in their confinement field. By inducing a toroidal current in their (initially poorly confined) plasma, they could achieve the same field twist that the Stellarator achieves, without having to rely on a complicated vacuum field geometry. This confinement strategy, coined Tokamak by its inventors, has the advantage of having a powerful continuous symmetry, which makes it virtually immune to neo-classical orbit drifts, and therefore allowed it to outperform its western counterparts significantly. This good neoclassical confinement, together with the fact that symmetric systems are much easier to design and construct, has made the Tokamak the world-leading approach to magnetic confinement fusion and the most likely candidate for the first fusion power plant.

The race between the Tokamak and the Stellarator is, however, far from being decided yet. While Tokamaks are comparatively easy to design and construct, they are challenging to operate, as Tokamak plasmas tend to be, for lack of a better word, *lively*. Where the structure of the Stellarator plasma is governed dominantly by its vacuum field, the vacuum field of the Tokamak is not twisted and therefore lacks a poloidal component to stabilize the plasma shape. The structure of the plasma is therefore fully derived from internal dynamics, which are governed by complex non-linear relations between pressure gradients, magnetic fields and thermal properties. As a result, Tokamaks frequently require continuous active stabilization of their plasma position. When improperly stabilized, they tend to eject all the energy stored in their plasma in a short burst. These plasma disruptions were a nuisance in small machines but are becoming increasingly more threatening as machines grow, and the amount of energy dumped increases likewise [9]. While not presenting a personal safety risk, the local damage caused by disruptions must still be repaired, and local radioactivity from the plasma fuel and activated machine components will make short-term access into the plasma vessel challenging.

Stellarators mostly do not suffer from these problems. The plasma surfaces are structured by the vacuum field, which dominates both the toroidal and the poloidal components (as opposed to just the toroidal component in a Tokamak). While the author can testify that Stellarators, too, *can* disrupt if provoked sufficiently, doing so requires a substantially larger amount of mistreatment, and even when occurring, disruptions are far less threatening due to the low toroidal current present in these devices.[1] Advances in numerical modeling have allowed the simulation of neo-classical orbit losses and the systematic exploration of configuration spaces that minimize these losses. The results of these efforts are several new kinds of numerically optimized stellarators which offer performance competitive with their Tokamak counterparts while having inherent steady-state capabilities (while still being somewhat challenging to build).

1.3 Characteristic quantities of toroidal confinement devices

Both Stellarators and Tokamaks are designed such that their magnetic field lines usually form closed *magnetic surfaces* (also called *flux-surfaces*). These surfaces are commonly represented via

[1] There is a common saying among pilots about planes and helicopters. Most planes just love flying, and when not actively prevented from it, will do all their best to continue doing it. Helicopters, however, dream of a sweet death, and your job as a pilot is to prevent them from ever realizing it (and dragging you along).

a label function mapping real-space points onto a flux surface label. Popular label functions are the toroidal magnetic flux (surface integral of the toroidal magnetic field) in Stellarators and the poloidal magnetic flux (surface integral of the poloidal magnetic field) in Tokamaks. This thesis will mainly use the *normalized toroidal flux* s, which is normalized to 1 at the last closed (not opened by divertor components) magnetic surface, which is usually referred to as *last closed flux-surface* (LCFS).

An important property is the degree to which the field-lines inside a magnetic surface are twisted. Locally, this can be characterized by the field line' *pitch angle* $\arctan\left({}^{B_{\mathbf{pol}}}/_{B_{\mathbf{tor}}}\right)$. As the pitch angle is not constant along a field-line, one often prefers to use the *rotational transform* $\iota = \oint \frac{RB_{\mathrm{pol}}}{rB_{\mathrm{tor}}} dL$, which represents the average number of poloidal turns taken for each toroidal turn of the field line. The Tokamak community often prefers the *safety factor* $q = \iota^{-1}$. The name safety factor is rooted in the fact that a large rotational transform makes a Tokamak susceptible to kink instabilities.

The flux-surfaces where the rotational transform is a rational number $\iota = {}^{n}/_{m}$ are particularly interesting. Field-lines along these surfaces travel along a path that takes them back to their starting position in only $\mathrm{lcm}\,(n, m)$ turns. This makes them particularly susceptible to magnetic field perturbations. If the (minor-)radial magnetic field along these lines experiences a perturbation of the form $\Delta B_r = \cos\left(\phi_0 + n \cdot \phi + m \cdot \theta\right)$ (with ϕ being the toroidal angle, and θ chosen so that ${}^{d\theta}/_{d\phi} = \text{const.}$ along field-lines), a particle travelling along this line would see a constant (minor-)radial field. Therefore, even small magnetic field perturbations can form magnetic structures, so-called *magnetic islands*, on these surfaces. The width of these islands depends on the rotational transform profile, more specificially, its gradient, the *magnetic shear*. A large magnetic shear suppresses magnetic island formation.

The magnetic field driven by external coils and the induced plasma current is also superimposed by currents driven by outward plasma flows (due to the Lorentz force). The strength of these currents, and the effects they create on the confining magnetic field, is proportional to the gradient of the thermal plasma pressure. The relative magnitude of these effects against the confining magnetic field strength is usually characterized by the *plasma beta* $\beta = \frac{p}{{}^{B^2}/_{2\mu_0}}$. **This is an important quantity that will repeatedly be mentioned throughout this thesis.** Intuitively, one should understand this quantity as the degree at which the plasma presses against its confining magnetic field. In magnetohydrodynamics (MHD), the plasma beta is the primary scaling parameter. An important corollary of this property is that low-field configurations can be used as a proxy for high-pressure operation to determine the impact of high-beta operation on confinement devices.

This thesis primarily requires on specific variants *volume-averaged toroidal beta* β_{vol} and *central toroidal beta* or *on-axis toroidal beta* β_{ax}, which are defined below:

$$\begin{aligned}
\beta_{\mathrm{vol}} &= 2\mu_0 \frac{\oint_{\mathrm{volume}} p dV}{B^2_{\mathrm{tor,ax}}} \\
\beta_{\mathrm{ax}} &= 2\mu_0 \frac{\oint_{\mathrm{axis}} p dL}{B^2_{\mathrm{tor,ax}}} \\
B_{\mathrm{tor,ax}} &= \oint_{\mathrm{axis}} B_{\mathrm{tor}} dL
\end{aligned}$$

Both of these plasma betas are normalized against the average toroidal field along the axis. Please note that this kind of definition differs substantially from the *poloidal beta* popular in the Tokamak community, which uses the poloidal instead of the toroidal field. As a result, the poloidal plasma beta is usually substantially larger than its toroidal counterpart. **From now on, every instance of plasma beta will refer to toroidal plasma beta unless explicitly stated.** The ratio between these two quantities, the *peaking factor* $f_p = \beta_{\mathrm{ax}}/\beta_{\mathrm{vol}}$will be used as a primary descriptor for the shape of the pressure profiles.

1.4 Heat- and Power-exhaust: The Divertor

So far, the main focus of this text was on how to achieve a fusion burn and bottle it up in a magnetic field. I cleverly forgot to mention that even when within a magnetic bottle, there must still be a point where the plasma volume is limited by contact with an outer material. Even in a cold plasma, the plasma particles (especially the ions) will be fast enough to sputter bulk material atoms on impact and eject the sputtered atoms back towards the plasma core. Since most of the low-Z elements are not particularly suited for the construction of thermally resilient components, these back-ejected atoms will have a substantial charge after ionization. As Bremsstrahlung goes with Z^2[10], these particles will therefore give off substantially more radiation than a plasma built out of Hydrogen and Helium isotope. The increased radiation degrades the energy confinement, resulting in a *radiative collapse*, a disruption's annoying little brother.

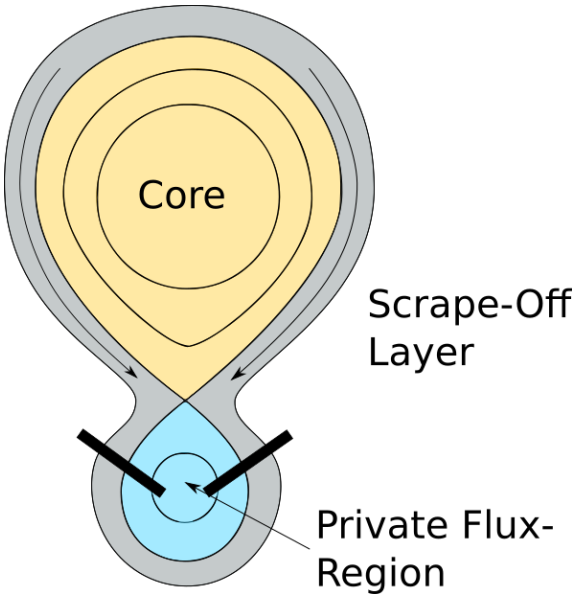

Figure 1.2: Toroidal cross-section of a poloidal divertor magnetic configuration.

To avoid the contamination of the plasma core with high-Z impurities, the area around the limiting geometry is usually closed off in a topologically separate magnetic region. The plasma core is now no longer directly connected to any plasma-facing components. Instead, the heat flows through this secondary magnetic region, the *scrape-off* layer, which forms the heat sink for the fusion reaction. Inside the scrape-off layer, plasma particles flow further downstream until they hit the divertor plate and are neutralized there. As sputtered neutral particles flow back from the divertor plate, they are ionized by the incoming hot plasma and are now trapped in the scraper-off layer region by the secondary magnetic bottle. In the SOL, the impurity radiation turns from a curse into a boon, as the radiating impurities will act as a local sink for the heat flowing in from the plasma core. In the best case, they form a partially ionized gas cloud above the divertor plate, which converts most of the incoming heat into radiation and shields the plasma-facing target

plate. This *detached* divertor operation is highly beneficial for the lifetime of the divertor target [11, 12].

To properly trap sputtered neutrals in the edge, the *parallel connection length* between the outer and inner side of the scrape-off layer must be sufficiently long. The longer the parallel connection length is, the wider the strike-line of the in-coming heat flow will be (due to perpendicular diffusion), and the harder it will be for partially ionized impurities to reach the boundary of the core plasma.

Most common - especially in Tokamaks - is the *poloidal divertor* [13, 14, 15], which follows the toroidal symmetry of the Tokamak (figure 1.2). A set of divertor coils generates a strong poloidal field in the edge, which creates its own private flux region separated from the core. The shared inner boundary, where the two flux regions meet, is called the separatrix. The scrape-off layer is formed by the surrounding flux surfaces, which encompass both the plasma core and the divertor private flux region and move excess heat and particles from the plasma core onto the divertor plate. While popular in Tokamaks, this type of divertor is not suited for Stellarators, which can not have a toroidally symmetric plasma edge. Most Stellarator lines include their own unique divertor concept, both to tailor the divertor to their specific geometric requirements and to experiment with different divertor types to see which one is the easiest to implement and operate. Recent examples include the island divertor of Wendelstein 7-X [16], the helical divertor of the Large Helical Device (LHD) [17] and the non-resonant divertor of the Helically Symmetric eXperiment (HSX) [18].

1.5 The Wendelstein 7-X Stellarator

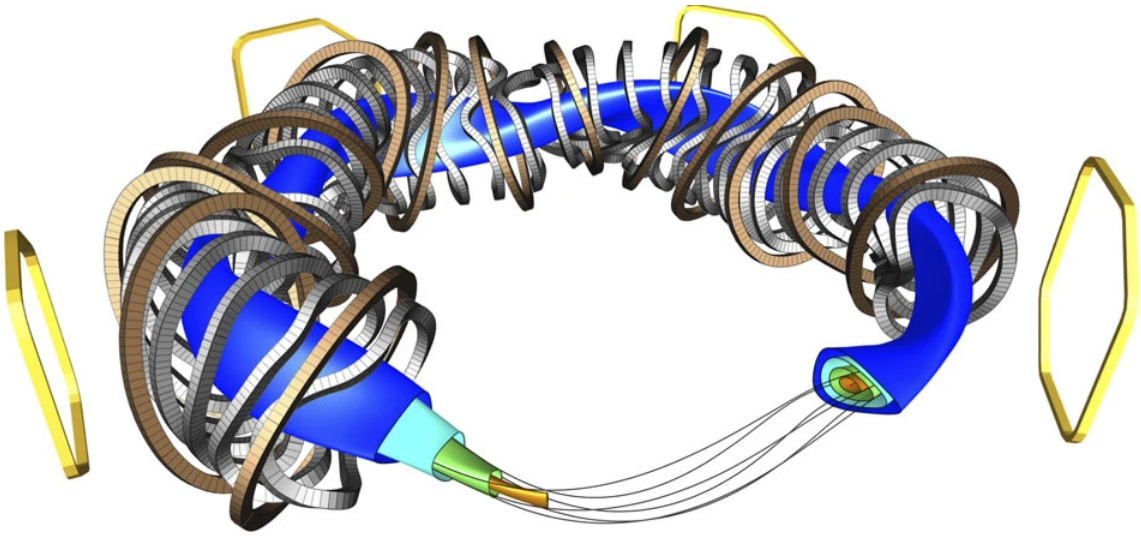

Figure 1.3: Layout of the Wendelstein 7-X Stellarator. Surfaces and lines indicate magnetic surfaces and field-lines. Planar coils are shown in bronze, non-planar coils in silver. Trim coils are shown in yellow. [19]

The main focus of this thesis is the Wendelstein 7-X (W7-X) Stellarator [12] (see figure 1.3). W7-X is the newest member of the HELIAS line of stellarators and is in operation in the Max-Planck-Institute for Plasma Physics in Greifswald, Germany. At present, W7-X is the largest Stellarator in the world. The machine has a five-fold discrete rotation symmetry around the vertical axis and a flip symmetry around the x-axis. In the fusion research community, this is

commonly labeled as a five-fold *stellarator symmetry*, while mathematicians usually know this symmetry as the *dihedral group* of order 10, D_5 (the symmetries of the pentagon). W7-X is a modular stellarator, which means that, like in a Tokamak, it is completely built out of toroidally localized coils (in contrast to other Stellarator designs which include helical coils). In W7-X, five (all distinct) non-planar and two planar coils (for adjustment of the toroidal field) form a *half-module*, two oppositely oriented half-modules form a *module*, and five modules together form the complete Stellarator. Each half-module also contains a single *control coil* to adjust the island phase and size (not shown), and each module also features a trim-coil for the correction of low-order error fields. In total, the coil systemW7-X consists of 50 non-planar and 20 planar coils, 10 control coils and 5 trim coils.

The main experimental goal of W7-X is to demonstrate steady-state operation in a high-performance (and high-confinement) operational regime. To achieve this, all major components of the device have been designed with steady-state water cooling in mind. However, the present campaigns were focused on validating the divertor concept and testing the operational safety in low-beta scenarios, where the machine has (so far) performed well [12]. The 2021 experimental campaign will, for the first time, include the water-cooled divertor, which will enable the device to push into the steady-state scenario regime.

For heat- and particle exhaust, W7-X uses a variant of the divertor concept called the *island divertor*. In the island divertor, the scrape-off layer is formed by a group of magnetic islands, which form closed flux tubes around the core plasma. These islands are then intersected and cut open by 10 divertor target plates, which follow the half-module structure of the overall device. In some magnetic configurations, these islands are not cut open completely, and a small *remnant island* remains toroidally closed. Magnetic island chains form on flux surfaces where the *rotational transform* ι (the change in poloidal angle during one toroidal turn) is a rational number $\iota = \frac{n}{m}$, and the magnetic field (in minor radial direction) has a matching Fourier component of shape $\cos(m \cdot \theta - n \cdot \phi + \Delta\phi)$. The width of the island is proportional to the strength of this component and inversely proportional to the gradient of ι, the *magnetic shear*. Since W7-X has a shallow ι-profile, and therefore a low magnetic shear, magnetic islands (intentionally) are wide and also have a low internal rotational transform. In the cases of $\iota = 5/4$, $\iota = 5/5$ and $\iota = 5/6$ at the plasma boundary, these islands form chains with 4, 5, and 6 islands respectively, which have their *O-point* (the center of the island) and their *X-point* (the intersection point of two neighboring islands) centered on the respective rational surfaces. The

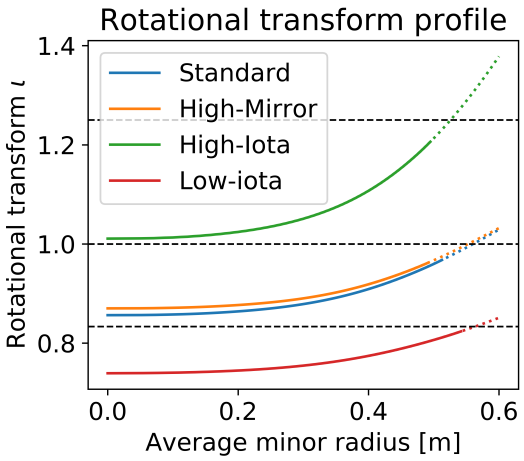

Figure 1.4: Rotational transform profile of Wendelstein 7-X for four magnetic configurations against average minor radius of the flux surfaces. Solid lines indicate rotational transform profiles obtained form equilibrium calculations. Dashed lines indicate spline-based extrapolations of these profiles. The black lines indicate the resonant values of $\iota \in \{5/6, 5/5, 5/4\}$.

divertor consists of two target plates (horizontal and vertical target), holding the main strike-line of the edge plasma (see figures 1.5 and 1.6). The gap between the target plates (figure 1.7) serves as an exit to pump out neutral particles. The horizontal target plate itself is further subdivided into three subsections. The front (low-iota) and back (high-iota) sections of the horizontal target, as well as the vertical target, can bear heat-loads up to $10\,\mathrm{MW\,m^{-2}}$, while the middle section can only bear $0.5\,\mathrm{MW\,m^{-2}}$. To close off the divertor assembly and prevent neutrals from escaping the pumping volume, the divertor target plates are surrounded by baffle tiles (figure 1.7). These tiles are cooled but are not designed to bear the heat loads of the main strike-line. They can only sustain a heat-load of $0.25\,\mathrm{MW\,m^{-2}}$. Beyond the divertor assembly itself, W7-X also features a heat-shield protecting select regions of the plasma vessel (figure 1.5, bottom subfigure), which has non-uniform maximum heat-loads. The only heat-shield region relevant for this region is the region protecting the outer observation ports of the triangular plane, the *U-Ports*, whose location is also highlighted in figure 1.5. Around these ports, the heat-shield is limited to $0.2\,\mathrm{MW\,m^{-2}}$.

W7-X has an adjustable configuration space. The reference configuration space of W7-X consists of 9 configurations, shown in table 1.1. By increasing or decreasing the current in the planar coils, the ratio between poloidal and toroidal field, and therefore the overall rotational transform, can be tuned. This can be used to modify the location of the divertor islands and select between the different island chains. By creating opposing currents in the planar coils, the magnetic axis can be shifted by a vertical field. Furthermore, the currents in the individual nonplanar coils can be varied to modify the magnetic mirror strength, which influences the neoclassical toroidal *bootstrap current*. In the first operational campaign, W7-X did not operate with a divertor but instead relied on five limiters directly intersecting the last closed flux-surface, operating in a correspondingly designed limiter configuration.

Configuration	I_n [MA]	Non-Planar Factor					Planar Factor	
Standard	1.45	1.0	1.0	1.0	1.0	1.0	0.0	0.0
Low-Iota	1.32	1.0	1.0	1.0	1.0	1.0	0.25	0.25
High-Iota	1.6	1.0	1.0	1.0	1.0	1.0	−0.23	−0.23
Low-Mirror	1.49	0.94	0.98	0.98	1.06	1.06	0.0	0.0
High-Mirror	1.44	1.08	1.05	1.0	0.95	0.92	0.0	0.0
Low-Shear	1.47	1.13	1.12	1.05	0.85	0.84	−0.2	0.2
Inward-Shifted	.1.47	0.96	0.95	0.97	1.07	1.08	0.1	−0.2
Outward-Shifted	1.46	1.04	1.04	1.01	0.96	0.96	−0.14	0.14
Limiter	1.43	1.07	1.1	1.02	0.92	0.89	−0.1	0.2

Table 1.1: List of reference configurations for Wendelstein 7-X. I_n gives the current factor required to reach a mean axial field of 2.5 T [20]

1.6 Key research objective and prior works

To ensure a safe operation of W7-X, it is absolutely critical that the distribution of heat is controlled during operation. A typical discharge involves around 3 MW to 5 MW of heating power, and can yield local heat-flux densities exceeding $1\,\mathrm{MW\,m^{-2}}$. If plasma-facing components were continuously

exposed to excessive heat fluxes, they would experience overload and, eventually, structural failure. In such a case, sensitive electric components, cooling pipes, and mechanical load-bearing structures would be directly exposed to the substantial heating power carried by the plasma. This would induce damages in the device which would be time-consuming to repair and probably delay the experimental campaigns by weeks (at least). For example, a damaged water pipe would release substantial amounts of steam into the vacuum vessel. After repair of the pipe and pump-down of the vessel volume to a vacuum, all the small water and oxygen deposition pockets would have to be baked out over multiple days.

It is, therefore, highly desirable to avoid undesired heat loads on plasma-facing components of the device. On the experimental side, there are multiple diagnostics installed to monitor for temperature overload. The main divertor is constantly monitored by a set of infra-red cameras, while key locations on the divertor baffles will - in upcoming campaigns - be equipped with thermocouples to ensure that temperature limits are observed. However, none of these diagnostics provides a complete view. Therefore, accurate forward modeling of the various magnetic configurations and their heat-load patterns is a key tool in ensuring the operational safety of W7-X. As plasmas are excellent conductors, and therefore have strong internal currents that shape the confining field as well, it is not sufficient to simply draw on the vacuum field calculations for this information. Additionally, the main drivers of structural change in fusion plasmas, the pressure (or its normalized equivalent, the plasma beta), and the plasma current, need to be included in such an analysis.

This motivation yields the key research objective, which is to *assess the effects of finite plasma beta on the magnetic topology of the edge islands and the resulting changes in the heat load distribution on plasma-facing components.*

As part of the design of W7-X and its divertor, configurations have been reviewed for finite-beta effects before. Early efforts are the works in [21, 22, 23, 24, 25, 26], which look at finite-beta equilibria of standard and high-iota configuration (see table 1.1). Unfortunately, these works cover only isolated cases, and the covered range of information computed from these equilibrium calculations is incoherent between the different publications. This provided the main motivation of this thesis, which is the provision of a comprehensive and coherent overview of a large finite-beta configuration space, in which both the effects of finite-beta operation on the magnetic topology and the corresponding effects on the heat-load distributions are uniformly covered. A work quite similar to this thesis in its methodical approach is the Ph.D. thesis of Hauke Hölbe [27]. That work is mainly focused on the scenarios relevant for the evaluation of the divertor scraper element, and therefore primarily concerns itself with the effect of the toroidal plasma current on the divertor, which is not a primary focus of this thesis, as it is already comprehensively covered in existing research ([28]).

1.7 Structure of this thesis

- *Chapter 2* will give an introduction into the theory of the MHD equilibrium in fusion devices, the plasma beta (a fundamentally important scaling parameter in confinement fusion), and stochastization effects. Wherever possible, the chapter will take a dual approach. Simple mathematical models will be used to provide hints at possible expected effects, while additional explanations will be provided to motivate the physical mechanisms driving these effects (which sometimes stow away in simplifications of the mathematical models). Starting from

the basic principles of MHD, the first part will focus on the derivation and discussion of the Grad Shafranov equation, an equation for axisymmetric Tokamaks. The second part of this chapter is oriented towards introducing the concept of stochastization driven by overlapping perturbations.

- *Chapter 3* will provide an overview over the various numerical tools necessary for an integrated numerical treatment of the plasma edge. It opens up with a discussion of two magnetic equilibrium codes for fusion devices (VMEC and HINT) based on opposing design principles. Afterwards, the numerical techniques applied to derive high-resolution heat-load distribution on PFCs from the equilibrium fields are discussed. The chapter then closes with a treatment on a newly developed method for geometric diagnostic mapping based on flux-surface label calculations accelerated with machine learning.

- Whereas the previous chapters are more concerned with theoretical and modeling aspects of this work, *Chapter 4* is primarily focused on experimental techniques and their implementation. The first half introduces the reader to the various diagnostic systems that provide the experimental data used during this thesis. The second half discusses a diagnostic developed and calibrated throughout this thesi: A reciprocating magnetic probe sensitive enough to directly measure the difference in magnetic field profiles driven by internal plasma currents. A particular focus is placed on the design of the time-integration system and a post-processing method that inverts the measurement chain's calibrated forward model to improve the accuracy of the measured time traces.

- *Chapter 5* focuses on benchmarking the equilibrium models against experimental measurements. This chapter holds three separate contributions. Firstly, the changes in the edge magnetic field predicted by the equilibrium simulation are compared against direct measurements achieved with the reciprocating probe presented in chapter four. Secondly, the pressure distribution obtained during the equilibrium calculations is benchmarked against measurements provided by the diagnostics outlined in chapter four. The profiles measured by the different diagnostics are also mapped onto each other taking the island geometry into account, a feat enabled by the mapping approach developed in chapter three. Finally, the predicted stability of the standard configuration is benchmarked against experimental low- and medium-beta data by separating the plasma-beta related variations of its strike-line position from the (substantially larger) effects of the toroidal plasma current.

- Being the final chapter holding original contributions, *Chapter 6* is exclusively concerned with the results obtained from heat-load modeling outlined in the first three chapters. Founding the back-bone of this thesis, this chapter discusses the effects observed on the different magnetic configurations in finite-pressure operation. For three magnetic configurations, the magnetic standard-, high-iota-, and low-iota-configuration (which differ in the structure of their edge islands), both the effects on the edge magnetic field topology as well as the effects on the divertor heat-loads are discussed in-depth. Particularly, this also outlines risk-scenarios which will require avoidance and mitigation in high-performance operation.

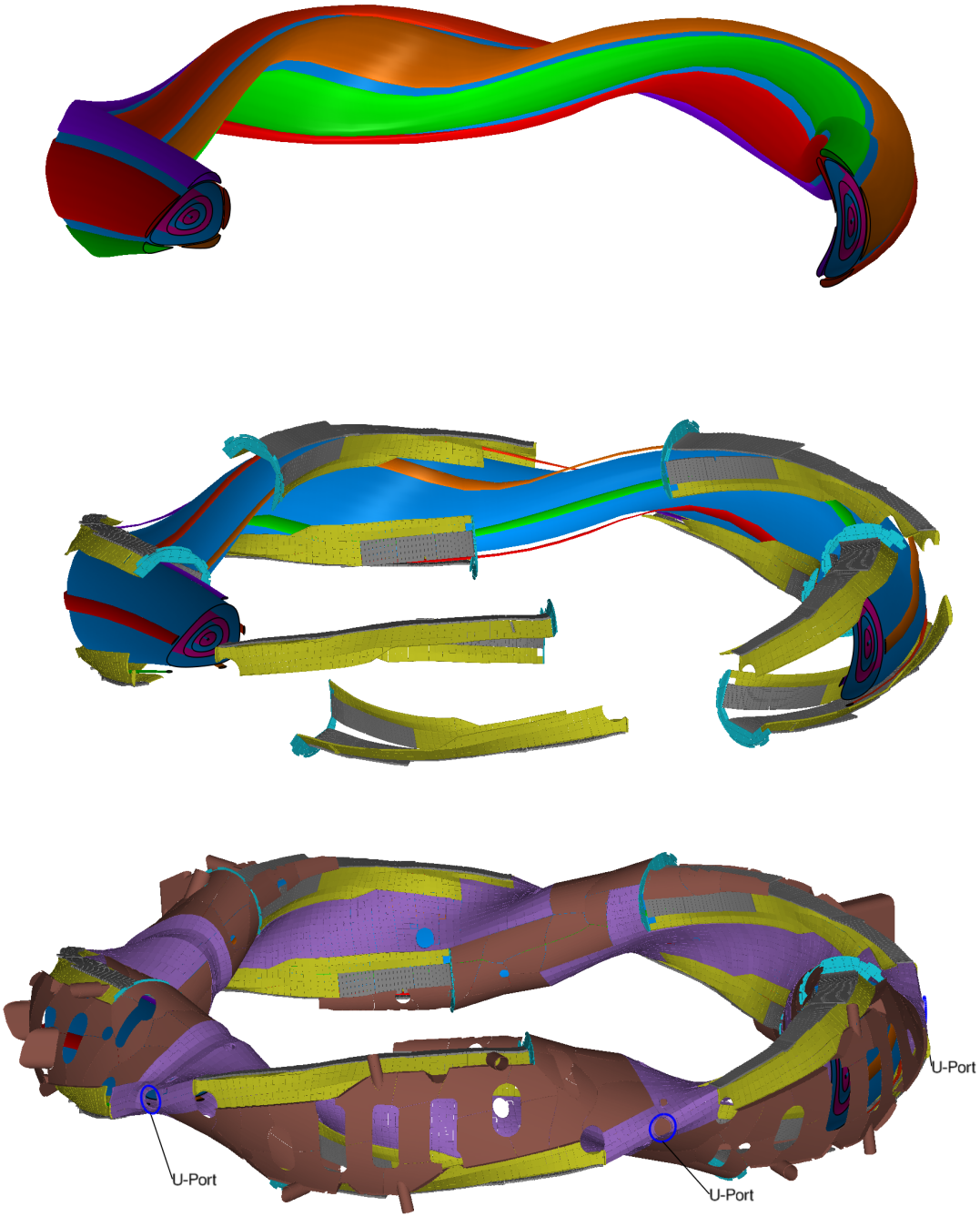

Figure 1.5: Overview of the magnetic flux surface structure of W7-X, including the islands and in blue the last closed flux-surface in magnetic standard configuration, (top), the divertor components (target plate in grey, baffles in yellow, toroidal closure in cyan) together with confined island remnants (middle) and the complete structure of plasma-facing components with steel panels in terracotta, heat shield in purple and the U-port highlighted (bottom)

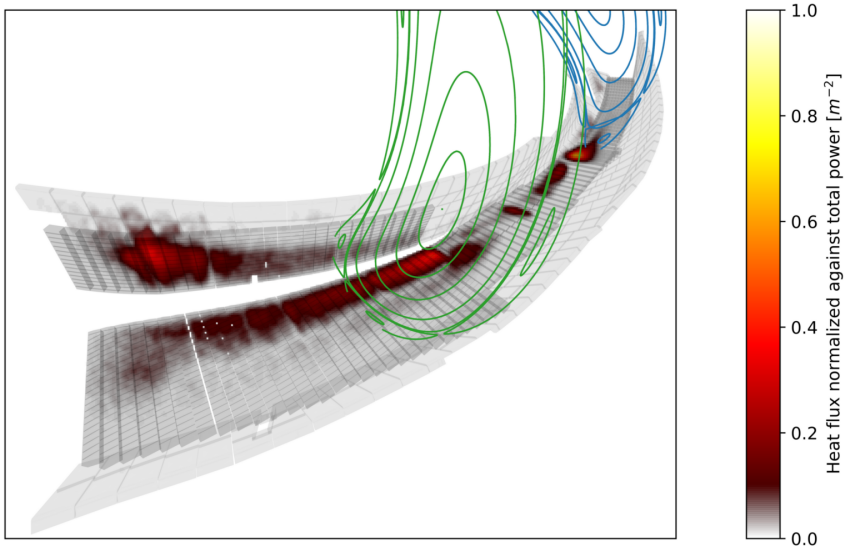

Figure 1.6: Overview of a single divertor half-module with divertor geometry indicated in grey, magnetic topology for standard 5/5 configuration overlaid as green and blue and the simulated heat-load distribution (normalized to total power) for $D_\perp = 1\,\mathrm{m}^2\,\mathrm{s}^{-1}$ overlaid on top of the divertor geometry

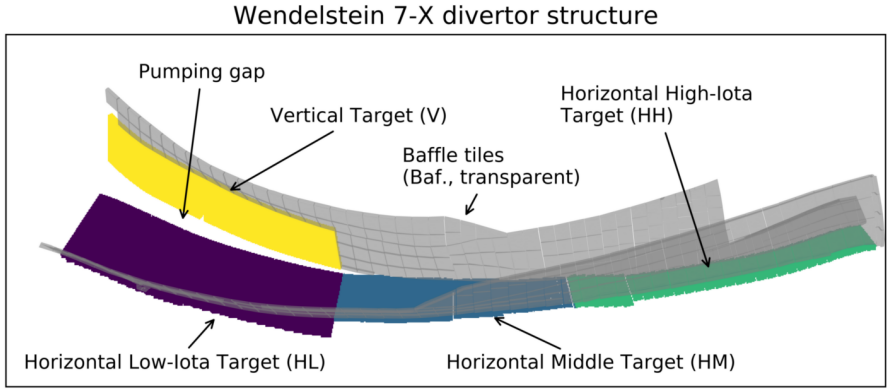

Figure 1.7: PFC structure of the Wendelstein 7-X divertor system, including the structure of the divertor target plate. Colored components together form the divertor plate.

2 MHD equilibrium theory

Whether Stellarator or Tokamak, all fusion plasmas are characterized by their strong internal current dynamics. Plasmas are excellent conductors, and the internal currents are both structured by and modify the confining magnetic field. Magnetohydrodynamics (MHD) is the theory which studies these complex interactions between the plasma and its magnetic field, particularly in the fluid limit (where the plasma is not modeled on a per-particle basis but in a collective fluid approach). MHD equilibria are steady-state solutions of MHD equations, where the exact structure of the equilibrium depends on the MHD theory itself. This chapter will be divided into four sections. The first section will introduce the general conditions necessary to achieve a steady-state MHD equilibrium. These conditions are, however, very complex and general and give very few hints in terms of actually expected effects. Therefore, the second section will restrict itself to ideal MHD equilibria in Tokamaks, where much more specific and informative conditions can be derived. These will then be discussed in more detail both on the equilibrium equations themselves and on a numerical example derived using 2D finite element simulations. Finally, a final section will introduce the topic of stochastization in chaotic systems and discuss its implications on confinement devices.

This chapter contains two original contributions:

- A new, simple derivation of the Grad-Shafranov equation based on covariant electrodynamics in slab coordinates
- A simple finite-element based solver for the Grad-Shafranov equation based on the FeNICs package and its application.

2.1 First principle conditions for MHD equilibria

MHD equilibrium theories can be mainly divided along two orthogonal axes:

- Depending on whether electrons and ions (and different ion species) are treated separately or as velocities and currents of a single fluid, MHD theories can be divided into *single-fluid* and *multi-fluid* theories.
- Furthermore, MHD theories can be subdivided into *resistive MHD* theories, which include a resistive energy dissipation channel, and *ideal MHD* theories, which do not take into account

resistive effects and instead suppress electric fields altogether. Resistive MHD theories can capture a larger class of changes in the plasma structure, as magnetic reconnection (creation and annihilation of magnetic dipoles) is forbidden in ideal MHD theory due to the suppression of electric fields (which would invariable arise during such an annihilation event). Because purely-resistive MHD effects rely on energy dissipation, they are usually orders of magnitude slower than effects in ideal MHD, which only redistribute magnetic energy densities inside the plasma.

The focus of this section will be placed on the equilibrium state in single-fluid MHD theories. The difference between resistive and ideal equilibria mostly concerns the magnitude of the perpendicular plasma flow, which is mostly ignored throughout this thesis. Therefore, from an equilibrium perspective, resistive and ideal theories are assumed to yield equivalent equilibria.

The MHD equilibrium is characterized by stationarity of all describing fields, usually the plasma flow, its pressure, and the magnetic field. The most important condition is the force balance condition, given by the stationarity of mass flow:

$$\begin{aligned} 0 &= \rho\frac{\partial\vec{v}}{\partial t} \\ &= \vec{F} - \rho\vec{v}\cdot\vec{\nabla}\vec{v} \\ &= \left(\vec{F}_{\text{Lorentz}} - \vec{\nabla}p\right) - \rho\vec{v}\cdot\vec{\nabla}\vec{v} \\ &= \left(\mu_0^{-1}\left(\vec{\nabla}\times\vec{B}\right)\times\vec{B} - \vec{\nabla}p\right) - \rho\vec{v}\cdot\vec{\nabla}\vec{v} \end{aligned}$$

Please note, that $\vec{F}$ and $\vec{j}$ refer to force- and current-densities, and not forces and currents. Oftentimes, the inertial contributions can be neglected in the force balance due to the extremely low plasma densities ($\rho\vec{v}\cdot\nabla\vec{v} \ll \vec{F}$). This equation is therefore usually simplified as

$$\begin{aligned} \mu_0^{-1}\left(\nabla\times\vec{B}\right)\times\vec{B} &= \vec{j}\times\vec{B} \\ &= \nabla p \end{aligned} \tag{2.1}$$

The stationarity of the magnetic field is usually used to simplify the expression for the electric field. When neglecting sheath effects ($\vec{\nabla}\cdot\vec{E}=0$), and assuming $0=\frac{\partial\vec{B}}{\partial t}=-\vec{\nabla}\times\vec{E}$, we get

$$\begin{aligned} \vec{E} &= \vec{E}_{\text{Lorentz}} + \vec{E}_{\text{Resistive}} \\ &= \frac{q}{m}\rho\vec{v}\times\vec{B} - \eta\vec{j} \\ &= \frac{q}{m}\rho\vec{v}\times\vec{B} - \eta\frac{\left(\vec{\nabla}\times\vec{B}\right)}{\mu_0} \end{aligned}$$

with the mean charge / mass ratio q/m. For an equilibrium solution neglecting sheath effects, we require $\vec{E}=0$. If the resistivity η (which is usually a tensor) is zero, we get the ideal MHD condition $\vec{v}\parallel\vec{B}$ forbidding perpendicular plasma flow. In the case of resistive MHD, however, we get a relation between perpendicular flow and the plasma current.

$$\vec{\nabla} \times \vec{B} = \frac{\mu_0}{\eta} \frac{q}{m} \rho \vec{v} \times \vec{B} \tag{2.2}$$

These two relations together form the primary equations for resistive MHD equilibria. A third requirement commonly imposed in MHD models is the requirement that no heat is transported between plasma particles. In such a plasma, all expansion must be adiabatic, and therefore

$$p\rho^{-\gamma} = \text{const.}$$

By varying the adiabatic coefficient, multiple diffusive heat transport regimes can be approximated. Additionally, this constraint has a $\gamma \to -\infty$ limit representing a constant density at a freely decoupled pressure. This corresponds to the limit towards an infinite heat capacitance.

2.2 Axi-symmetric ideal MHD equilibria

2.2.1 The Grad-Shafranov equation

One of the most important special cases of MHD is the subspace of axisymmetric systems, the ideal Tokamaks. As the axial rotation is a sub-group of the Lorentz-group, the Lorentz-invariance of electrodynamics and mechanics mandates that this symmetry should be preserved by the equilibrium solution as well. The axisymmetric solutions of single-fluid MHD are described by the *Grad-Shafranov-equation [29, 30]*, which is a common basic equation in plasma physics. In this section, I will present a new approach for shortly deriving the Grad-Shafranov equation in covariant electrodynamics. Note that the idea to derive the Grad-Shafranov equation covariantly is not new, but was so far only used to derive stellar solutions including gravitation, but not for simplification of the derivation.

Using a slab coordinate system (t, ϕ, r, z), the covariant vector potential can be written as a function of only r and z. We assume the equilibrium to be both time-invariant and *ideal* in the sense of an infinite conductivity limit. In this case, we can restrict ourselves to the spatial components and neglect the t component. The derivation will be done in curvilinear coordinates with the following notations:

- Covector coordinates and vector basis elements (derivatives along coordinate functions) will have lower indices
- Vector coordinates and covector basis elements (coordinate function gradients) will have upper indices
- Doubly-occurring indices are implicitly summed over

In toroidally symmetric slab coordinates, the following expressions hold:

$$
\begin{aligned}
A_\mu &= \begin{pmatrix} A_\phi \\ A_r \\ A_z \end{pmatrix} \\
F_{\mu\nu} &= \begin{pmatrix} 0 & -\partial_r A_\phi & -\partial_z A_\phi \\ \partial_r A_\phi & 0 & \partial_r A_z - \partial_z A_r \\ \partial_z A_\phi & \partial_z A_r - \partial_r A_z & 0 \end{pmatrix}
\end{aligned}
$$

$$
\begin{aligned}
g_{\mu\nu} &= \begin{pmatrix} -r^2 & 0 & 0 \\ 0 & -1 & 0 \\ 0 & 0 & -1 \end{pmatrix} \\
g^{\mu\nu} &= \begin{pmatrix} -r^{-2} & 0 & 0 \\ 0 & -1 & 0 \\ 0 & 0 & -1 \end{pmatrix} \\
\sqrt{-\det g} &= r \\
\mathcal{D}^{\mu\nu} &= \frac{\sqrt{-\det g}}{\mu_0} g^{\mu\alpha} g^{\nu\beta} F_{\alpha\beta} \\
j^\nu &= \mu_0^{-1} \partial_\mu \mathcal{D}^{\mu\nu}
\end{aligned}
$$

with the covariant vector potential A_μ (covector), the covariant field-strength tensor $F_{\mu\nu}$, the covariant metric tensor $g_{\mu\nu}$, the contravariant inverse metric tensor $g^{\mu\nu}$, the local volume density $\sqrt{-\det g}$, the contravariant electromagnetic displacement density $D^{\mu\nu}$ and the contravariant current density j^μ. We now define the poloidal flux $\psi = A_\phi$ and the normalized toroidal field $G = rB_\phi = r\left(\partial_r A_z - \partial_z A_r\right)$, and can explicitly calculate the current:

$$
\begin{aligned}
F_{\mu\nu} &= \begin{pmatrix} 0 & -\partial_r \psi & -\partial_z \psi \\ \partial_r \psi & 0 & r^{-1} G \\ \partial_z \psi & -r^{-1} G & 0 \end{pmatrix} \\
\mathcal{D}^{\mu\nu} &= \frac{\sqrt{-\det g}}{\mu_0} g^{\mu\alpha} g^{\nu\beta} F_{\alpha\beta} \\
&= \frac{1}{\mu_0} \begin{pmatrix} 0 & r^{-1}\partial_r \psi & r^{-1}\partial_z \psi \\ -r^{-1}\partial_r \psi & 0 & -G \\ -r^{-1}\partial_z \psi & G & 0 \end{pmatrix} \\
j^\nu &= \frac{1}{\mu_0} \partial_\mu \mathcal{D}^{\mu\nu} \\
&= \mu_0^{-1} \begin{pmatrix} -\left[\partial_r r^{-1} \partial_r \psi + r^{-1} \partial_z^2 \psi\right] \\ -\partial_z G \\ \partial_r G \end{pmatrix}
\end{aligned}
$$

In cartesian coordinates, the expression for the pressure gradient force density reads as:

$$\begin{aligned}
\vec{j} \times \vec{B} &= \epsilon_{ijk} \vec{e_i} j_j B_k \\
&= \epsilon_{ijk} \vec{e_i} j_j \left(\frac{1}{2} \epsilon_{klm} F_{lm} \right) \\
&= \frac{1}{2} \vec{e_i} j_j \left[F_{ij} - F_{ji} \right] \\
&= \vec{e_i} j_j F_{ij} \\
&= \nabla p
\end{aligned}$$

As gradients are covector-fields, the corresponding co-variant expression for the pressure gradient force density has to read as:

$$\begin{aligned}
\sqrt{-\det g} \partial_\mu p &= r \partial_\mu p \\
&= j^\nu F_{\mu\nu} \\
&= \mu_0^{-1} \begin{pmatrix} r^{-1} \left(-\partial_z G \right) \left(-\partial_r \psi \right) + r^{-1} \left(\partial_r G \right) \left(-\partial_z \psi \right) \\ - \left[\partial_r r^{-1} \partial_r \psi + r^{-1} \partial_z^2 \psi \right] \partial_r \psi - r^{-1} \left(\partial_r G \right) G \\ - \left[\partial_r r^{-1} \partial_r \psi + r^{-1} \partial_z^2 \psi \right] \partial_z \psi - r^{-1} \left(\partial_z G \right) G \end{pmatrix}
\end{aligned}$$

Taking the Ansatz of G to be representable as a function of $G(\psi)$ with derivatives G' and G'', we can further simplify this expression:

$$\begin{aligned}
r \partial_\mu p &= \mu_0^{-1} \begin{pmatrix} r^{-1} G' \left[\left(\partial_z \psi \right) \left(\partial_r \psi \right) - \left(\partial_r \psi \right) \left(\partial_z \psi \right) \right] \\ - \left[\partial_r r^{-1} \partial_r \psi + r^{-1} \partial_z^2 \psi \right] \partial_r \psi - r^{-1} \left(\frac{1}{2} \frac{d}{d\psi} G^2 \right) \partial_r \psi \\ - \left[\partial_r r^{-1} \partial_r \psi + r^{-1} \partial_z^2 \psi \right] \partial_z \psi - r^{-1} \left(\frac{1}{2} \frac{d}{d\psi} G^2 \right) \partial_z \psi \end{pmatrix} \\
&= -\mu_0^{-1} \left[\partial_r r^{-1} \partial_r \psi + r^{-1} \partial_z^2 \psi + r^{-1} \frac{1}{2} \frac{d}{d\psi} G^2 \right] \partial_\mu \psi
\end{aligned}$$

This suggests that p must also be representable as a function of ψ. This brings us to a scalar equation for ψ

$$\begin{aligned}
-\mu_0 r \frac{dp}{d\psi} &= \partial_r r^{-1} \partial_r \psi + r^{-1} \partial_z^2 \psi + r^{-1} \frac{1}{2} \frac{d}{d\psi} G^2 \\
&\Leftrightarrow \\
-\mu_0 r^2 \frac{dp}{d\psi} - \frac{1}{2} \frac{d}{d\psi} G^2 &= r \partial_r r^{-1} \partial_r \psi + \partial_z^2 \psi \\
&= \Delta^\star \psi \\
&= \mu_0 r j^\phi
\end{aligned}$$

, which is commonly referred to as the *Grad Shafranov equation [29, 30]*. To avoid confusion, please note a few specialties of this equation:

- The elliptic operator $\Delta^\star$ is not the Laplacian operator, which would be expressed as $\Delta = r^{-1} \partial_r r \partial_r + \partial_z^2$, but is closely related (in particular, the second order terms are identical).
- j^ϕ is the ϕ-component of the contra-variant current vector density in slab coordinates. This is not the local toroidal current, which would be express as $j_{\mathrm{tor}} = r j^\phi$ (since $|e_\phi| = r$).

In this equation, the plasma is now decoupled into a set of flux surfaces, which are the isocontours of the poloidal flux function ψ.

2.2.2 Equilibrium effects in axi-symmetric plasmas

To determine the effects of equilibria on the profile, it is instructive to perform a qualitative examination of the Grad-Shafranov equation and infer some properties about its solution space. For simplicity, we limit ourselves to solutions with $\psi = 0$ at the edge and $\int_\Omega \psi > 0$ inside (positive average flux, non-negative net toroidal current).

- In order to have an overall positive solution for ψ, the left-hand side of the equation has to be overall negative. Therefore we would mostly (but not necessarily everywhere) expect $\frac{d}{d\psi}G^2 > 0$. When assuming a positive toroidal field B_0, we can fix $G(0) = r_0 B_0$ at the edge (with r_0 being the radius of a point on the plasma edge, and B_0 being the toroidal field at that point). In a vacuum, we could have a solution with constant G, but in a solution with finite current density, G has to increase towards the plasma core to maintain a positive slope in ψ. This implies that the toroidal field must be increased as soon as a toroidal plasma current is present. Physically, this is related to the divergence-freedom of the total current. The $\nabla p \perp j$-requirement prohibits radial balance currents. However, a field-aligned helical toroidal current is by itself not divergence-free (due to the spatial metric being larger on the inboard side of the torus). Therefore, a parallel current must always also be accompanied by a perpendicular current balancing out the charge flow, which is called the *diamagnetic current*. The same effect also holds vice-versa. The resulting perpendicular current enhances the toroidal field.

- If the pressure-influence can be neglected, G can be obtained directly from the requested current profile. $G = \sqrt{B_0 + \int_0^\psi j_\phi(\psi)\, d\psi}$, Because $B_{\text{pol}} = \nabla\phi \times \nabla\psi = r \cdot \frac{e_\phi}{|e_\phi|} \times \nabla\psi$ and B

- More generally, assuming $p(0) = 0$, $\frac{dp}{d\psi} > 0$, the left-most term in the Grad-Shafranov equation is negative, and therefore enhances the effects of the second term. To maintain the average current profile, the diamagnetic current, therefore, has to be decreased and, eventually, inverted. This turns the low-pressure enhancement of the toroidal field required by the plasma current into a suppression of the toroidal field at high pressure, the *diamagnetic effect*.

- The two terms on the left-hand side can not exactly match, as the $r^2 p'$ term is radially unbalanced. Even when balanced in flux surface average, the left-hand side will become overall more negative in the out-board region and less negative in the in-board region of the device. As the differential operator is Laplacian-like, the peak point of the flux will generally move with the peak of its source density. Therefore, the magnetic axis would be expected to move outwards. This effect is commonly referred to as the *Shafranov shift*. Physically, the increased and unbalanced diamagnetic current, driven by the pressure gradient, drives an unbalanced parallel return current to balance out the charge flow. This return current, the *Pfirsch-Schlüter-current,* flows around the axis on the out-board side. Therefore it causes a vertical field in the central plasma core. This vertical field changes the location of the $B_z = 0$, which defines the magnetic axis.

- Surprisingly, all equilibrium effects are completely independent of the toroidal field, even though the strength of the diamagnetic current is strongly coupled to it. The only limitation imposed is that rB_0 must be sufficiently large at the edge to guarantee $G^2 \geq 0$ everywhere. Provided that this condition is fulfilled, identical poloidal flux distributions can be found for any valid toroidal field value at the outer edge.

2.2.3 A simple Tokamak equilibrium

To showcase the effects mentioned above, I implemented a simple 2D numerical simulation of the Grad-Shafranov equation. As a model, I chose a circular Tokamak with major radius $R_0 = 5.5\,\mathrm{m}$ and minor radius $r_0 = 1.5\,\mathrm{m}$. Pressure- and toroidal current-profiles over poloidal flux were chosen as sigmoid functions $p, j \propto \frac{1}{1+\exp(-ax-b)}$ (see figures 2.1 and 2.2). This limits the profiles to bounded ranges, which eliminates local instabilities in the equation. In the simulations the toroidal current density was kept fixed, while the magnitude of the pressure was varied in three steps. For the toroidal field and the pitch-angle visualizations, I chose a vacuum field distribution of $B_\phi(R) = \frac{R_0}{R} \cdot 0.5\,\mathrm{T}$, which translates into a boundary condition for $G(\psi = 0)$. Similarly, the poloidal flux function was constrained at the edge to $\psi(r = r_0) = 0$. The equation was discretized with a $\mathcal{H}^1$-conforming (standard Lagrange elements) finite-element discretization on a 50×50 mesh using the *FEniCS* toolkit[31, 32]. Interested parties can find the code under [33, released on GitHub, archived by CERN].

The most obvious effect of the increase in pressure is the Shafranov shift, visible in the flux surface shape (2.3). It is accompanied by a strong asymmetry in the toroidal current density, up to the point where the current reverses on the inboard side (figure 2.4), and an accompanying reduction in the toroidal field (2.5). This current pinch indicates that the right-most equilibrium is probably highly unstable. Concerning the toroidal magnetic field, an interesting quirk of the Grad-Shafranov equation also outlined above is the increase of the toroidal field at low plasma pressures (but finite plasma current), which then turns into the actual field decrease at higher pressures that is commonly associated with the diamagnetic effect. This can be nicely seen in the profile of the normalized toroidla field G (figure 2.6). A secondary effect of the Shafranov shift is the compression of the flux function at the outboard side and an expansion on the inboard side. Since the poloidal field is proportional to the gradient of the poloidal flux, the poloidal field increases in the outboard region and decreases on the inboard side (2.7). Together with the reduction of the toroidal field in the outboard region, this leads to a strong imbalance of the local pitch angle $\alpha = \arctan\left(B_{\mathrm{pol}}/B_{\mathrm{tor}}\right)$ (figure 2.8).

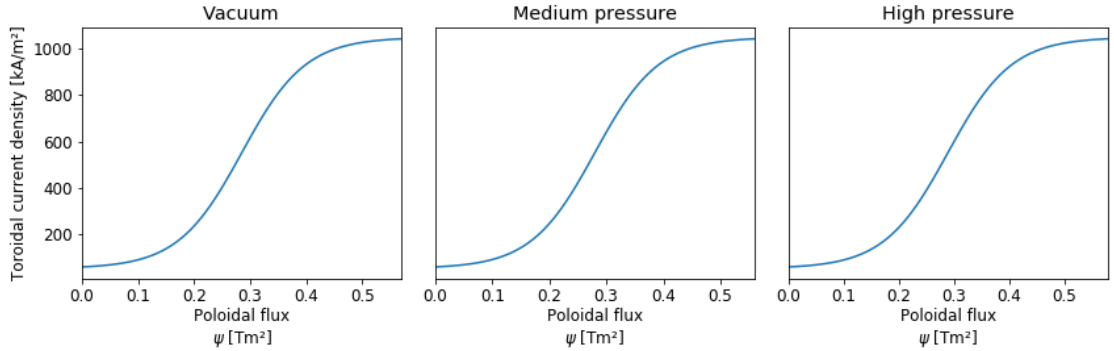

Figure 2.1: Toroidal current-density profiles (flux-surface averaged) against poloidal flux chosen for the example Tokamak simulations

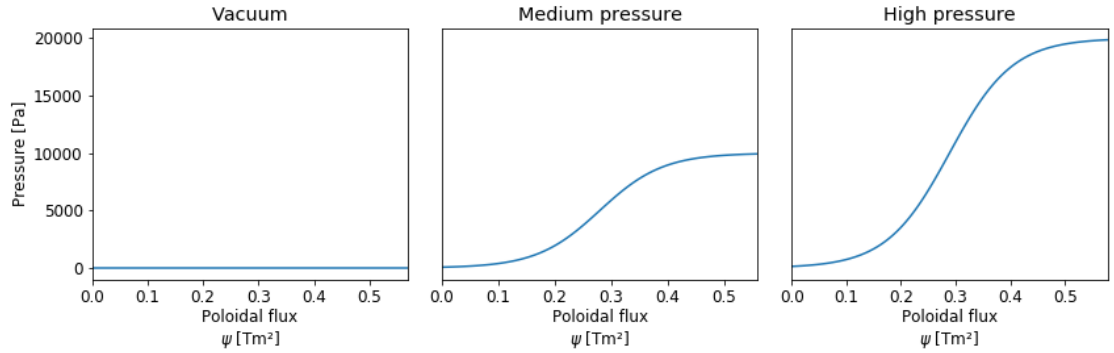

Figure 2.2: Pressure profiles against poloidal flux chosen for the example simulation of the Grad-Shafranov equation.

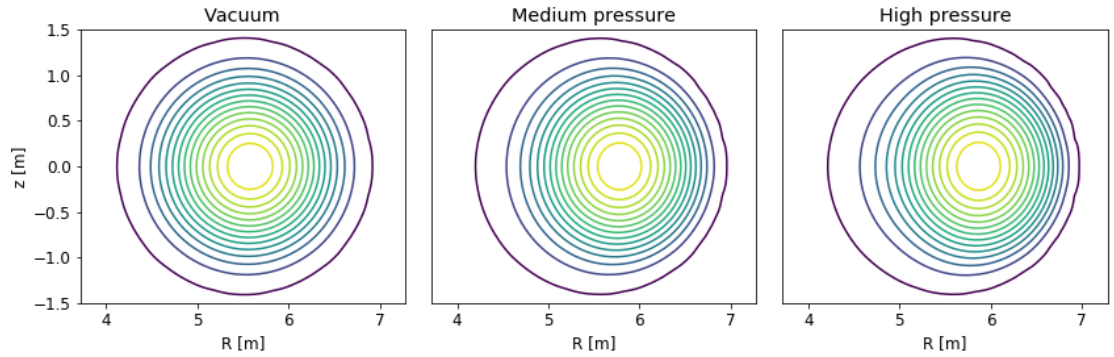

Figure 2.3: Flux surfaces obtained for the three simulated pressure cases in the Tokamak simulation.

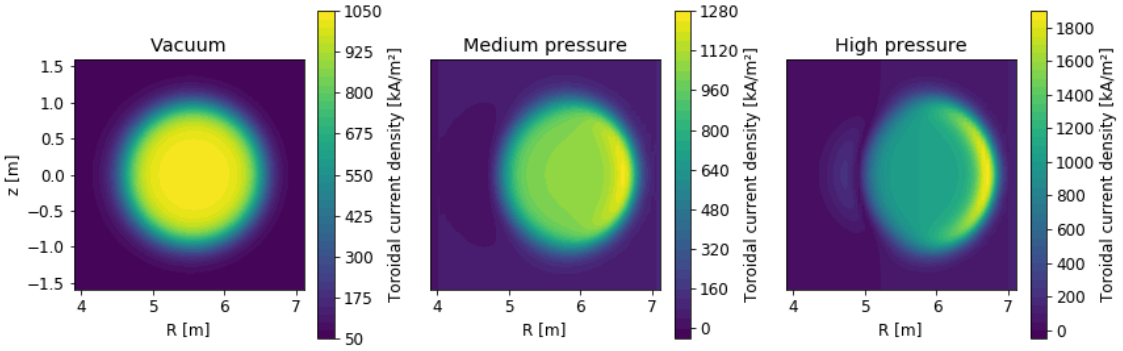

Figure 2.4: Absolute magnitude of example Tokamak toroidal current densities obtained for the three different simulated cases

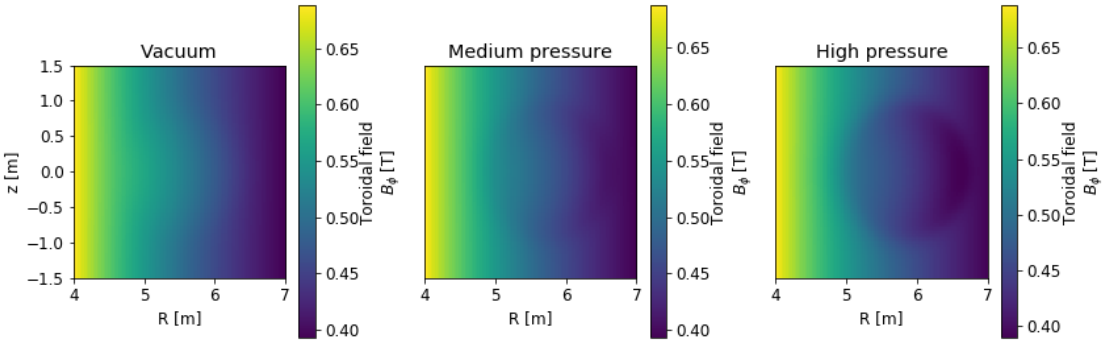

Figure 2.5: Example Tokamak toroidal magnetic fields obtained for the three different simulated cases assuming $B = \frac{R_0}{R} \cdot 0.5\,\mathrm{T}, R_0 = 5.5\,\mathrm{m}$ at the edge

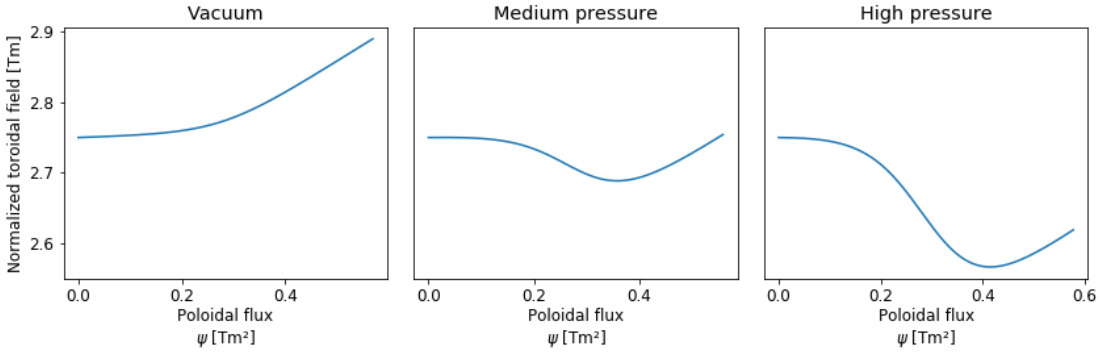

Figure 2.6: Profile obtained for the normalized toroidal field (the G-term) assuming $B = \frac{R_0}{R} \cdot 0.5\,\mathrm{T}, R_0 = 5.5\,\mathrm{m}$ at the edge.

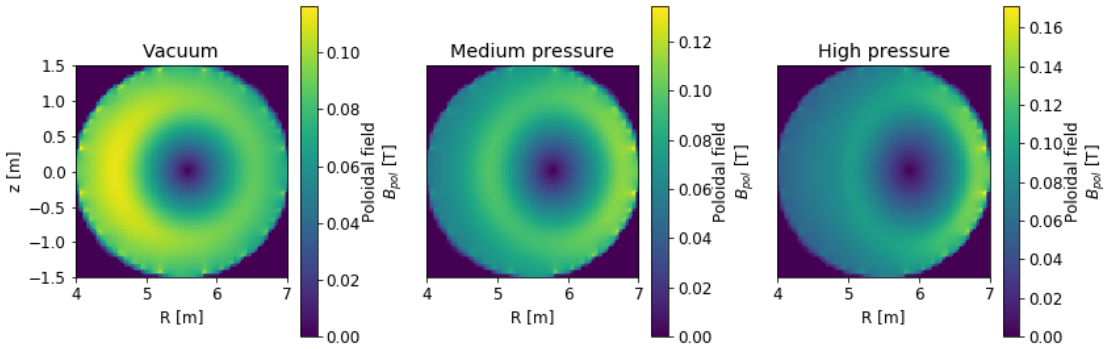

Figure 2.7: Example Tokamak poloidal magnetic fields obtained for the three different simulated cases

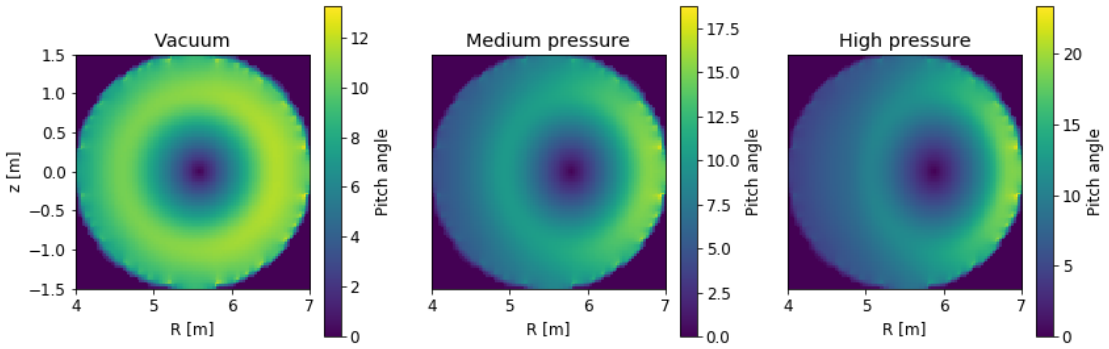

Figure 2.8: Pitch angle distribution (in degrees) of the example Tokamak for the three simulated cases

2.3 Island formation and stochastization effects

Many magnetic topologies contain magnetic island structures similar to the structures in W7-X's island divertor. Generally, these islands appear whenever the toroidal and poloidal mode numbers n and m of a radial magnetic perturbation $\Delta B_r \propto \cos(\phi_0 + n \cdot \phi - m \cdot \theta)$ (with ϕ being the toroidal and θ being the poloidal angle) interact with a magnetic surface. To allow for these interactions to interfere constructively, the magnetics surface's *rotational transform* ι (ratio of average poloidal to toroidal angle change) must fulfill the resonance condition $\iota = {}^{n}/_{n}$. Whenever this is the case, an island chain with m poloidal islands will form on this flux surface.

At first order, these islands will have clean nested flux surfaces. However, once these island structures start to overlap, the intersecting region becomes chaotic. Since the magnetic island size usually depends on the plasma beta, this makes stochastization effects an important beta-related effect. This section will shortly discuss a popular toy model for stochastization, the kicked rotator model, and then will give a more practice-oriented example for stochastization characteristics (and avoidance strategies) on a practically used Stellarator type.

2.3.1 The Kicked Rotator Model

The simpliest toy model to study is the kicked rotator model, which is given by the Hamiltonian $\mathcal{H}(\theta, p, t) = \frac{p^2}{2} + K\cos(\theta)\sum_{i=-\infty}^{\infty}\delta(t-i)$. In this model, θ is the angle of a massive rod and p is its angular momentum. Periodically, the rod is kicked at its end in a fixed direction with magnitude K. When sampled at integer time intervals (right before every kick), the angular momentum p is only relevant for the angle's time series up to a multiple of 2π. Therefore, the whole phase space of this time series fits in the $[0, 2\pi]^2$ window and its timeslices at $t = \{2\pi n | n \in \mathbb{N}\}$ can be represented by the time series

$$\begin{aligned} \theta_{t+1} &= \theta_t + p_{t+1} \\ p_{t+1} &= p_t + K\cos(\theta_t) \end{aligned} \tag{2.3}$$

which is also called the *standard map*. Figure 2.9 shows the phase space surfaces formed by the kicked rotator's trajectories. Between 0.9 and 1.0 lies the critical K value at which the two resonances in phase space start to overlap. As K increases beyond this threshold, the overlapping region is transformed into a stochastic region, where field-lines mostly do not follow any nested structures anymore.

2.3.2 Plasma-beta driven edge stochastization

The phenomenon of stochastization is not limited to the growth of already existing islands. The harmonic magnetic field components which drive the creation (and overlap) of islands can often be purely driven by MHD equilibrium effects. Figure 2.10 shows an example of how stochastization can practically affect a Stellarator. In the shown system (which is a simplified model for a Heliotron-type Stellarator like LHD), large beta plasmas exhibit a severe degradation of the magnetic surfaces in the edge, which not only leads to a significant loss of confined plasma volume but also creates a strong deviation in scrape-off layer structure. Since the magnetic islands originate

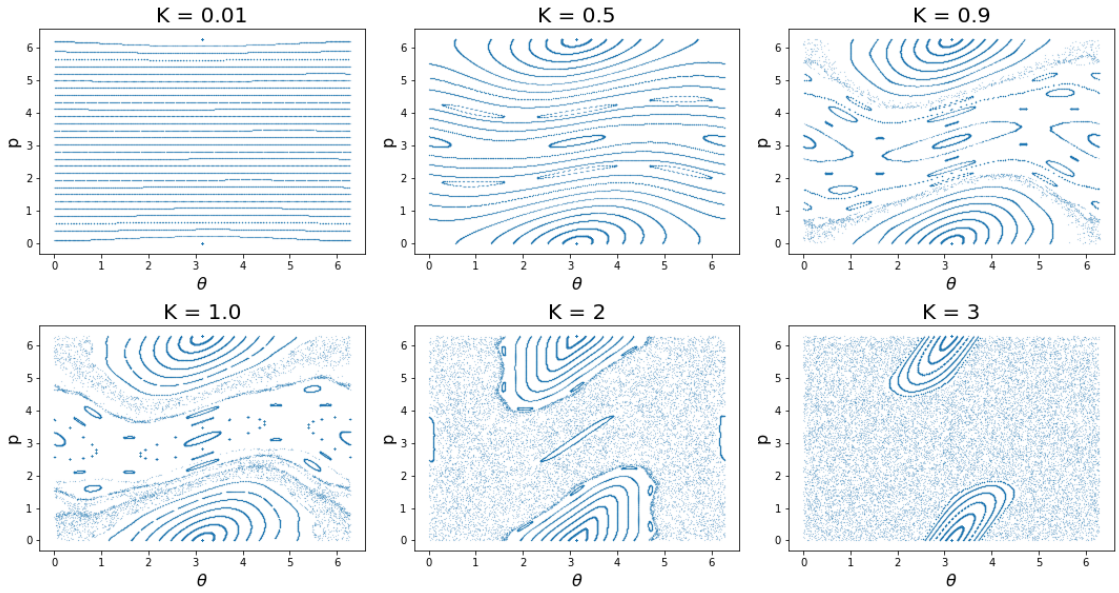

Figure 2.9: Poincaré map (see equation 2.3) of the kicked rotator for different values of the kick strength K. Coordinate axes correspond to the phase space of the kicked rotator.

from a resonant flux surface, and their width is inversely proportional to the magnetic shear, there are three strategies to design robust magnetic configurations for high plasma beta:

1. Avoid rational flux surfaces with ι resonant to magnetic Fourier components driven by plasma beta
2. Have a sufficient magnetic shear around these surfaces in order to limit the growth of magnetic islands due to the resonant magnetic components
3. Design the vacuum geometry to contain Fourier components opposite to the ones driven by plasma pressure so that high-β-operation annihilates existing magnetic islands instead of creating new ones

In Wendelstein 7-X, the second option directly opposes the requirements for an island divertor and the nature of its low-shear optimization. Option one can be implemented through scanning the ι-range of the core (by adding an additional toroidal field), while option three is a component of the standard magnetic configuration. In this configuration, there is the potential of a magnetic $\iota = 5/6$-surface appearing in the core. The vacuum $n/m = 5/6$-component was design such that it would cancel out against the plasma contribution at $\beta_{\text{axis}} = 5\%$, suppressing the associated island at high-beta operation.

2.4 Summary

This chapter gave an elementary introduction to the theoretical foundations of MHD equilibria and discussed the effects that should be expected when transitioning from a vacuum-magnetic topology to a finite-pressure plasma. The first principles of this theory were briefly introduced, and then the Grad-Shafranov equation for axisymmetric systems was derived from them in a covariant approach

in cylindrical coordinates. The most important effects, the diamagnetic effect and the Shafranov shift, were introduced by numerically examining a simple model Tokamak. The characteristical scale of such effects, the plasma beta, was introduced in multiple variants. Afterwards, the effects of magnetic field stochastization by overlapping magnetic islands was brought into play via a simple toy model. The possible interactions between stochastization processes and beta-driven islands - and general ideas on avoiding and mitigating their effects - were shown based on a practically relevant Stellarator design.

With the end of this chapter, this thesis will close its focus on simple and instructive models, and will instead proceed to the more complex models required for real-world Stellarators. In particular, the next chapter will deal with a more detailed modeling approach suitable for complex geometries such as Wendelstein 7-X, which can be used to derive finite-beta magnetic field, analyze their structure, and then make heat-load predictions for plasma-facing components.

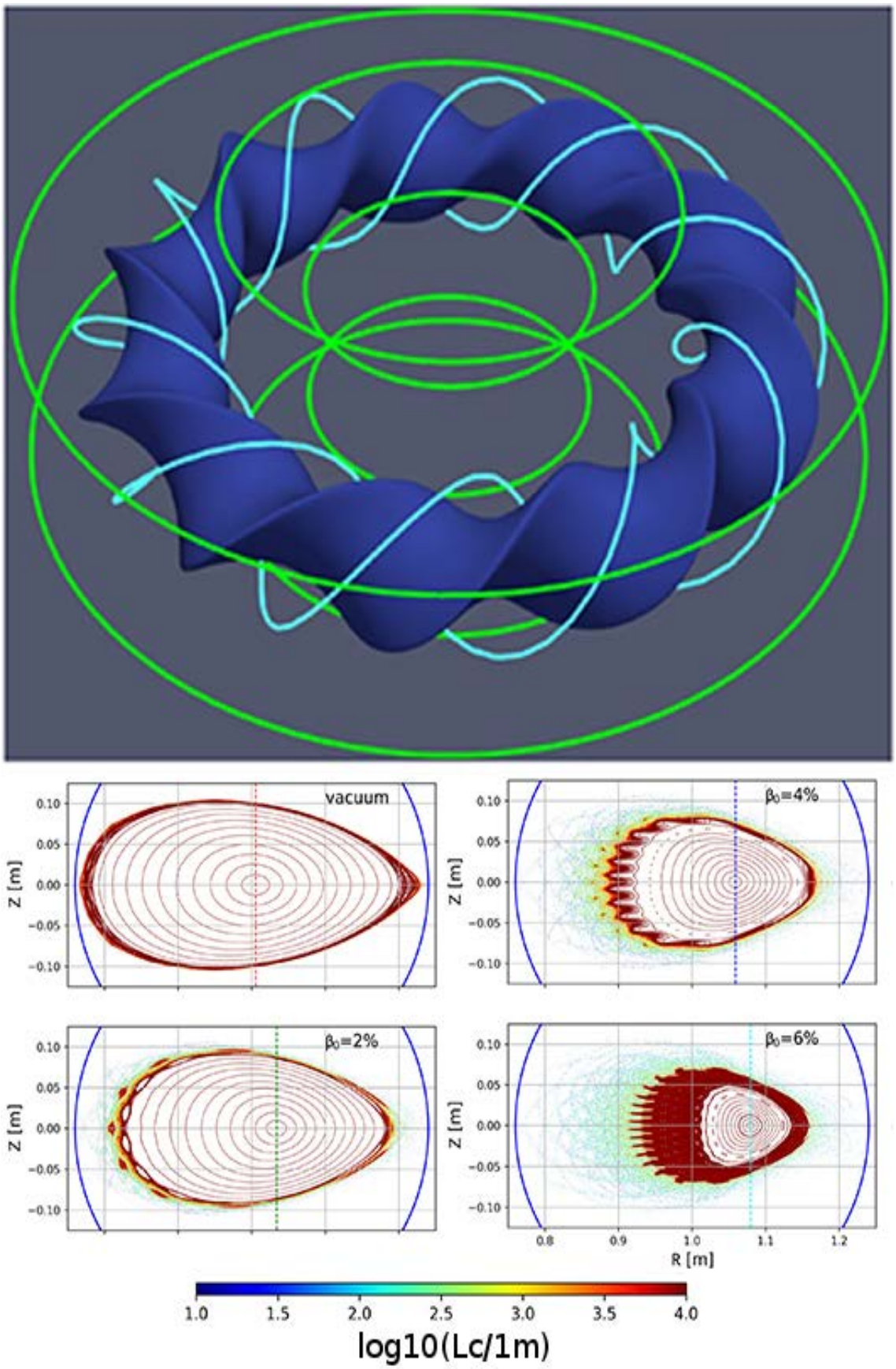

Figure 2.10: Edge stochastization of a simplified Heliotron stellarator (left) at various central plasma beta values (right). The colorbar indicates the decadic logarithm of the connection length onto the plasma-facing components, the dashed line highlights the Shafranov shift of the magnetic axis. Adapted from [34]

3 Numerical codes for finite-beta equilibrium and heat-load modeling

In order to understand the internal dynamics of pressure-driven changes in the edge plasma, one must first understand the dynamics of the primary shaper of the plasma, the confining magnetic field. While analytical solutions can be obtained for simple cases, such as restricted subsets of the Tokamak configuration space, generally, a numerical solution of the equations is required. On the coarsest level, MHD equilibrium solvers for fusion devices can be divided into two branches:

- Flux-surface based solvers: These solvers approximate MHD equilibria in a restricted subspace, namely the subset of equilibria with nested flux-surfaces. The flux surfaces are usually described as isocontours of a 3D flux surface label function, and the magnetic field is fixed by parametrizing magnetic flux functions over the flux surface label. Since this approach is very close to an explicit vector potential, it yields stable and fast discretization schemes (the equations are closely related to vectorial Poisson equations, which are outstandingly well-behaved).

- Full-field solvers: These codes rely on a more explicit description of the equilibrium field. Oftentimes, they directly apply standard discretization methods (finite difference, finite volume, finite element) directly on the field and related equations. These codes can represent a far wider space of possible equilibria, including those with stochastization and magnetic islands. Unfortunately, the improved representational capability comes at the cost of massively increased resource demands. Where flux-surface codes can usually run in a few minutes on a single PC, full-field codes are a strict supercomputer-only domain, not least due to the large amounts of memory required.

These codes then need to be integrated into a pipeline of post-processing systems, which analyze the finite-beta magnetic configurations to obtain experimentally relevant information (such as synthetic diagnostic data, but also un-observable information). A full overview of the pipeline applied in this thesis is shown in figure 3.1. The pipeline is divided into three stages. The first stage is the computation of finite-beta equilibria using the equilibrium codes HINT and VMEC. The second stage is the direct and diffusive tracing of the finite-beta fields (combined with the machine geometry) to obtain Poincaré-maps, connection-length distributions, and strike-points distributions for heat-carrying test particles. The purpose of this chapter is the introduction of the individual components making up this numerical modeling chain.

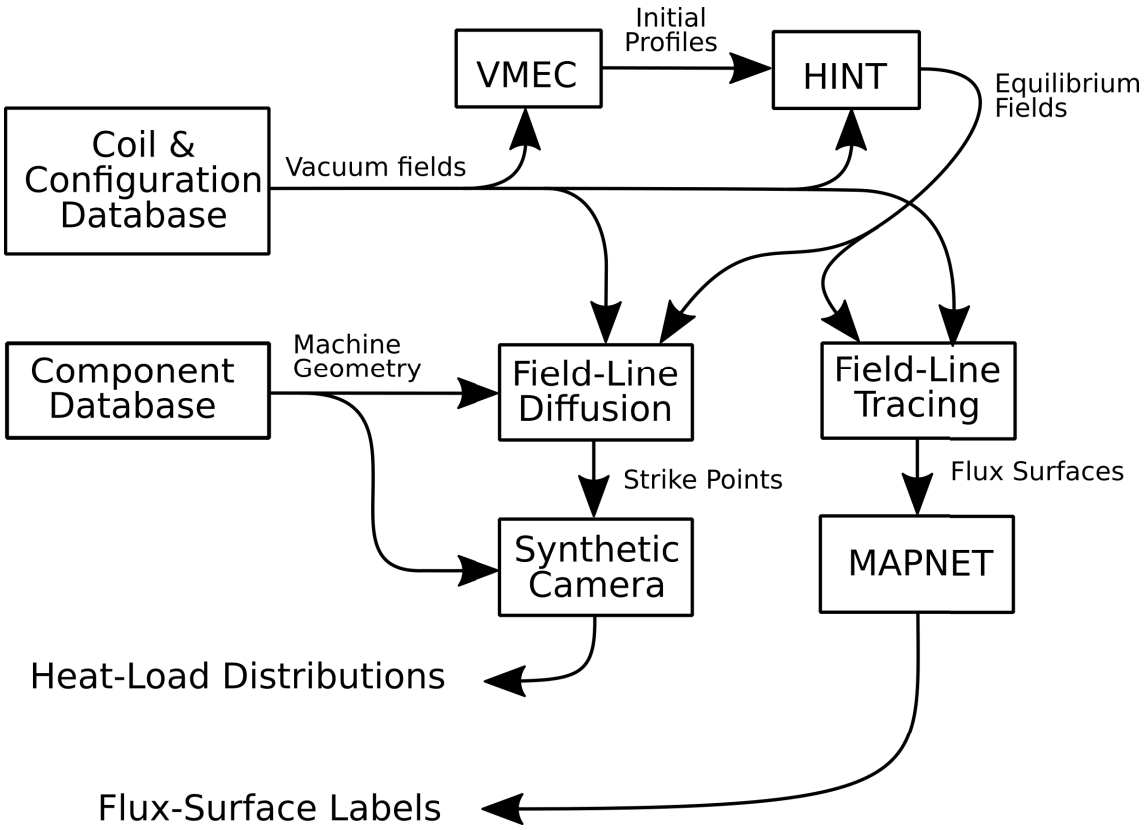

Figure 3.1: Overview of complete modeling pipeline

The following original research contributions are presented in this chapter:

- A synthetic camera approach for the conversion of Monte-Carlo samples into heat-flux distributions, which can provide high-resolution heat-flux images
- A machine learning method (more specifically: a neural network), which computes configuration-dependent magnetic surface labels compatible with divertor island structures
- The modeling pipeline into which the components presented here are assembled. This does not extend to the other components of the pipeline themselves, which are external contributions. The work-flows for bridging these codes, however, are themselves original contributions. Particular contributions here are programs for sampling VMEC outputs on HINT's calculation grid, conversion of triangle mesh geometries into HINT's solid voxel format, as well as front-end code for bridging the W7-X webservices with HINT output files.

3.1 The nestex flux-surface solver VMEC

VMEC (short for "Variational Moment Equilibrium Code") is an equilibrium solver based on a Fourier representation of flux surfaces [35]. Its speed and robustness have made it a prevalent and possibly the most widely used equilibrium code in the Stellarator community. Similar to the Grad-Shafranov approach, VMEC represents the magnetic field $\vec{B} = \vec{\nabla}\phi \times \vec{\nabla}\psi_{\mathrm{pol}} + \vec{\nabla}\psi_{\mathrm{tor}} \times \vec{\nabla}\theta^{\star}$ as a combination of a toroidal and a poloidal flux function, which inherently gives a divergence-free

field. The resulting coordinate system is similar to a toroidal coordinate system, with the minor radius being replaced by the normalized toroidal flux $s = \psi_{\mathrm{tor}}/\phi_{\mathrm{tor,max}}$ and the poloidal coordinate θ being perturbed so that field lines are straight lines in VMEC coordinates ($d\theta^\star/d\phi = \text{const.}$). The magnetic surfaces are parametrized by parametrizing the mapping from flux-surfaces to cylindrical coordinates $(\phi, s, \theta) \to (\phi, R, z)$ as Fourier expressions in ϕ and θ (and interpolation of the Fourier coefficients in s). In this parametrization, VMEC then searches for a minimum of the potential energy $W = \int \frac{|\vec{B}(\vec{x})|^2}{2\mu_0} + \frac{p(\vec{x})}{\gamma - 1} d^3\vec{x}$ using a steepest-descent method. VMEC supports two kinds of operational modes. In fixed-boundary mode, the outer-most flux surface is specified as an input and respected by the equilibria. In free-boundary mode, VMEC attempts to construct a boundary surface perpendicular to the vacuum field, which can give a better fit if the field contains topological structures near (but not at) the outermost surface.

VMEC's speed comes from this very efficient Fourier representation of the flux surfaces. However, this representation can not capture non-nested topologies, such as island structures of stochastic regions. It can, therefore, not compute self-consistent equilibria for the edge region of W7-X but remains the preferred option for equilibrium calculation in W7-X's plasma core, which mostly retains the nested flux surface structure. This limitation can be partially overcome by extrapolating the plasma response beyond the VMEC domain and combining it with the vacuum field [36, 37]. This approach is, however, not self-consistent in the edge. In particular, the distortion of the outermost flux-surface by the modified island structures will not be taken into account in the equilibrium calculations.

3.2 The full-field 3D MHD code HINT

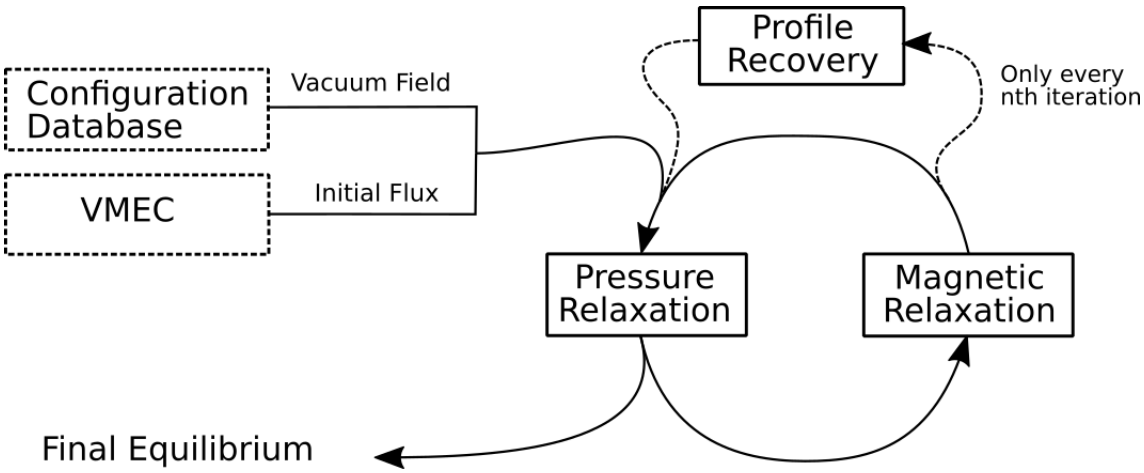

Figure 3.2: Structure of the HINT code. Dashed boxes indicate external data sources

HINT code is a full-field 3D MHD equilibrium solver designed to calculate stellarator equilibria given requested pressure- and current-profiles [38, 39]. It represents the field using a 2nd-order symmetric finite difference scheme, which is exact up to the 5th derivative. HINT uses a two-step scheme, where it alternates between a magnetic relaxation and a pressure-relaxation step. Pressure relaxation is performed by averaging the pressure along magnetic fieldlines. If the distance is on the order of, or below, the mean free path length, this process approximates perpendicular diffusion

along the field-line. In the equilibrium case, this implies that $p = \text{const.}$ on all closed flux surfaces, which corresponds to the $\gamma \to \infty$ limit of the MHD equilibrium equations. Magnetic relaxation is achieved by integrating the resistive MHD equations over time. In order to bring the inertial and resistive time-scales onto a similar level, the resistivity is assumed at an un-physically high level. This speeds up the speed of the magnetic relaxation without modifying the equilibrium field (as the equilibrium conditions are independent of the plasma resistivity). As HINT uses a direct formulation for the magnetic field and does not rely on the vector potential, it has to explicitly preserve the divergence freedom of the magnetic field. It does so by adding an additional $\kappa \cdot \vec{\nabla} \cdot \left(\vec{\nabla} B\right)$ term into the time derivative that annihilates emerging magnetic monopoles.

As the magnetic field relaxes, the pressure averaging process ensures consistency of the pressure distribution with the magnetic topology. It does, however, not ensure consistency of the pressure profile with the requested profile. Especially during the early iterations, where the field changes the most, the pressure profile is smeared out by the repeated averaging over different flux surfaces. Therefore, the requested pressure profile has to be periodically recovered. Figure 3.2 shows an overview of these three different processes, which are detailed below.

3.2.1 Magnetic Relaxation

Magnetic relaxation is performed in HINT by integrating the resistive MHD equations. For the magnetic field, it uses the equations

$$\begin{aligned} \frac{dB_1}{dt} &= \nabla \times E + \kappa \nabla \cdot \nabla B \\ E &= v \times B - \eta \left(j_1 - j_n\right) \\ B &= B_0 + B_1 \\ j_1 &= \mu_0^{-1} \nabla \times B_1 \\ j_n &= \mu_0^{-1} \nabla \times B_0 \\ v &= v_0 + v_1 \end{aligned}$$

with the vacuum field B_0, the plasma field B_1, the anisotropic artificial resistivity η, the stationary flow v_0 and the dynamic flow v_1. The resistivity η can be specified separately for the plasma- and wall-domain, and is averaged once over a local 3×3 grid by HINT to prevent sharp transitions.

Like the magnetic field, the flow is decomposed into a stationary and a dynamic component, and only the dynamic component is evolved over time:

$$\begin{aligned}
\frac{dv_1}{dt} &= \rho^{-1} f_B F \\
F &= -v \cdot \nabla v - \nabla p + j \times B \\
&+ \nu_{0,\text{para}} \hat{B} \left\langle \hat{B}, V_0 \right\rangle \\
&+ \nu_{0,\text{perp}} \left(V - \hat{B} \left\langle \hat{B}, V_0 \right\rangle \right) \\
&+ \nu_0 V_0 + \nu_1 V_1 \\
V_0 &= \Delta\nu_0 \\
V_1 &= \Delta\nu_1
\end{aligned}$$

with the background and foreground viscosities ν_0 and ν_1 and the anisotropic background viscosities $v_{0,\text{para}}$ and $v_{0,\text{perp}}$. f_B (referred to in the code as *factorb* or *factorc*) is a stabilization factor that is set to 0 inside the coils (it is determined by thresholding the vacuum field and its current and then smoothing) in order to prevent a build-up of flow in the coils. Both equations are integrated together over a fixed time step-size with a high-order Runge-Kutta integrator. A fixed number of magnetic relaxation steps are performed per macrocycle, where each time relaxation step is a single time step of the integrator.

The boundary conditions enforced during the time-stepping process are Dirichlet conditions on the normal field and flow:

$$\begin{aligned}
\frac{dv}{dt} \cdot n &= 0 \\
\frac{dB}{dt} \cdot n &= 0
\end{aligned}$$

In addition to the above relaxation scheme, HINT relies on a mixing-smoothing scheme for flow stabilization. Smoothing is performed by partial convolution with a 1D kernel along every direction

$$v_1 \leftarrow \lambda v_{\text{ref}} + (1 - \lambda)(v_1 - v_{\text{ref}}) * K$$

with $\lambda = 0.375$ and K having the fixed representation $\frac{1}{6}[-1, 4, 0, 4, -1]$ on the finite-difference grid. The reference flow v_{ref} is copied from v_1 periodically.

3.2.2 Pressure relaxation

After magnetic relaxation, the 3D pressure distribution has to be modified to fulfill $\vec{B} \cdot \vec{\nabla} p \approx 0$ of the new magnetic field. HINT achieves this by averaging the field along a fixed distance. The field-lines traced for averaging are started from the grid points and are traced in both directions. The field-lines are not traced with a fixed 3D step size or a fixed multiplier of the vacuum field. Instead, the code performs a fixed step size in the toroidal angle on each Runge-Kutta iteration. If any direction encounters the wall domain during tracing, the contribution of that direction to the average pressure is completely set to 0 (but the other direction can still contribute).

When focusing on core plasma physics, especially on islands appearing in the plasma core, the averaging length of the pressure relaxation process should be set high enough to connect both ends

of the inner islands. This is, however, undesirable when analyzing divertor islands, as the truncation of the pressure will prevent the buildup of pressure gradients at the edge. In practice, even values orders of magnitude shorter than the connection length ($L_{\text{in}} = 10\,\text{m}$ vs. a connection length of 250 m) still make it difficult to build up significant edge pressures, as the repeated application of pressure relaxation acts similar to a parallel diffusion process. This value should, therefore, be chosen as low as possible without compromising the flux-surface alignment of the isobaric surfaces in the core. For the results presented in this thesis, the edge profiles were not matched exactly, and the averaging length was chosen as 2 m.

3.2.3 Pressure profile reconstruction

The pressure relaxation step alone has a tendency to overly dissipate pressure gradients, especially during the early phases where the magnetic field varies a lot between pressure relaxation steps. Therefore the requested pressure profile has to be periodically re-established. HINT achieves this with a three-step process:

1. Build a histogram of the toroidal magnetic field over the pressure
2. Use this histogram to calculate the toroidal magnetic flux enclosed by each isobaric surface on every grid point
3. Re-calculate the pressure distribution from the 3D flux distribution and the requested pressure profile

The pressure profile is calculated from a profile shape and a requested plasma beta. The target pressure is estimated from the requested axial plasma beta and the on-axis magnetic field in the $\phi = 0$ plane.

3.2.4 Required Inputs

In order to perform its calculation, HINT must be given the following information:

- The 3D vacuum field must be explicitly passed. Not only is it used as the initial field for the calculation, but it also contains the information necessary to derive the f_B factor for flow stabilization. This factor is derived from coils detected in the magnetic domain, which is achieved by analyzing the vacuum current distribution
- Additionally, HINT requires an initial magnetic flux distribution to calculate its starting value for the 3D pressure distribution. The inputs were here created by sampling the 3D flux distribution of VMEC equilibria. In cases of short L_C with a high number of repeated relaxations, the outputs of HINT were found to be remarkably stable against perturbations in this parameter, to the point where VMEC equilibria from different configurations could be used as an input and would yield nearly the same result (if the vacuum field was kept the same). It should be stressed that this high degree of stability can not be expected for higher L_{in} configurations, where the initial flux distributions will quickly lock in the shape of the pressure profile.
- Finally, HINT requires a description of the machine geometry. Since triangle-line intersection tests are numerically complex and expensive, HINT instead relies on a voxel description of the

machine geometry. In this work, the machine geometry was voxelized by casting rays from flux surfaces of a VMEC equilibrium towards the target point in question (most commonly the surfaces at normalized toroidal flux $s = 0$ and $s = 0.2$ in standard magnetic configuration). If any of the rays were to intersect a triangle of the machine geometry, the corresponding voxel would be marked as "in-wall", otherwise it was assigned to the plasma domain. This scheme produces high-quality solid volume representations of the plasma boundary.

When calculating the flux distributions from VMEC equilibria, care should be taken on how the coordinates are mapped. VMEC uses a non-linear coordinate system (ϕ, s, θ) with toroidal slab angle ϕ, normalized flux s, and poloidal angle θ, which can be easily transformed to cartesian coordinates by a Fourier series. The inverse transform form cartesian into VMEC coordinate space, however, is highly non-trivial and usually not analytically solvable, so a numerical inversion scheme has to be used instead. Since VMEC's coordinate systems are polar, standard Newton-Raphson methods are unsuitable near the axis. This problem was solved by inverting the transform from virtual slab coordinates $(\phi, s\cos(\theta), s\sin(\theta))$ to slab coordinates (ϕ, R, z), which is stable also around the magnetic axis, and would recommend interested researchers to do the same.

3.3 Divertor heat load modeling

At lowest order, the heat loads on plasma-facing components can be approximated by a convective-diffusive streaming model. Test particles are instantiated on the closed surfaces of the plasma and stream along the field-line. To enable the particles to leave the confined plasma, a small Brownian motion is superimposed onto the particle trajectories. In its discrete form, this model is called the *field-line diffusion* model. A naive implementation would have the particle travel a very short distance and then apply a fixed variance Brownian motion step. A straight-forward numerical optimization is to first sample the mean free path from an exponential distribution $L \leftarrow p(L = l) = \frac{\exp(-\lambda l)}{\lambda}$, propagate this distance along the field-line, and then sample the Brownian motion conditioned on the travel distance $\Delta x \leftarrow p(\Delta x = s) = \frac{1}{(2\pi)^{3/2}\sigma(l)} \exp\left(-\frac{|\Delta x|^2}{\sigma(l)^2}\right), \sigma(l) = \sqrt{D \cdot \frac{l}{v}}$. This work relies on the field-line diffusion implementation provided by a web-service installed in the Institute of Plasma Physics in Greifswald [40].

Like all test-particle Monte-Carlo models, and unlike a numerical fluid model, this model does not immediately yield a heat-flux approximation. Instead, it constructs a three-dimensional cloud of impact points which needs to be projected onto the machine geometry and binned to obtain heat-flux predictions. Usually, these approaches require a manual mapping of the machine geometry into 2D space. This is a long-winded and time-consuming manual process. A newly developed approach developed during this thesis is a synthetic camera-based binning concept. All particles are transformed into the camera space and then binned in the 2D grid representing the camera image. The resulting distribution can then be multiplied with a (pixel-dependent) conversion factor to obtain the heat-load distribution. The mathematical concepts underlying this model are as follows:

- Transformations in 3D space can be modeled as matrices in the 4D *homogenous coordinate* space. In this space, 3D points are represented as $(x, y, z, 1)$ and distance / direction vectors as $(x, y, z, 0)$. This space is well defined in the sense that distances and directions may be

summed and scaled, and 3D points can be subtracted to yield a distance. Likewise, adding distance to a 3D point is also legal. In this space, translations, rotations, shear transforms, and similar spatial operations can be expressed as 4×4 matrices with the last row always being $(0, 0, 0, 1)$.

- Projective camera transforms (which are no pure spatial transforms) can be, in homogenous coordinates, expressed by a spatial transform, a matrix of the form $M = \begin{pmatrix} 1 & 0 & 0 & 0 \\ 0 & 1 & 0 & 0 \\ 0 & 0 & 1 & 0 \\ 0 & 0 & \alpha & 0 \end{pmatrix}$ and a non-linear renormalization operation $(x, y, z, w) \to (x/w, y/w, z/w, 1)$.

- If a surface is modeled as a function from a surface parameter space to 3D space $f : (u, v) \to (x, y, z)$ and a projective transform form 3D space to screen $g : (x, y, z) \to (x_s, y_s)$, then the surface area covered by a pixel is in first order approximated as the ratio between the surface element $\left|\frac{df}{du} \times \frac{df}{dv}\right|$ and the screen element $|\det(D_{g \circ f})|$ (assuming that a pixel is 1×1 in screen coordinates)

- The normalized heat-flux on a surface element represented by a pixel is given as $P_{\text{norm}} = \frac{n_{\text{pix}}}{n_{\text{tot}}} A_{\text{pix}}^{-1}$, where n_{pix} is the number of test particles in the virtual screen pixel, n_{tot} the total number of test particles that reached a PFC, and A_{pix} is the surface area covered by this pixel.

This approach allows the fast construction of heat-load images from varying camera angles, fields of view, and positions. It also has the distinct advantage of working well on non-planar geometries that can not be easily un-rolled (e.g. close-up views of gaps in divertor targets). Additionally, because such a model re-uses calculations commonly performed in video games, it should also map extremely well onto GPU hardware.

3.4 Machine-learning assisted magnetic surface coordinate reconstruction in 3D magnetic fields

A major challenge in experimental plasma physics is the task of combining the measurements from different diagnostics. Most diagnostics are specialized in measuring one or two plasma parameters and have unique sight-lines. Plasma-facing camera diagnostics, such as bolometers, measure line-integrated data, while other diagnostics (such as Thomson scattering or reciprocating Langmuir probes) measure along a specific path. Physical conclusions usually require more parameters than can be provided by a single observation system. Generally, there are two methods to achieve this.

The gold standard for physical evaluation is full 3D modeling of the involved physical processes. The model can then be iteratively adapted to match the plasma parameters to the observations provided by the available diagnostics. This approach allows a full reconstruction of the plasma and provides a large amount of additional information about the modeled experiment. It faces, however, two challenges. The first issue comes from the fact that simulation codes often implement simplified models, which can sometimes not provide a full match of the observations in question. This is not a major issue with well-established and extensively benchmarked models but can become a hindrance

when investigating novel (and consequentially poorly understood) physics. An additional problem is the cost of such a process, especially in a complex magnetic geometry like W7-X. Full simulation requires extensive computing resources and expert operators. Additionally, large scale observation fitting usually not only combines multiple diagnostics but also requires the combination of multiple modeling codes. Coupling models which make different, and sometimes conflicting, assumptions about the studied system requires long attention windows by highly trained experts on both the codes and the diagnostics, which is a far higher expense than the computational resources needed.

Many cases, however, do not require a full reconstruction of the target system. A large number of applications only want to either combine information about related magnetic surfaces or want to compare observations of the same plasma parameter at different spots on the same magnetic surface. A full model is neither necessary nor feasible for these projects (e.g. due to time constraints on the analysis). They therefore usually take approaches based on the magnetic geometry of the plasma. The most common approach is to provide a label for magnetic surfaces and then plot measured plasma parameters over this flux surface label. The most popular labels are the s coordinate of VMEC equilibria (which assume nested flux surfaces) and the average distance between a field-line and the magnetic axis. Unfortunately, both of these labels are only suitable for the plasma core and do not provide flux-surface aligned (which is broken in the VMEC equilibria) and distinct (which is lost for the average distance to the axis) magnetic surface labels in the plasma edge of W7-X, which is dominated by magnetic islands.

This sub-chapter introduces a novel approach to this problem of mapping coordinate construction, which borrows heavily from the field of machine learning.

In particular, the mapping coordinate function will be approximated through a neural network, which has several benefits. The trained neural network is a simple, small, feed-forward network. It can therefore be easily shared between researchers and evaluated quickly (in real-time if using a Graphics Processing Unit). Additionally, neural network libraries routinely provide support for automatic algebraic differentiation, as it is required for their training processes. The network can therefore be differentiated in the configuration parameters to quickly evaluate the "best-matching" configuration under any required set of constraints. This is particularly of interest for diagnostics with many independent measurements, which can then leverage fast gradient-based optimizers to find the most consistent magnetic configuration for their observations. Additionally, the network can also be trained to produce secondary outputs, for example an estimation on whether the queried point lies on an open or closed field line.

3.4.1 Definition of an island-aware radial coordinate

For most considerations in nuclear fusion experiments (with the notable exception of parallel flow in open field lines such as divertors), plasma parameters can be assumed as constant along field lines. When comparing positions in the magnetic geometry, we would therefore like to neglect the parallel component of the distance and only rely on the remaining perpendicular component of paths between points. Based on this motivation, we can define the following quantities for a given magnetic field $\vec{B} : \mathbb{R}^3 \to \mathbb{R}^3$:

- The *perpendicular path length* $l_\perp$ of a smooth (arbitrarily differentiable) path $\gamma : [0, 1] \to \mathbb{R}^3$ between points p and q ($\gamma(0) = p, \gamma(1) = q$) is defined as the integral of its parallel differential component $l_\perp[\gamma] = \int_0^1 \left| \vec{B}(\gamma(\tau)) \cdot \frac{d\gamma}{d\tau}(\tau) \right| d\tau$

- The *perpendicular distance* of two points p and q is defined as the infimum of all possible such path lengths $d_\perp(p,q) = \inf\{l_\perp[\gamma] \,|\, \gamma \text{ smooth path from } p \text{ to } q\}$
- The *perpendicular distance of two magnetic surfaces* S_1 and S_2 (where a magnetic surface is defined as a set $S \subset \mathbb{R}^3$ with $\forall p,q \in S : d_\perp(p,q) = 0$) is defined as $d_\perp(S_1,S_2) = \inf\{d_\perp(p,q) \,|\, p \in S_1, q \in S_2\}$
- The *perpendicular radius* $r_\perp(p)$ of a point p is defined as its perpendicular distance $d_\perp(p,p_{\mathrm{ax}})$ to a pre-defined reference point p_{ax} on the magnetic axis.
- The *perpendicular radius* $r_\perp(S)$ *of a magnetic surface* S is defined as the perpendicular radius of an arbitrary point $p \in S$ (this is independent of the choice of point)

It should be noted that the last definition is independent of the choice of reference point on the magnetic axis. $d_\perp$ is symmetric and fulfills the triangle inequality ($d_\perp(a,b) \leq d_\perp(a,c) + d_\perp(b,c)$). Unfortunately, the calculation of $r_\perp$ as formulated here is numerically infeasible. It can, however, be approximated for a finite set of magnetic flux surfaces through the following three-stage approach:

- Calculate the distance of closest mutual approach between all given magnetic surfaces
- Calculate the distance of all magnetic surfaces to the magnetic axis
- Calculate the shortest path from the magnetic axis to each surface, which can be achieved by hopping from one surface to the next (can be calculated from the above two points)

With this calculation, approximations for $r_\perp$ can be obtained on each of the pre-determined magnetic surfaces.

In a case of well-aligned nested flux surfaces, the shortest path from one flux-surface to another is usually orthogonal to the flux-surface in-between. In such a case, the difference in perpendicular radius should be approximately equal to the perpendicular distance of the surfaces. This allows us to define topologically related zones $Z_i \subset \mathcal{P}\left(\mathbb{R}^3\right)$, which are sets of flux surfaces that fulfill the consistency relation

$$\forall S_1, S_2 \in Z \quad : \quad |d(S_1,S_2) - |r_\perp(S_1) - r_\perp(S_2)|| \leq \epsilon \tag{3.1}$$

with a mismatch tolerance parameter ϵ (which defines the minimum scale of structures that should be partitioned out into separate zones) and the real-space surface distance $d(S_1,S_2) = \inf\{|p-q| \,|\, p \in S_1, q \in S_2\}$. In addition to the perpendicular radius coordinate, the network will also be tasked to assign a zone label to each input flux surface in order to identify topological fault-lines (e.g. island separatrices) in the magnetic structure.

3.4.2 Training of the mapping network

Training of neural networks and other surrogate models involves three components which need to be assembled:

- The data-flow and computation pattern, as well as the parameters available for tuning by the optimizer, have to be defined
- Input data for the training loop have to be provided

- A loss function which is optimized by the training framework needs to be specified

The particular approach towards each of these sub-tasks is outlined below.

3.4.2.1 Structure of the surrogate neural network

The mapping network for Wendelstein 7-X takes as an input the cartesian coordinates of the requested point and 10 parameters describing the magnetic configuration. The cartesian coordinates are then converted into $R = \sqrt{x^2 + y^2}, \phi = \arctan\left(y/x\right), z$ coordinate, and ϕ is further converted into $\sin\left(5\phi\right)$ and $\cos\left(5\phi\right)$, which enforces the 5x. The raw x, y and ϕ values are then dropped. This coordinate representation enforces the five-fold symmetry of W7-X and assists in the stability of the training. Furthermore, all current-like parameters (including coil-, but also toroidal plasma current) are then normalized to the mean non-planar coil current to model equivalence of configurations under scalar magnetic field scaling.

Afterwards, the inputs are passed to a number of dense layers with a "leaky ReLU" (leaky rectified linear unit) [41, 42] activation function. Each of these layers amounts to a dense $d \times d$ matrix multiplication, followed by an element-wise application of the leaky ReLU activation function $LRU\left(x\right) = \begin{cases} x & x \geq 0 \\ \alpha x & x < 0 \end{cases}$. Both the bandwidth d and the number of these layers are hyperparameters, which are automatically optimized over. Finally, three output layers extract the following information from the final internal layer:

- The radial coordinate value $r_\perp\left(x\right)$
- A list of unnormalized logarithmic probabilities (*"logits"*) $l_{Z,i}$ representing confidence values for each zone assignment
- Two logits l_{open} and l_{closed} representing confidences in the associated flux surface being an open (cut by divertor or other plasma-facing components) or a closed zone

The logit values $l_{\ldots}$ can be converted into probabilities by the softmax function. We therefore get the probabilistic confidence values for the zones $p\left(Z = k\right) = \frac{\exp(l_{Z,k})}{\sum_{j=1}^{n} l_{Z,j}}$ and the probability of the magnetic surfaces being opened by a divertor $p\left(\text{open}\right) = \frac{\exp(l_{\text{open}})}{\exp(l_{\text{open}}) + \exp(l_{\text{closed}})}$. As the softmax function is monotonous, the most likely zone can be chosen as the zone with the highest l_{Z} value while a point is likely on an open field-line if $l_{\text{open}} > l_{\text{closed}}$.

3.4.2.2 Grid of training configurations

For a first experiment, the network was trained on a training set of 23 vacuum field configurations and 47 HINT equilibria3.3. The vacuum configurations were chosen from a T-shaped grid ranging from standard to high-iota, to low-iota and to high-mirror configuration. Due to availability from previous simulations, equilibrium calculations were used for standard-, low-iota- and high-iota configuration. The configuration set is parametrized by the following 10 parameters:

- Non-planar and planar coil currents (7 values)
- Toroidal plasma current
- On-axis plasma beta

- Pressure profile coefficient α, describing a profile of shape $p \propto (1-s)^{\alpha}$ over normalized toroidal flux s

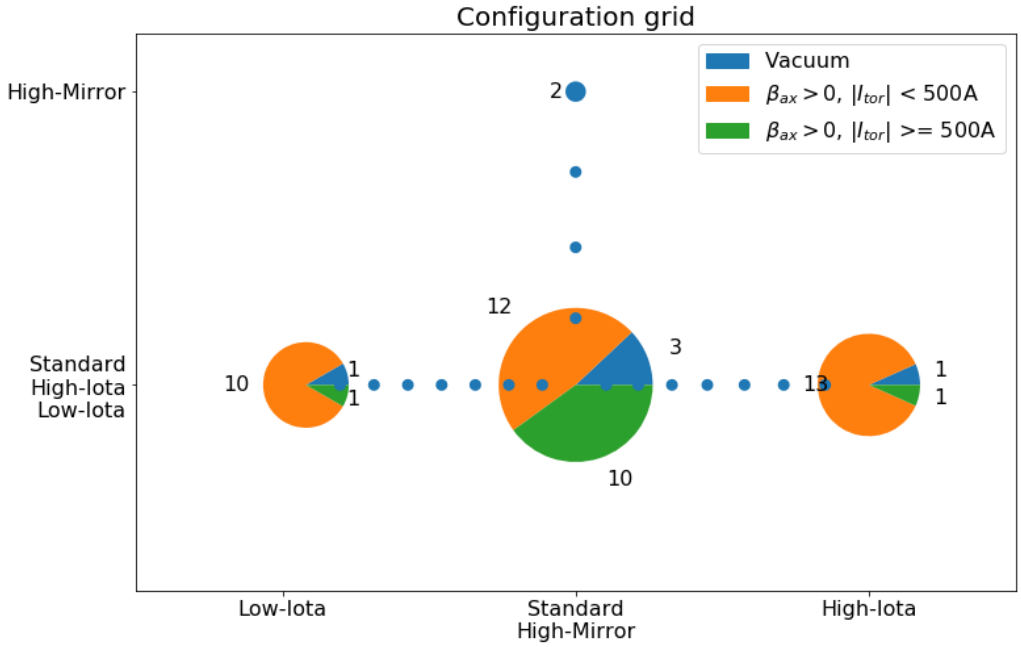

Figure 3.3: Configuration grid used for training of the flux-surface mapping network. The x-axis corresponds to the edge rotational transform, the y-axis to the magnetic mirror. The pie diagrams indicate the number of variants included for the given configuration. Blue dots correspond to a single vacuum configuration.

3.4.2.3 Choice of loss function

The loss function represents the optimization target. It is a scalar function on the input data, which is evaluated by the optimization routine. The optimizer adjusts the parameters of the model (in this case, the neural network) against the gradient of the loss function, eventually finding a local minimum. The optimization problem defined here is a *supervised learning* problem, where the model is presented with specific inputs and has to replicate a reference output. The loss function is evaluated on the data as follows:

- Select a pair of pre-computed magnetic surfaces S_1 and S_2 from the dataset, along with the pre-computed perpendicular radii $r_{\perp,\mathrm{truth}}(S_1)$ and $r_{\perp,\mathrm{truth}}(S_2)$and their real-space distance $d(S_1, S_2)$
- Sample two points p_1, p_2 from these surfaces as well as a point from the magnetic axis p_{ax}
- Apply the black-box model to these points to compute the output parameters (perpendicular radii, zone assignment probabilities and confidences of open and closed field-lines)
- Evaluate the loss function as given in equation 3.2

$$\begin{aligned} \text{Loss} &= \frac{1}{2}\left|r_{\perp,\text{estimated}}\left(p_1\right) - r_{\perp,\text{truth}}\left(p_1\right)\right|^2 + \frac{1}{2}\left|r_{\perp,\text{estimated}}\left(p_2\right) - r_{\perp,\text{truth}}\left(p_2\right)\right|^2 \\ &+ \alpha_{\text{zone}}\left[\left|d\left(S_1, S_2\right) - \left|r_{\perp,\text{truth}}\left(p_1\right) - r_{\perp,\text{truth}}\left(p_2\right)\right|\right|^2 - \epsilon^2\right] \cdot P\left(Z\left(p_1\right) = Z\left(p_2\right)\right) \\ &+ \alpha_{\text{O/C}} \cdot \left[\begin{cases} \log\left(p\left(\text{open}\right)\left(p_1\right)\right) & S_1 \text{ is open} \\ \log\left(p\left(\text{closed}\right)\left(p_1\right)\right) & S_1 \text{ is closed} \end{cases}\right] \end{aligned} \tag{3.2}$$

The first component is a quadratic regression loss. The second component is a custom loss component that encourages surface pairs satisfying equation 3.1 to be assigned to identical zones, and discourages it otherwise. The third component is a cross-entropy loss for a binary classification scheme. As the primary task of the mapping network is the reconstruction of the perpendicular radius coordinate, the second and third loss terms are multiplied by a small scale factor to reduce their impact on the outcome. This encourages the training process to prefer improving the $r_\perp$ estimator when having to make trade-offs between the different components.

3.4.2.4 Training process

The network is implemented in TensorFlow in a custom training loop. The loss function is not evaluated on a single sample from the data but averaged over sampled batches. The sampling of these batches is performed on ten configurations simultaneously. For training, 20000 samples are drawn simultaneously from each configuration and combined into one training batch. For validation, 10000 points are sampled from every configuration of the input grid. To reduce noise in the validation loss, the validation set is not resampled every time. Instead, the sample points are kept constant globally (by caching them on-disk). The network was trained using TensorFlow's [43] implementation of ADAM [44], with the learning rate being a hyperparameter. Hyperparameters were selected by Optuna's [45] Tree Parzen Estimator[46]. Unpromising runs were aborted early by an ASHA/Hyperband[47] pruner. For this pruner, Optuna's initial implementation was modified to only promote iterations to the next rung in a bracket if another run had completed this bracket already. Figure 3.4 shows an overview of the training run for the neural network, including the influence of the two most important hyperparameters, the learning rate (multiplier for all parameter adjustments by the optimizer) and the bandwidth (the number of individual neuron channels per layer).

The learning rate is the most impactful parameter for the training process. Even a slightly reduced learning rate will quickly lead to a very inefficient training process, as the incremental improvements required to optimize the network will take too long to incorporate. Conversely, if the learning rate is set too high, the updates to the network's weights will overshoot beyond the optimum, and, eventually, the training will become unstable. This instability often leads to a catastrophic numerical divergence of the weights optimization. Such events are detected and compensated by reverting both network and optimizer (as the ADAM optimizer holds internal state as well) to a checkpoint, which is saved every minute if the validation loss improves. Even with the divergence being accounted for, an overly frequent occurrence of these resets is prone to slow down the training process.

Another relevant optimization parameter is the bandwidth (and, therefore, the complexity and expressive power) of the network. On the one hand, if the bandwidth is set too low, the network will be unable to learn a sufficiently expressive internal representation of the inputs to correctly infer a

consistent set of outputs and zone partitions. On the other hand, the amount of work performed during the training process is almost proportional to the network's bandwidth. Therefore, a higher bandwidth leads to a lower number of training cycles per minute and a lower rate of training data consumption. Since training is budgeted over time and not over training cycles, the hyperparameter optimizer avoids the upper end of the bandwidth spectrum.

The upper two subfigures of figure 3.4 show the training times and final loss function values of all training attempts. The learning rate shows clear slopes towards an optimum value of $3 \cdot 10^{-3}$. The bandwidth hyperparameter also shows a cluster of high-performing runs on its lower end. However, this might also be a bias of the Tree-Parzen-Estimator, which preferentially samples new hyperparameters around previously well-performing runs. The lower left subfigure of figure3.4 indicates that the performance, while improving slightly over time, is overall a noisy property of the training runs. This points at a significant dependency on the initial weights of the network, which are sampled from a pseudo-random distribution. The bottom-right subfigure showcases the behavior of the Hyperband pruner, which stops unpromising runs after a time of six minutes, and again after a time of one hour.

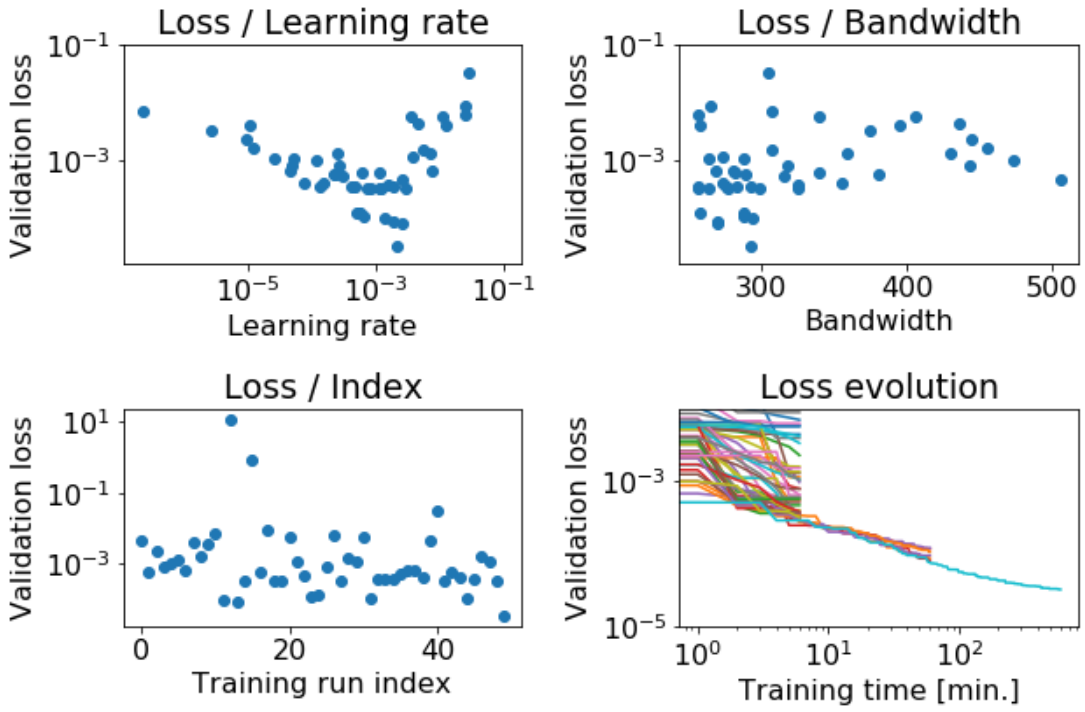

Figure 3.4: Hyperparameter dependence (upper row) and time evolution (lower row) of the training process. Dots indicate the best training loss of the run (lower is better) against run parameters and run index. Lines indicate the evolution of all training runs over time.

3.5 Summary

Numerical modeling forms the backbone of this research work. At the end of this chapter, the reader should be familiar with the equilibrium codes VMEC and HINT, and the kind of inputs

these codes need to build an equilibrium magnetic field. Furthermore, this chapter introduces the convective (parallel)-diffusive (perpendicular) field-line diffusion model, which can be used to generate strike-point distributions for test particles onto the divertor components. Finally, this chapter introduced two novel contributions to the modeling approaches, which are a full-resolution synthetic camera and a neural-network-based approach to obtain flux surface coordinates in non-nested topologies.

4 Diagnostic systems for plasma observation in magnetic confinement devices

Confinement experiments require a large number of diagnostic systems in order to characterize their plasmas reliably. They feature large numbers of non-uniformly distributed parameters, such as electron and ion temperatures and densities, parallel and perpendicular flows, turbulent fluctuations, magnetic mode excitations, impurity densities, and others, which should preferentially be observed simultaneously by multiple measurement systems each to confirm each others' measurements in a research setting. The purpose of this chapter is to introduce a subset of these diagnostic systems, which can obtain the plasma parameters relevant for these studies.

This chapter presents one original contribution, which is the reciprocating magnetic probe system embedded inside the combined probe (excluding the coil support structure, which was already designed beforehand). This contribution does not include the combined probe as a whole, but does encompass the design and calibration of the analog amplifier system and the associated post-processing, both of which are key components in its successful operation.

4.1 Thomson Scattering System

Thomson scattering is the elastic scattering of low-energy electromagnetic waves off a charged particle. Specificially, in contrast to Compton scattering, the Thomsons scattering limit assumes the velocity of the charged particle to be unaffected. If the luminosity of the scattering light source is known, the amount of photons scattered from a specific volume is directly proportional to the density of charged particles. If the light source has a narrow frequency bandwidth, the spectrum of the scattered light also contains the information required to infer the velocity distribution of the charged particles. Since lighter particles have a stronger tendency to scatter light, the dominant contributor to Thomson scattering is the electron gas portion of the plasma.

In W7-X, Thomson scattering is used to determine electron density and temperature profiles mostly in the plasma core [48, 49, 50]. In standard configuration, the beam path of the laser light source usually covers only a limited portion of the magnetic islands, as it crosses the islands near the X-point on both sides. However, the in-board side can still cover the outer 3rd of the island in standard configuration.

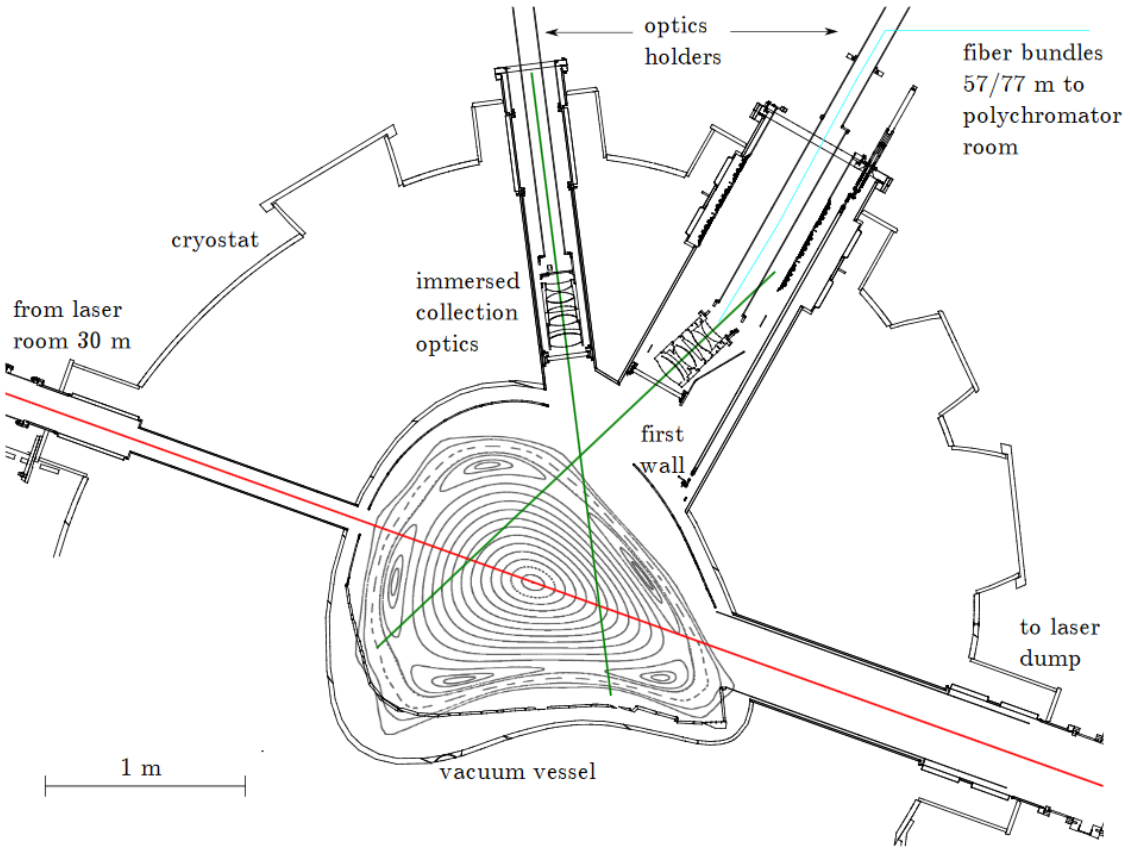

Figure 4.1: Setup of the W7-X Thomson scattering system in toroidal cross-section. [48]

4.2 X-Ray Imaging Crystal Spectrometer

The X-ray Imaging Crystal Spectrometer (XICS) is an imaging system for X-Ray radiation coming from highly charged impurities in the plasma. The centerpiece of the XICS system is a spherically bent crystal, which diffracts the in-coming X-Rays according to their (wavelength-dependent) Bragg diffraction angle. Due to its spherical bend, like a spherical mirror, such an imaging crystal has a focal length and can be used to image objects onto a detector. The X-ray detectors are oriented so that they lie in the image planes of a vertical slit aperture close to the plasma. Each point of the aperture transmits light onto the diffracting crystal from a limited region of the plasma. Since a wavelength-change of the emitted X-Ray lines lead to a change in their Bragg diffraction angles, the horizontal component of the slit's image directly depends on the wavelength spectrum of the observed line, and therefore the velocity distribution of the emitting impurity ions. The vertical component corresponds roughly to the vertical location of the emitting region (although this match is not exact since the plasma can not lie precisely in the imaging system's object plane). By inversion of the optical transmission forward model, XICS can then determine density-, flow- and temperature-profiles for the observed impurity ion species, from which it can, in turn, infer the ion temperature distribution of the background plasma.

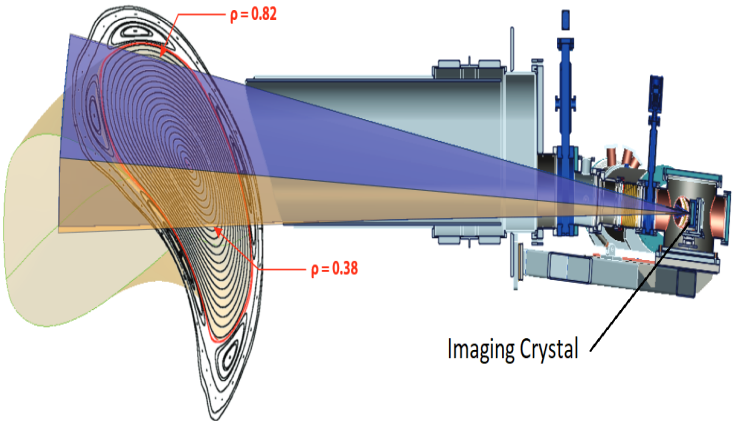

Figure 4.2: Viewing geometry of the XICS system in standard configuration. ρ indicates the normalized minor radius. Shown in red is the last closed magnetic surface. Adapted from [51]

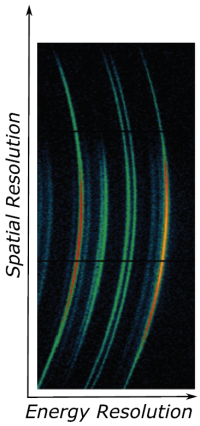

Figure 4.3: Raw XICS detector image of an Ar^{16+} emission spectrum, adapted from [52]

4.3 Helium-Beam

The Helium-Beam system [53] is a two-part diagnostic, consisting of a gas injection system embedded into the divertor plates and two viewing ports observing the injection nozzles connected to a Line-Ratio Spectroscopy system (see figure 4.4). Since the relative population of the excited electronic levels (which are excited primarily by collisions with surrounding thermal electrons) depends on both the density and temperature of surrounding electrons, the measurement of multiple line ratios allows a deduction of T_e and n_e without sensitivity to the neutral emitter density (except the signal/noise ratio of the measurement). If the neutral emitter is concentrated along a line (which is the case shortly after a gas puff), the spatial distributions of the observed lines can be used to infer linear profiles for both of these parameters.

4.4 Magnetic Equilibrium Diagnostics

W7-X features a large array of magnetic pick-up coils to measure the distribution of toroidal and poloidal currents in the plasma. Of particular interest for this research work are two of these systems:

- The diamagnetic loops are poloidally wound around the plasma domain and measure the change in integrated toroidal flux. This change in toroidal flux can then be used to reliably estimate the total thermal energy stored in the plasma via equilibrium calculations. [55, 54]

- To measure the total toroidal plasma current, W7-X currently features a total of 5 sets of Rogowski coils, all of which feature both in-vessel and out-of-vessel coils to distinguish plasma and vessel currents. Two additional sets have only their out-of-vessel components currently installed. Out of these seven coil sets, five are further segmented into eight segments, which allows measurements of the poloidal distribution of the toroidal currents.[54]

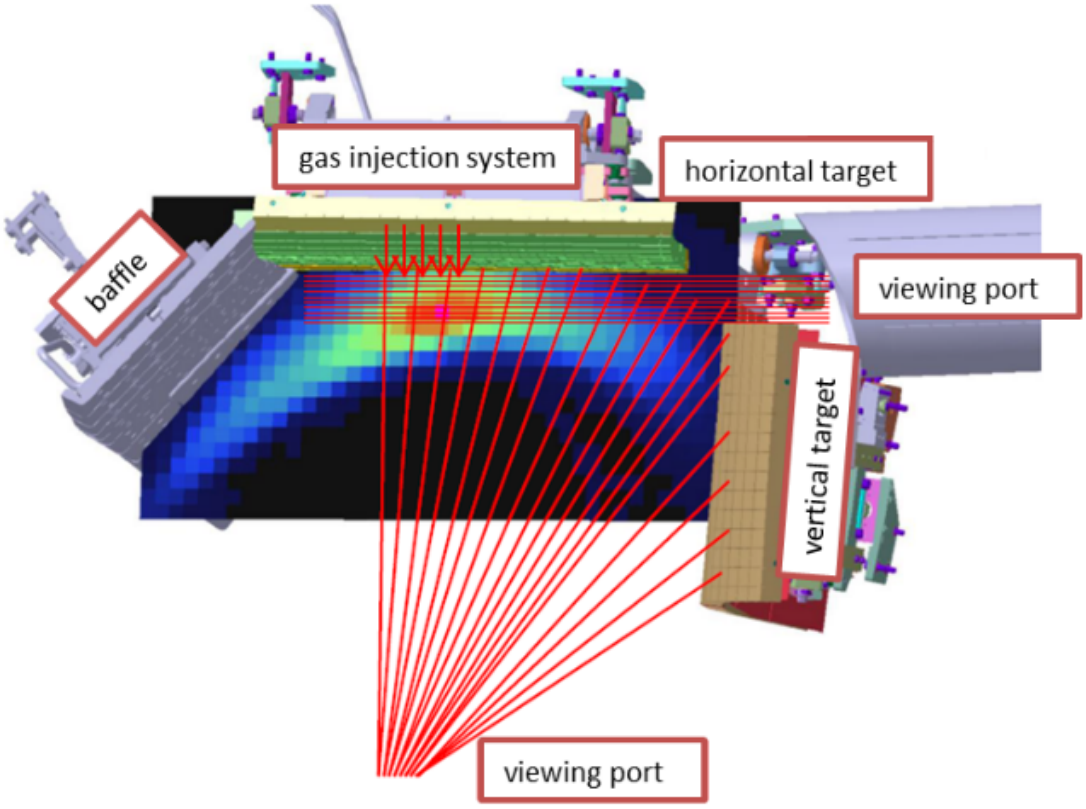

Figure 4.4: Viewing lines of the Helium-beam diagnostic, overlapped with a simulation of He-line emission[53]

- For equilibrium reconstruction, the plasma vessel is also lined with saddle coils, which can pick up low-order radial magnetic field components, which can have a strong influence on the edge islands.
- Additionally, W7-X contains multiple poloidal Mirnov coil arrays, which can pick up local magnetic field fluctuations and provide information about electromagnetic mode activity (both frequency and spatial structure of the modes).

Both of these coil systems are equipped with compensation coils to take into account the influence of external error fields during operation. Since magnetic coils only measure the time derivative of the magnetic flux passing through them, the signals have to be integrated over time. The W7-X magnetic equilibrium diagnostics rely on a digital integrator stabilized with a signal chopper in the analog signal path to eliminate long-term drifts.

4.5 Divertor IR cameras

In order to measure the heat-loads on the divertor systems, W7-X is equipped with LWIR cameras providing wide-angle (116°) observations of 9 out of its 10 divertors [56]. Each camera consists of a wide-band 1024×1024 microbolometer array, which measures the spectrally integrated power of the incoming radiation by detecting the local temperature changes on the sensor due to deposited

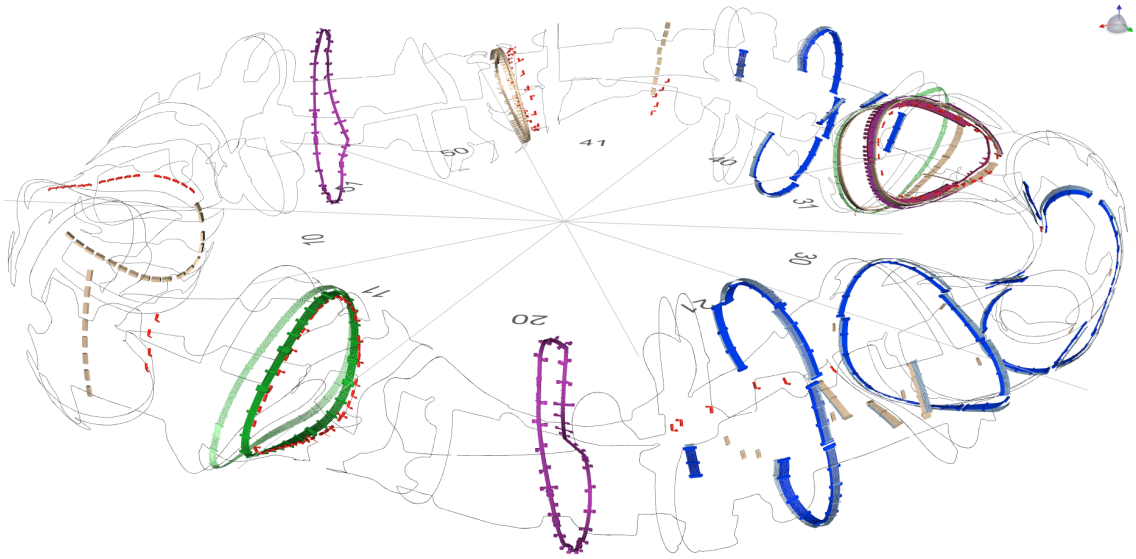

Figure 4.5: Location of the different magnetic diagnostics in Wendelstein 7-X. Numbers indicate the ten half-modules. Shown in black are saddle coils for MHD equilibrium reconstruction, in green continuous Rogowski coils (saturated inside and lighter color outside vessel), in blue the segmented Rogowski coils, in purple the diamagnetic loops and in red the Mirnov coils. Beige elements are not yet installed. [54]

power. As long as the emissivity of the divertor surfaces is known, these measurements can then be directly translated into local surface temperatures of the divertor plate. The surface temperatures are then again translated into heat-flux measurements by modeling the internal heat-diffusion in the divertor with the 2D code THEODOR [57].

4.6 Reciprocating Probes on the Multi-Purpose Manipulator

The Multi-Purpose Manipulator (MPM) [59, 60, 58] is a probe manipulator system that can quickly insert and retract diagnostic probes into/from the edge plasma. It is located in the $\phi = 200.8°, z = -17\,\text{cm}$ line and can theoretically plunge up to 35 cm inwards from its parking position. In practice, heat fluxes onto the probes limit its plunges to shallower plunges outside of the confined plasma region. Thanks to a secondary probe chamber, the probes can be exchanged during the experimental campaign without breaking the vacuum of the main vessel. This has allowed the Multi-Purpose Manipulator to be equipped with a variety of specialized probes, including multi-channel retarding field analyzers for ion plasma parameter measurements, toroidal and poloidal Mach-probe arrays for plasma flow studies, material exposition and laser-blow-off sample holders, and gas-puffing systems.

4.6.1 The combined probe

The combined probe is a diagnostic system for the integrated measurement of a multitude of plasma parameter profiles. Its front surface features a triple probe for electron temperature and density measurements, two protruding floating potential pins, a pair of up- and downstream facing Mach probes for parallel flow measurements, a gas inlet, a tungsten sample for exposition, and

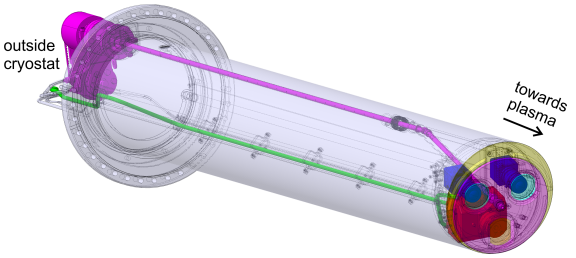

Figure 4.6: Immersion tube holding a single overview IR-camera (red) and a visible and H-alpha light camera (blue), cooled by a pressurized air cooling loop (green) and protected by a rotating shutter (magenta)[56]

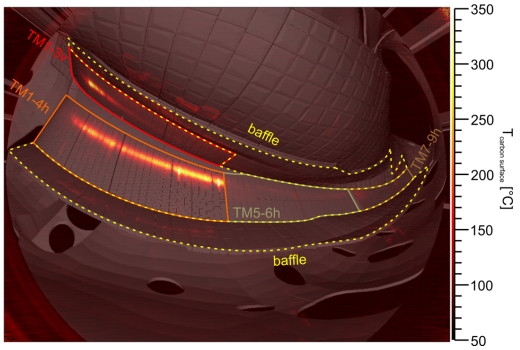

Figure 4.7: Overview of the viewing angle of the divertor IR cameras, with portions of the divertor geometry highlighted. TM1-4h, TM5-6h and TM7-9h correspond to the three sections HL, HM and HH of the horizontal divertor target, TM1-3V to the vertical target.[56]

an experimental ion-sensitive probe [62]. The probe interior - including the magnetic coils - is shielded by a Boron Nitride cover. Magnetic plasma response measurements are restricted to the outboard side of the magnetic islands due to interference between the pickup coil system and currents drawn via the Langmuir probes. This interference would manifest itself as a jump in the integrated voltage occurring simultaneously with short transient current bursts appearing on the Langmuir probe channels. To ensure that smaller variations of this interference - potentially not visible to the naked eye on the raw signals - do not accumulate in the integrated signal, the error analysis was designed to be sensitive to differences in the magnetic field measurement during the inward and outward motion.

4.6.1.1 Langmuir Probes

Langmuir probes consist of conductive pins directly inserted into the active plasma. The potential difference between the probe and its surrounding plasma creates a potential barrier, which shields a portion of the inflowing ions or electrons (depending on orientation). By simultaneously sampling multiple points of this potential-/current-curve, the Triple probe can infer the electrostatic plasma potential, electron temperatures and densities, and a constraint on the $T_i \leftrightarrow n_i$ relation (the ion saturation current).

4.6.1.2 The magnetic sensor

The magnetic probe is a 3D pickup probe consisting of three concentric mutually orthogonal coils. Each coil consists of 500 windings of a 0.1 mm copper wire with a Polyimide film (Kapton) insulation. The coils have a (calculated) effective area per winding of $1.342\,\mathrm{cm}^2$, $1.464\,\mathrm{cm}^2$ and $1.83\,\mathrm{cm}^2$ in radial, toroidal and vertical direction, respectively. The common center point is offset 39.2 mm from the front-most pin, 111 mm from the base of the probe along the probe path, and 6 mm below the MPM center axis (see figure 4.10). For measured total effective areas, see table 4.1. The design also features a differential coil pair (2198 windings each, oppositely wound, 1cm apart) for gradient fluctuation measurements, but these coils were out of operation during the

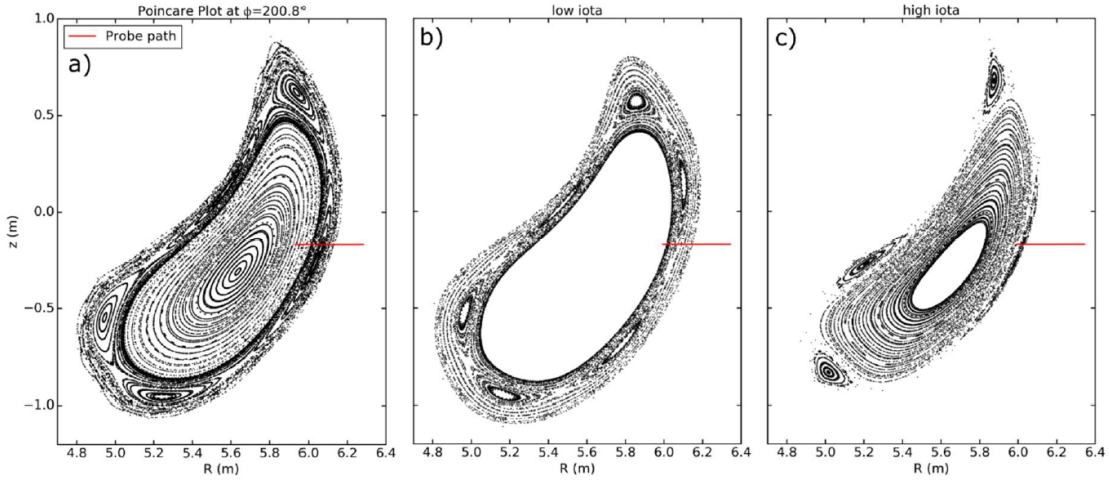

Figure 4.8: Measurement path of the MPM imposed with the magnetic field structure in standard (a), low-iota (b) and high-iota (c) configuration.[58]

2018 campaign. The pickup probe is connected via 14 m long twisted cable pairs to the integration circuit.

4.6.2 Integration circuitry for the magnetic probe

For this probe, an analog integrator was chosen over a chopper-stabilized digital integration for two reasons:

- Robustness of the integration scheme at a limited sample rate and piece-wise signal acquisition
- Availability of high-performance stock components and ease of implementation (limited time-frame between the 2017 and 2018 experimental campaigns)

To minimize distortion of the signal prior to integration (mainly by $\frac{1}{f}$ noise), the integrator was implemented as an integrating pre-amplifier. It uses a standard inverting amplifier circuit with the parameters $R_{\text{amp}} = 10\,\text{k}\Omega$ and $C_{\text{amp}} = 10\,\mu\text{F}$ (see figure 4.11). In an ideal scenario, such an integrator has an amplification factor of $\alpha = -10\,\text{s}^{-1}$. The chosen operational amplifier AD8628 suppresses common-mode drift using a built-in signal chopper and feedback loop. This configuration provides a strong noise reduction at low frequencies ($< 10\,\text{Hz}$) at the cost of additional output noise at the chopping frequency. This drawback is mitigated by pseudo-random chopping, spreading the noise up to 15 kHz wide.

4.6.3 Signal acquisition

To protect the data acquisition system from the high voltages present inside W7-X, all probe signals, including the output of the integrator, are passed through a set of DEWETRON® HSI-LV variable isolation amplifier before being recorded by a DTAQ® ACQ132CPCI and stored in an MDSplus [64, 65] tree (see fig. 4.12). Data can be acquired in a single block or over multiple segments. The isolation amplifiers have a bandwidth of 2 MHz, while the sampling rate of the

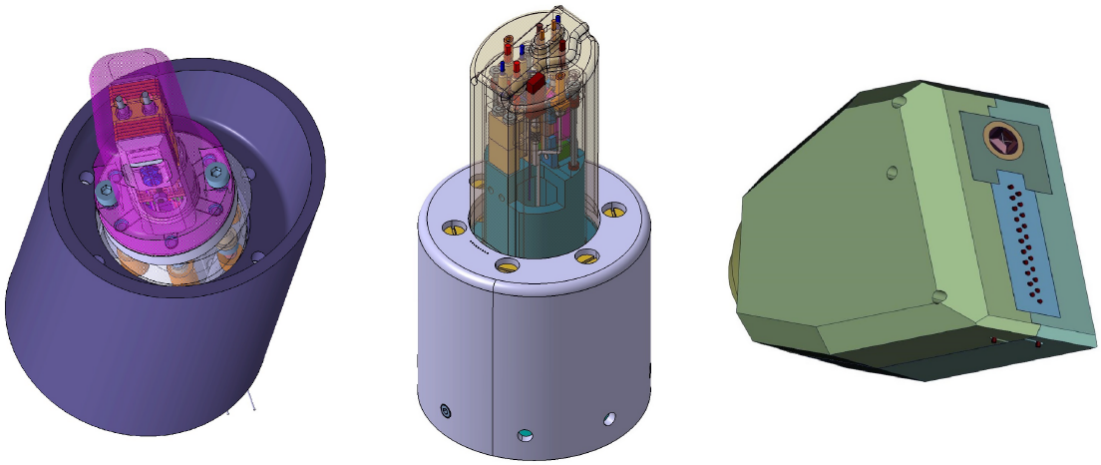

Figure 4.9: Collection of different manipulator probes, with the Retarding Field Analyzer probe FZJ-RFA1 probe (left), the combined probe FZJ-COMB2 (middle) and the poloidal fluctuation array IPP-FLUC1 (right) [61]

digitizers could be selected from a range between 250 kHz (for up to 16 s) and 2 MHz (for up to 2 s) during the last experimental campaign.

4.6.4 Characteristics of the magnetic probe

4.6.4.1 Characteristics of the pickup coils

Coil	$A_{\text{radial}}\,[\text{cm}^2]$	$A_{\text{toroidal}}\,[\text{cm}^2]$	$A_{\text{vertical}}\,[\text{cm}^2]$	$L\,[\text{mH}]$	$R\,[\Omega]$
Radial	675 ± 10	$3.9^{+5}_{-3.9}$	6.9 ± 5	3.0 ± 0.6	167 ± 10
Toroidal	$1.9^{+5}_{-1.9}$	707 ± 4	5.4 ± 5	2.7 ± 0.1	167 ± 10
Vertical	10.7 ± 5	3.0^{+5}_{-3}	888 ± 5	3.4 ± 0.1	187 ± 2

Table 4.1: Empirically obtained coil parameters[63]

Coil 1	Coil 2	Mutual inductance [µH]
Toroidal	Radial	34
Vertical	Radial	18
Toroidal	Vertical	16

Table 4.2: Upper bounds for mutual inductances of the coils[63]

The pickup coils' response curves (phase and sensitivity) were determined in a pair of Helmholtz coils. The probe was set up as it would be inside the manipulator, so the measurement also includes shielding effects from the cover and metal components. Adding capacitors parallel to the voltage measurement allowed measurement of the coil's self-inductance and internal resistance. The equivalent circuitry for this measurement is shown in figure 4.13 and can be used to obtain the frequency response (equation 4.1) to an external magnetic field (substituting $X = \widetilde{X}e^{i\omega t}$), the

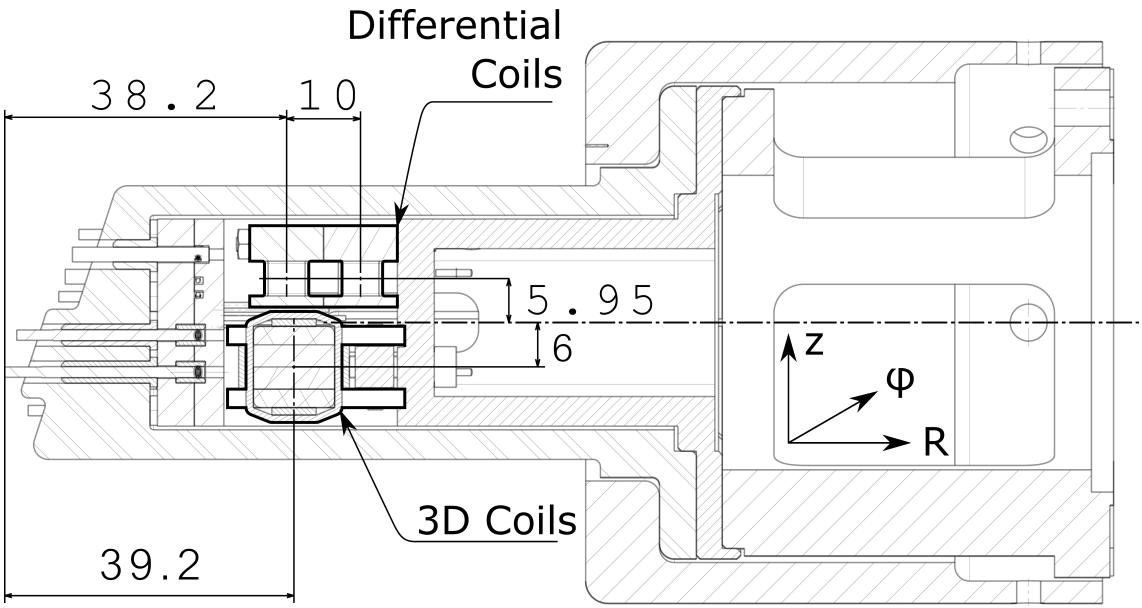

Figure 4.10: Location of the 3D and the differential coil sensors inside the combined probe[63]

derivation of which can be found in appendix A.

$$\begin{aligned} \frac{\widetilde{V}_{\text{coil}}}{\tilde{B}} =& \frac{i\omega A_{\text{coil}}}{h\left(\omega\right)} \\ h\left(\omega\right) =& 1 + \frac{R_{\text{coil}}}{R_{\text{meas}}} - \omega^2 L_{\text{coil}} C_{\text{meas}} \\ &+ i\omega\left(R_{\text{coil}} C_{\text{meas}} + \frac{L_{\text{coil}}}{R_{\text{meas}}}\right) \end{aligned} \tag{4.1}$$

The parameter C_{meas} was varied to better characterize the self-inductances, while the input impedance R_{meas} of the measurement digitizer is fixed at 1 MΩ. The parameters in table 4.1 were estimated by fitting equation 4.1 to the measurements in figure 4.14 in a range from 1 Hz to 10 kHz. In this range, the characteristics of the signal cables do not yet play a significant role. If one were doing a characterization into the MHz regime, one would have to take into account transmission delays as well as impedance matching effects. The non-monotonic relation between the effective area A and the inductance L shows that the exact winding geometry of the coil plays a vital role in determining the self-inductance. Given that the dynamic ranges have approximately a 2 : 1 : 1 ratio for toroidal, vertical and radial signals respectively, the additional error from cross-direction coupling should be bounded at about 2%, which is far below the intrinsic error level of the measurement itself (see section 4.6.4.4 for a discussion of the magnetic profile error). This limit, of course, only holds as long as the integration circuitry operates linearly, as this implies proper error cancellation when combining field measurements.

The uncertainties of the measurement in the upper-frequency region are related to two effects, which are visible in figure 4.14. Firstly, the current amplitude from the KEPCO power supply powering the Helmholtz coils drops (as the current supply is driven near its specified frequency limit of 10 kHz), reducing both the magnetic field and the coil signal. Secondly, there is an increase in background noise near 8 kHz, which causes the signal level to drop below the uncertainty. The

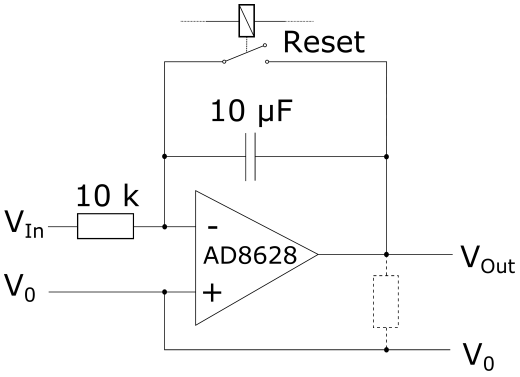

Figure 4.11: Simplified schematic of the integrating pre-amplifier (unintentional parasitic resistance displayed in dashed lines)[63]

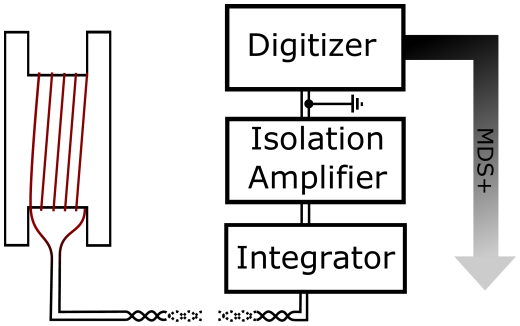

Figure 4.12: Setup of the signal processing stack for the pickup coil[63]

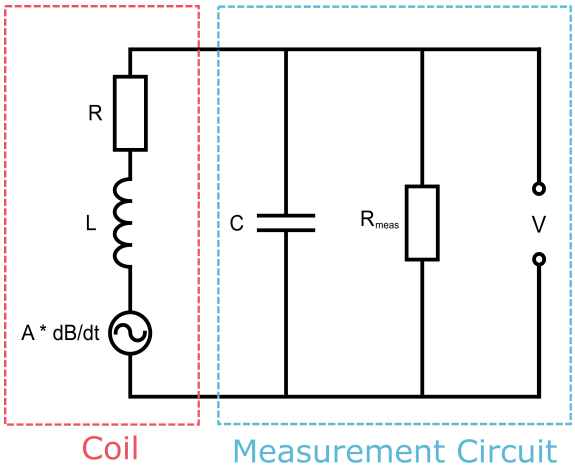

Figure 4.13: Circuitry model for the coil characterization. A, R and L are the parameters to be determined, while C is externally set and R_{meas} is a function of the voltage measurement device[63]

noise peak obtained by the background characterization (where the power supply was set to a zero control voltage) exceeds the measured signal in magnitude at a few frequencies in the coil voltage measurement. This indicates a noise reduction when the power supply is actively driven to a specific frequency, which is possible if the power supply contains a non-linear feedback loop. This means that the background measurement is likely an over-estimation of the actual measurement error, but obtaining a more accurate estimate is experimentally challenging.

By replacing the external Helmholtz coil pair with the pick-up coils themselves as the magnetic field sources, the mutual inductances of the sensors can be determined. Due to the high ohmic resistivity of the coil, only small source currents could be applied. Upper bound measurements obtained as such are shown in table 4.2. Due to the mutual inductances being two orders of magnitude below the self-inductances, and due to the comparable dynamic ranges of the signals, we assume inductive effects to be dominated by the self-inductances.

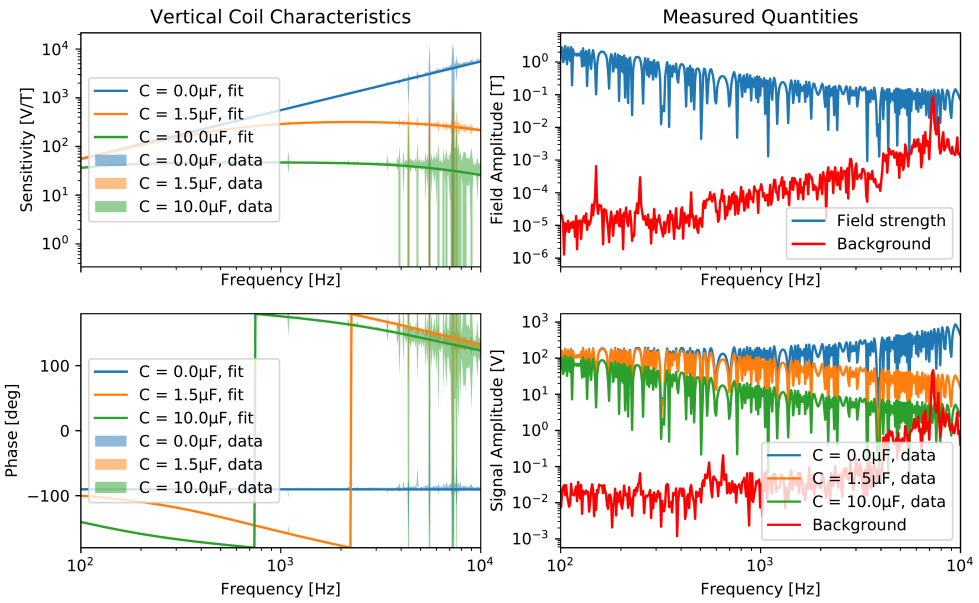

Figure 4.14: Input and output measurements - as well as background levels - for the radial sensitivity measurement[63]

4.6.4.2 Characteristics of the analog integrator

In a simple linear model, the integrator can be described using equation 4.2 with the (integrating) input amplification α and the output signal decay time τ.

$$\frac{dV_{\text{out}}}{dt} = \alpha V_{\text{coil}} - \tau^{-1} V_{\text{out}} \tag{4.2}$$

This model implies the transfer function $\widetilde{V}_{\text{out}} = \frac{\alpha}{\tau^{-1}+i\omega}\widetilde{V}_{\text{coil}}$ which has a $1/\sqrt{2}$ cutoff at $f_{1/\sqrt{2}} = \frac{1}{2\pi\tau}$. Table 4.3 shows empirical parameters for model 4.2, obtained by fitting it onto the response to a single sine-shaped pulse of 500 ms duration mimicking a typical magnetic signal during a manipulator plunge. The high decay rate τ^{-1} coincides with a $\approx 3\,\text{M}\Omega$ scale parasitic resistance, which was only present when the integrators were mounted on their auxiliary power supply board. This parasitic decay stresses the importance of proper isolation between the signal line and external circuitry and will be addressed in the next iteration of the circuitry.

Integrator	$\alpha\,[\text{s}^{-1}]$	$\tau^{-1}\,[\text{s}^{-1}]$	$f_{1/\sqrt{2}}\,[\text{Hz}]$
Radial	−11.68	0.22	0.035
Toroidal	−11.42	0.31	0.049
Vertical	−11.34	0.35	0.055
Ideal	−10	0	0

Table 4.3: Parameters for the linear integrator model described in equation 4.2[63]

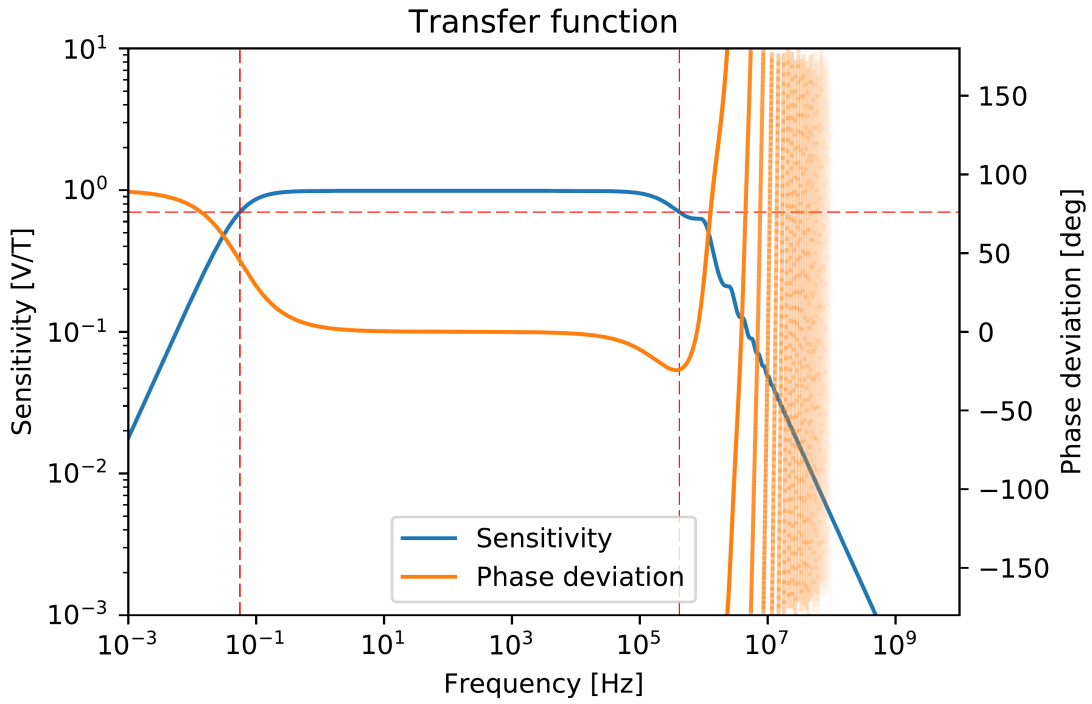

Figure 4.15: Total system characteristics of the different pickup coil systems (calculated using equation 4.3). Red lines mark the $1/\sqrt{2}$ cutoff. To improve readability the phase axis does not include the 180° from the inversion during integration.[63]

4.6.4.3 Total characteristics and post-processing

Combining the transfer function of the coil with the transfer function of the integrator leads to the total system transfer function derived in appendix A:

$$\begin{aligned}
\frac{\widetilde{V}_{\text{out}}}{\widetilde{B}} &= \frac{2i\omega A \exp(ikl)}{(1-\lambda)(1-\kappa)+(1+\kappa)(\lambda+\exp(2ikl))} \\
&\quad \cdot \frac{\alpha}{1+\frac{1}{i\omega\tau}} \\
\lambda &= Z^{-1}\left(R_{\text{coil}} + i\omega L_{\text{coil}}\right) \\
\kappa &= Z\left(R_{\text{meas}}^{-1} + i\omega C_{\text{meas}}\right) \\
Z &= \sqrt{\frac{L_{\text{cable}}}{C_{\text{cable}}} - \frac{i}{\omega}\frac{R_{\text{cable}}}{C_{\text{cable}}}} \\
k &= \sqrt{\omega^2 \frac{L_{\text{cable}} C_{\text{cable}}}{l^2} - i\omega \frac{R_{\text{cable}} C_{\text{cable}}}{l^2}}
\end{aligned} \tag{4.3}$$

with the manipulator cable resistance $R_{\text{cable}} = 2.3(1)\,\Omega$, the cable capacitance $C_{\text{cable}} = 11(1)\,\text{nF}$, its inductance $L_{\text{cable}} = 9.4(1)\,\mu\text{H}$, and the integrator's input impedance $R_{\text{meas}} = 10\,\text{k}\Omega$. The length of the cable is implicitly captured in R, C and L and does not explicitly appear in either kl, κ or λ.

As can be seen in figure 4.15, the system has good sensitivity up into the low kHz regime, which is more than sufficient for accurate integration of the magnetic field in the absence of ex-

ternal disturbance. The low-frequency behavior is, however, slightly problematic since the average measurement duration lies around 8-10 seconds. While the system is still sensitive at these frequencies, the deviations from the ideal case do already distort the magnetic field measurements in the form of a hysteresis opposite to the measured magnetic field change. Figure 4.16 b shows such a hysteresis in the form of a negative offset after the plunge.

4.6.4.4 Post-correction of low-frequency cut-off

To recover the correct field, two corrections are applied to the integrated signal:

- A linear compensation is added so that $V(t_{\text{start}}) = V(t_{\text{end}}) = 0$
- A corrected integrated voltage is defined as $V_{\text{out,corr}} = \int_{t_{\text{start}}}^{t} V_{\text{coil}}$, estimating V_{coil} using equation 4.2. The backwards application of equation 4.2 results in a correction shown in equation 4.4.

$$V_{\text{out,corr}} = \int_{t_{\text{start}}}^{t} \alpha^{-1} \left(\frac{dV_{\text{out}}}{dt} - \tau^{-1} V_{\text{out}} \right) \tag{4.4}$$

It may seem unintuitive to first put in the effort to introduce an analog integrator, only to differentiate the signal and then again apply numerical integration. However, this scheme retains the low susceptibility against intermediate drifts in the signal processing chain. Additionally, V_{out} only varies slowly between manipulator plunges (which does not apply for V_{in}) and therefore can be accurately interpolated if the signal acquisition is disabled in-between. A further advantage is that the V_{out} component can be natively sampled at a low rate, while the unintegrated signal must either be sampled at a high rate or pre-processed using an analog low-pass filter. On the downside, while this correction scheme can be used to re-adjust frequency components of the order of τ^{-1}, at even lower frequencies it exceedingly amplifies small noise components, requiring an improvement of the integrator hardware's τ value for long-pulse operation.

An example of the signal correction is shown in figure 4.16 b. Besides a 10% reduction in peak height from 0.21 T to 0.19 T due to the correction of α from -10 to about -11, the correction also significantly reduces the short-term offset of the magnetic field after the plunge and brings the time-trace more in line with the position measurement (compare figures 4.16 a and b).

As can be seen in figure 4.16 b - d, the post-corrected integrator output (also referred to as "hardware integrated" in figure 4.16 c and d) shows a significantly improved stability against low-frequency drifts, compared to both a simple software integration with a linear drift compensation (referred to as "software integrated" in figure 4.16 c and d) and the uncorrected integrator signal shown in figure 4.16 b. An unusual feature in the signal is a post-plunge oscillation at about 6 Hz that decays over about 1 s. This feature is caused by a small vertical oscillation of the manipulator's arm after the plunge, which is also visible in the arm's acceleration sensor (figure 4.16 e, see also [59]) after the plunge. The oscillation is not visible in all field components (compare figure 4.16 c and d). For profile derivation, the radial probe position is obtained using a laser-based distance measurement system. As visible in figure 4.16 a, the manipulator arm does not immediately retract to the starting position, but instead overshoots a little bit on the way back (likely due to inertia of the arm) before returning to the parking position. This overshoot is also visible in the magnetic field measurement, especially for the toroidal field profile (figure 4.16 b and c), which has a steeper

gradient at the edge.

4.7 Summary

This chapter's primary focus has been the introduction and discussion of diagnostic methods applied in this research work, introducing the Thomson Scattering system, the X-Ray Imaging Crystal Spectrometer, the Helium-Beam, the magnetic diagnostics, and last the Multi-Purpose Manipulator. Secondarily, it also discussed the design, implementation, and calibration of a magnetic probe system for the Multi-Purpose-Manipulator (and its magnetic integrator subsystem), which is an original contribution of this research project.

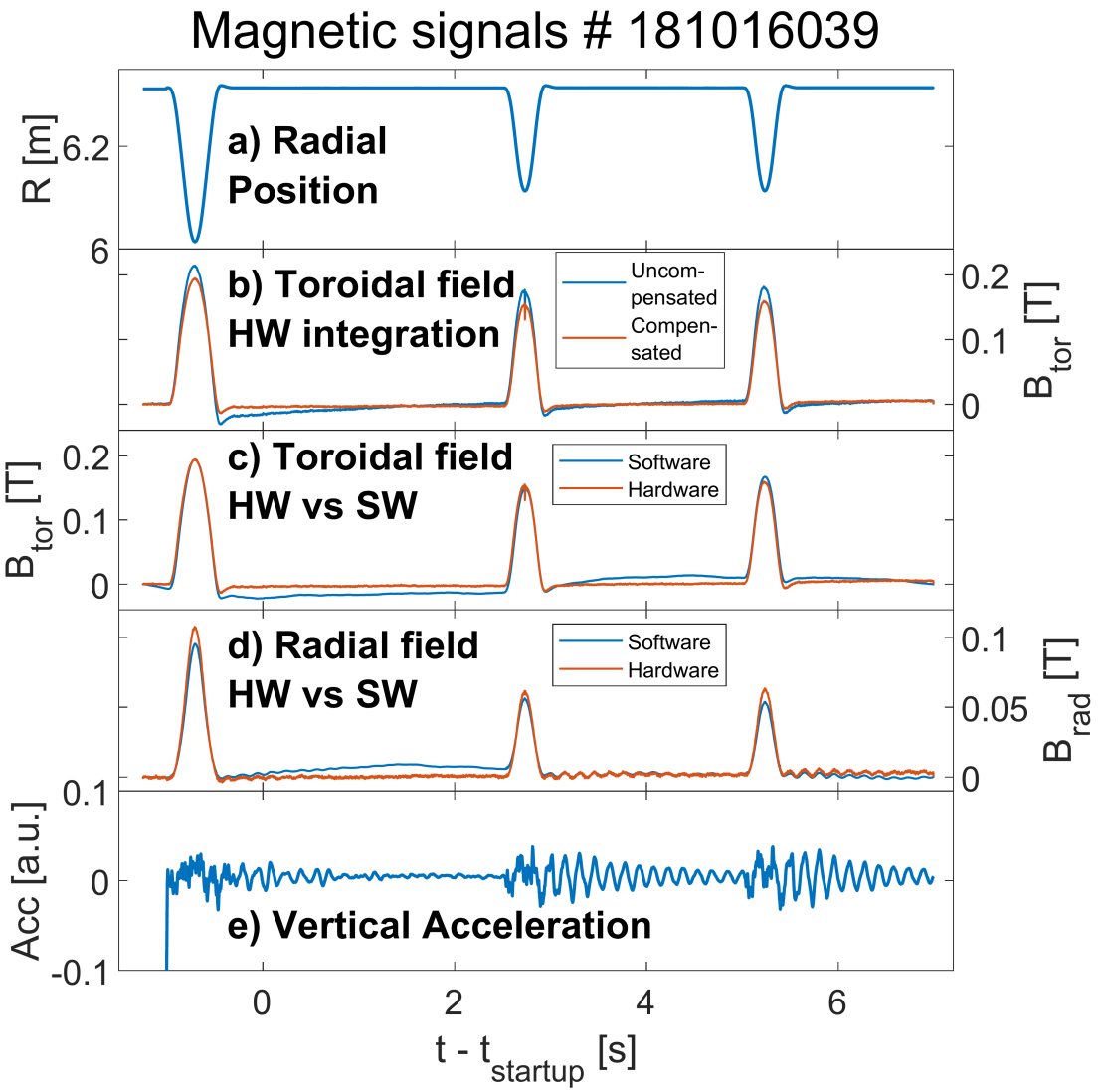

Figure 4.16: Time-traces of signals related to the magnetic probe measurement - a): Radial position of the magnetic probe, b): Comparison of hardware-integrated toroidal coil signal with and without post-compensation, c) Post-compensated hardware-integrated and software-integrated toroidal coil signal, d) Post-compensated hardware-integrated and software-integrated toroidal coil signal, e) Vertical acceleration measurement in the probe interface on the manipulator arm[63]

5 Benchmarking of predictions against experiments

While the primary goal of this thesis is to obtain predictive heat-load models for the W7-X PFCs, clarifying the limitations of the methodical approach is just as important, if not even more so, as discussing the predictions themselves. There are two stages to the predictive model, which need to be independently benchmarked:

- The equilibrium magnetic field obtained from HINT must be checked in its structure against the divertor topology of the real machine
- The limitations of the field-line diffusion model must be clarified

Both the HINT equilibria and the field-line diffusion rely on simplifications of the machine model to achieve an acceptable trade-off between accuracy and computation time. On the HINT modeling side, the machine is assumed to be five-fold symmetric. Additionally, error fields coming both from the magnetic forces flattening the non-planar coils and additional asymmetries in the machine were not parametrized in the equilibrium modeling. This is mainly due to the fact that the parameter space for these models is (without more a-priory assumptions such as stiffness models for the coils) too large to explore cost-effectively, and the present best-guess for these parameters is known to be inaccurate (improved stiffness models for the coils are on-going active research).

On the field-line diffusion side, the accuracy of the transport model is the main source of concern. Field-line diffusion models are easy to set up (compared with more involved self-consistent plasma codes such as EMC3-EIRENE), but their dominantly convective transport deviates from the usually conductive (gradient-driven) nature of plasma flow. Flow stagnation and reversal, in particular, can not be represented in field-line diffusion. Benchmarking the transport model in particular is complicated by the fact that even discharges in identical plasma conditions can show wildly different transport behavior simply due to different boundary conditions imposed by the state of the wall and the divertor. Depending on the recent discharge history, the wall can have accumulated significant amounts of impurities, which it will then release over the following discharges. Therefore, any benchmarks of heat-load models should, if possible, be performed as ensemble models over larger numbers of discharges.

Unfortunately, most experiments to date have been performed in rather moderate scenarios of $\beta_{\mathrm{axis}} \leq 2\%$ and $\beta_{\mathrm{volavg}} \leq 1\%$. This means that most beta-effects on the divertor heat-loads are comparatively weak and are buried below far greater changes in the heat-loads driven by the

evolving plasma current. The toroidal plasma current creates an additional poloidal field, and therefore increases the rotational transform ι at the edge. As the island location is defined by the location of the $\iota \in [5/4, 5/5, 5/6]$ resonances, this creates an inward shift of the magnetic island. Every analysis looking of plasma beta effects in the edge should currently, therefore, include an analysis of toroidal current effects, if only to separate the two from each other.

While simulations shown in chapter 6 present three different magnetic configurations, the standard configuration has by far the most extensive experimental coverage. Therefore, this chapter will concern itself primarily with the investigation of the standard magnetic configuration.

The results presented in this chapter are all original results in the sense that the data presented here were all collated by the author. However, credit for the individual diagnostic measurements lies with the diagnostic group of the W7-X team which operates these diagnostics. The major work lies in the combination and preparation of all these diagnostic measurements to form an integrated view which can be compared to the equilibrium simulations. This includes cross-discharge regression analysis. The only major exception is the overview plot in figure 5.1, which is provided externally.

5.1 Direct magnetic profile measurements

The most straightforward idea for benchmarking an equilibrium model is to compare the predicted magnetic field with experimental observations. This section presents an experiment in which the plasma-driven component of the magnetic field is directly measured and compared against predictions from equilibrium simulations with the HINT code.

5.1.1 Experimental setup

The experimental program shown here is part of a set of discharges designed to achieve a high core ion temperature and, potentially, an improved confinement state. The specific scenario, overviewed in figure 5.1, consists of a combination of heating through electron cyclotron resonance microwaves (ECRH) and neutral beam injection (NBI), as well as a pellet injection phase 1 s after plasma startup. The MPM was equipped with the combined probe, including the magnetic pick-up system described in section 4.6.1.2, and plunged into the scrape-off layer region three times. The first plunge was performed before the plasma startup to provide a vacuum reference. The last two plunges were shallower plunges during plasma operation, which measured the equilibrium magnetic field's radial profile. The chosen program was selected due to its good data quality in the magnetic probe signal (which was the primary motivation for the shallow plunges) and its low toroidal plasma current.

5.1.2 Magnetic probe measurements

Figure 5.2 shows radial profiles of all three magnetic field components, as well as theoretical field profile calculations obtained by applying the Biot-Savart law to the ideal CAD coil geometry. The radial profiles were obtained by binning the magnetic field time trace radially over the position signal, using the mean and standard deviation of the bin ensembles as, respectively, value and error estimates. This ensures that any differences in the measured magnetic field between the inward and outward movement of the manipulator are appropriately captured in the error bars. To remove the influence of high-frequency MHD events, the magnetic signal was low-pass filtered

before binning. The cutoff frequency was varied between 50 Hz and 500 Hz without any significant variation of the profile or its error estimates. Toroidal current measurements were obtained from the W7-X Rogowski coil system, and the peak plasma beta was estimated from Thomson scattering measurements for electron-density and -temperature measurements assuming $n_I = n_e$ for the ion density and $T_i = \min(T_e, 1.5\,\mathrm{keV})$ for the ion temperature. Because the profiles are obtained by integration, they are only defined up to a constant. This constant is chosen so that the integrated signal is 0 T at the start of the measurement (which is before the $t = 0\,\mathrm{s}$ time of plasma startup). The measured profiles do not agree perfectly with the expected profiles from a Biot-Savart calculation assuming an ideal coil configuration. The first visible disagreement is a small positive offset from zero at the outer-most radius (which is the start- and end-point of the plunge) in all components. This is probably a small low-frequency drift that could not be fully corrected during post-processing. The additional slope disagreements in vertical and toroidal direction could be error fields related to the flattening of the main coils generating the magnetic field[66]. All of these deviations are not limited to this discharge but can be observed systematically during the whole day in standard magnetic configuration.

Since the first probe plunge was always performed before the plasma startup, it can be used as an experimental vacuum reference for plasma response calculation. Error analysis estimates that the magnetic probe has a field resolution of about 4 mT in vertical and radial, and about 10 mT in toroidal direction (the difference is likely due to the stronger overall magnetic field change in toroidal direction). The radial magnetic field measurement, in particular, is accurate enough to detect a significant (given the measurement uncertainties) deviation between the vacuum magnetic field and the magnetic field during the discharge. When comparing the measured magnetic field change to the magnetic field generated by a hypothetical current filament of 1 kA on the magnetic axis, it can be seen, that an on-axis current of about $-4\,\mathrm{kA}$ (far more than present during the discharge) would be required to even poorly match the change in edge magnetic field. Therefore, the magnetic field changes observed are likely not driven by a parallel bootstrap current (which is usually strongest in the core), but are instead probably related to diamagnetic and Pfirsch-Schlüter currents.

Figure 5.3 shows a more in-depth comparison of the measured radial magnetic field profiles with various different HINT equilibria. To achieve a better match between experiment and modelling, both the HINT equilibria and the probe measurements were linearly combined. First, the probe measurements were combined as $\Delta B = \frac{I_2 \Delta B_1 - I_1 \Delta B_2}{I_2 - I_1}$, which would cancel the toroidal current contribution at first order. Then, the HINT equilibria of $\beta_{\mathrm{ax}} = 1\%$ and $\beta_{\mathrm{ax}} = 2\%$ were interpolated to match the $\beta_{\mathrm{ax}} = 1.2\%$ of the interpolated experimental discharges. Unfortunately, the probe could not plunge deep enough to measure the rollover point of the radial field change. As visible in the lower part of figure 5.3, a measurement of the rollover point's location would provide a direct indicator of the pressure profile shape.

5.2 Integrated observation of pressure profiles and comparisons to HINT

A second intrinsic physical quantity of equilibrium calculations is the pressure distribution obtained in the equilibrium configuration. While the consistency of the pressure profile with its magnetic field is enforced by the equilibrium codes, the radial profile is a high-dimensional input which the codes attempt to match. All analyses done in this thesis focus on a two-dimensional pressure profile space, which aims to capture the central pressure as well as the stored kinetic energy (the integrated pressure), but does not capture effects related to the detailed shape of the profile. It would, therefore, be interesting to see how well the equilibrium simulations match the profile shape. Another question is the behavior of the field-line averaging process in the edge, which is a very simple approximation of edge transport physics. While pressures are small in the edge compared to the core, the impact of small localized gradients in the edge is an open question. A comparison between the assumptions in the equilibria and the measurement observations serves is useful in steering present and future research on this matter. A related issue of particular importance in the edge is the probable disagreement between up- and downstream measurements of plasma parameters. It must be clarified where diagnostics agree enough with each other to rely on geometric information for interpolation between experimental data, and where additional input from more expensive plasma transport simulations is required.

To achieve the goals outlined above, this section combines the observations provided by four diagnostics into a consistent view. Electron temperature and density measurements are sourced from Thomson scattering, the He-Beam, and reciprocating manipulator probes, while ion temperature measurements are provided by XICS. To inspect the potential mutual agreement of the plasma parameter measurements along magnetic surfaces, the neural network presented in section 3.4 was employed to map all diagnostics into the surface-aligned $r_\perp$ coordinate. The sight-lines of the electron-related diagnostics are shown in figure 5.4, together with the resulting coordinate mapping of their sight-line. XICS measures line-integrated emissions and relies on a VMEC coordinate system for its tomographic inversion. The sight-line of the Thomson scattering system was used to bridge the VMEC coordinate into the coordinate space used here.

Figure 5.5 shows a combined view of electron-temperature and -density by Thomson Scattering, the Helium-Beam and the MPM, as well as ion temperature measurements by XICS. In the plasma edge, all three diagnostics agree on the electron temperature where they observe identical magnetic surfaces. Both the MPM and the He-Beam also observe a hollow structure in the electron temperature in the island, with the electron temperature first falling and then rising again as the surface label moves from the separatrix to the island O-point. In the plasma core, both sides of the Thomson scattering side-line agree well on the electron temperature profile. However, in the deep core ($r_\perp < 3\,\mathrm{cm}$), the profiles are not fully self-consistent. The density profiles are substantially more challenging to interpret, as most observations disagree with each other. There are, however, two statements that can be clearly made. The first one is the observation that the MPM and the Thomson-Scattering measurements appear to connect reasonably well. The second clear observation is that the He-Beam consistently measures higher electron density values than the MPM. This could be related to the fact that the He-Beam measures directly above the divertor target, which is itself a particle source. It should also be mentioned that the XICS measurements presented here

were inverted using a vacuum VMEC surface description. The shape of these surfaces does not match the finite-beta surface labels provided by the mapping network, which results in a profile hysteresis in the edge.

When combining the XICS and Thomson-measurements, the resulting total pressure profile shows a double-hump structure. This structure is not reflected in the HINT equilibria, which suggests that future HINT investigations into the standard configuration should potentially expand the pressure profile domain beyond the two-degrees-of-freedom-approach currently employed. In the plasma edge, the current setup of the HINT runs does also not allow the code to build up a significant pressure in the scrape-off layer, with the pressure distribution quickly falling even below the electron pressures observed by the edge diagnostics. This could, in the future, be remedied by modification of the pressure profile at the edge, but has to be likely accompanied by a further decrease of the pressure-averaging length and potentially an increase in grid resolution to better resolve the divertor structure.

5.3 Beta-effects on divertor heat-loads

Beyond consistency checks on the calculated equilibria, it is also of interest to compare the predicted divertor heat-loads against measurements from divertor IR cameras. The primary motivation for this is the desire to accurately tune the field-line diffusion model to provide the best match to experimental measurements. Figure 5.6 shows an overview of divertor heat-flux measurements by divertor infrared (IR) cameras and a field-line diffusion result in a similar equilibrium. Overall, the main strike-line (left portion) shows a decent agreement between experimental observation and the synthetic camera. The heat-loads on the vertical target also show a similar qualitative structure in simulation and experiment. However, there is a hot region in the horizontal divertor's high-iota tail which is not predicted by the model. This is most likely a short-coming of the field-line diffusion part of the model, which does not permit particles to change their toroidal velocity once launched. Specifically, particles are prohibited from performing U-turns. Effects of parallel flow stagnation and bi-directional diffusion are therefore poorly captured. Transport codes including parallel diffusion models, such as the plasma transport simulation code EMC3-EIRENE, should be able to reproduce this experimental feature if this was indeed the cause. Furthermore, the strike-line width exhibits a deviation between the upper and lower divertors, with the upper divertors (viewed from port AEF31 as an example in figure 5.6) showing generally wider strike-line patterns than the lower divertors (example being viewed from port AEF30 in figure 5.6).

What can also be seen, however, is an asymmetry between the upper and lower divertors in the experimental observations. Such asymmetries can not be reproduced by the theoretical modeling process applied here. The HINT equilibrium calculation assumes a high degree of symmetry (five-fold stellarator symmetry) for both the magnetic field and the machine geometry. In the experiment, low order magnetic error fields are almost universally present in any magnetic configuration. The lowest order perturbations are usually:

- The machine and its magnetic axis are not perfectly aligned. Mismatches in the horizontal plane result in a $^{n}/_{m} = {}^{1}/_{1}$ radial error field along the flux surfaces, while a vertical mismatch results in a $^{n}/_{m} = {}^{0}/_{1}$ error field (vertical shift).

- While most of W7-X is built out of non-magnetic metal, diamagnetic effects are still present

in many materials. These responses create tiny error fields. For components which are present in all plasmas, these will be $^{n}/_{m} = {}^{5}/_{1}$ error fields. For unique components, these perturbations will generate small $^{1}/_{1}$ error fields

The vertical shift, together with the fact that the upper and lower divertor support structures are differently loaded (pushing vs. pulling load), usually results in up-down asymmetries of the divertor heat-loads. The effects of magnetic error fields are usually dominated by the lowest-order modes resonant with the relevant flux-surfaces. As the standard configuration has a rotational transform of $\iota = 1$ at the edge, the edge field is most sensitive to the $^{1}/_{1}$ and $^{2}/_{2}$error fields. Like-wise, the induced changes in the strike-line should only be a function with the helical angle $\zeta = n \cdot \phi - m \cdot \theta = \phi - \theta$.

As figure 5.8 shows, this picture is apparently incomplete. Fitting an $^{0}/_{1} + {}^{1}/_{1} + {}^{2}/_{2}$ model onto strike-line positions averaged over a larger dataset (see section 5.3.1 for an overview of the experimental data), while containing significant asymmetries of all three kinds, also leaves a significant variance between the observation ports which can not be attributed to either. Unfortunately, since only 9 divertor modules are available for observation most of the time, a more descriptive model can not be fitted without risking significant overfitting.

5.3.1 An experimental and a synthetic dataset

In order to properly benchmark the simulated divertor heat-loads, I selected an ensemble of experimental discharges and created a large number of equilibria to cover the same parameter space. For the dataset, I chose the discharges of August 14th 2018 and discarded all discharges with a modified vacuum magnetic configuration. The particular experiment day was chosen for the following reasons:

- A single day was used to avoid effects from day-to-day switching, such as wall condition changes
- The whole day was run in standard configuration
- The discharge ensemble includes a large number of "reference" discharges with many repetitions, designed to provide stable environments for plasma characterization

The discharges were then sliced in 1 s intervals. Observations were (after extraction of the strike-line parameters) averaged over upper and lower divertor observations of 4 out of 5 modules (excluding module 5) and then aggressively cut to ensure good contrast in the divertor heat-flux reconstructions in all used cameras. For modeling comparison, the same data processing was applied to synthetic heat-flux distributions obtained with field-line diffusion. Equivalents of the experimental parameters were extracted from the equilibrium calculations. The parameters going into the comparison are described fully in table 5.1.

In the end, the benchmarking model holds 15 full-field equilibria and corresponding field-line diffusion runs. Projections of the grid onto colored 2D plots (figure 5.9) show that these 15 equilibria are sufficient to achieve a good coverage of the experimental parameter distributions.

Parameter	Observation	Synthesis
Normalized heat-flux distribution	Heat-fluxes reconstructed from, that the HINT equilibria IR camera observations, normalized against P_{ECRH} (heating power) - P_{rad} (radiated power, measured by bolometer cameras)	Obtained using field-line diffusion and virtual heat-flux camera
Pressure profile (including on-axis beta and peaking factor)	Electron density and temperature observed by Thomson Scattering, Ion temperature observed by X-Ray Imaging Crystal Spectrometer (XICS), Restricted by two-parameter fit $(p = p_0 \cdot (1-s)^{\alpha})$	Specified as input to the HINT code
Plasma stored energy	Measured by change in toroidal flux by the diamagnetic loop	Calculated by integrating the 3D pressure distribution
Toroidal plasma current	Total current measured by Rogowski coils, profile unknown	Total current specified as input to HINT, peaked current profile assumed $(j \propto (1-s)^2)$
Radiative power fraction $P_{\mathrm{rad}}/P_{\mathrm{ECRH}}$	P_{ECRH} measured by control system, P_{rad} measured by bolometer cameras	Assumed as 0

Table 5.1: Physical parameters shared between synthetic and experimental device and method of observation and synthesis

5.3.2 Evolution of the strike-line position

As a target for quantitative comparison of the model and experimental measurements, the distance of the strike-line from the pumping gap along the blue line shown in figure 5.6 was chosen. The evolution of the strike-line position is mostly robust against changes in edge transport and therefore provides a reliable accuracy measurement for the calculated equilibria. The change in strike-line position was then approximated by a linear regression in central beta, peaking factor, and toroidal plasma current. Errors on the linear fit parameters were estimated by repeatedly performing the same fit on subsamples of the dataset to obtain distributions of the fit parameters. Figure 5.10 shows a comparison of the predictions for strike-lien distances based on the linear estimation against the data points in the dataset. The dataset appears to scatter beyond the uncertainty of the regression. This does not mean that the error bar on the fitted parameters is underestimated but rather indicates the presence of nonlinearities and/or statistical fluctuations in the input data. The full datasets and the regression results are shown in figure 5.11. Both theory and experiment do not showcase any significant shift of the strike-line over the dataset range, with the strike-line shifting about 3 mm over the 1% to 2% range of central beta in the theoretical modeling and no statistically significant shift with central beta being visible in the experimental data. However, the small difference between the modeled and measured trends appears to be statistically significant. Theory and experiment also both predict a 2.5 mm shift in the strike-line position due to pressure profile shape changes at fixed central beta. The main driver for strike-line position changes in both datasets is the toroidal plasma current, which can shift the strike-line by 2 cm when evolving in a range up to 5 kA. Finally, the model appears to underestimate the distance between the strike-line center and the pumping gap by 6 mm to 1 cm. This offset is also present in low-beta current-effect studies [28] and extends all the way down to the vacuum field. Therefore, it is most likely an effect

of the field-line diffusion model and requires significantly more detailed and resource-intensive numerical modeling (e.g., EMC3-EIRENE) to overcome.

5.4 Summary

The comparison with low-beta experiments seems to indicate the limitations of the employed field-line diffusion model clearly. On the positive side, the field-line diffusion correctly predicts the strike-pattern evolution on the divertor, both the absolute location of the main strike-line and the relative heat-load distribution between different sections of the horizontal target plate. However, a primary limitation of this model seems to be its single-directional flow approximation. The relaxation of this assumption would be a worth-while investigation point in the near future. Concerning the behavior of the HINT equilibria, the results appear to compare favorably with the experimental results. The reduced parameter space used for the equilibrium calculations seems to decently capture the behaviors in central beta and the peaking factor, and the code's predictions seem to match the experimental measurements in their (albeit considerable) confidence intervals.

The magnetic field plasma response measurement especially still suffers from a somewhat poor signal-to-noise ratio, which is expected to improve in the next operational campaign through hardware improvements and overall higher plasma beta (as well as longer discharges, which potentially provide more measurement opportunities in steady conditions). The coming experimental campaign will also provide a more series testing ground for the equilibrium predictions, as many changes outlined in chapter 6 will only then start to become apparent.

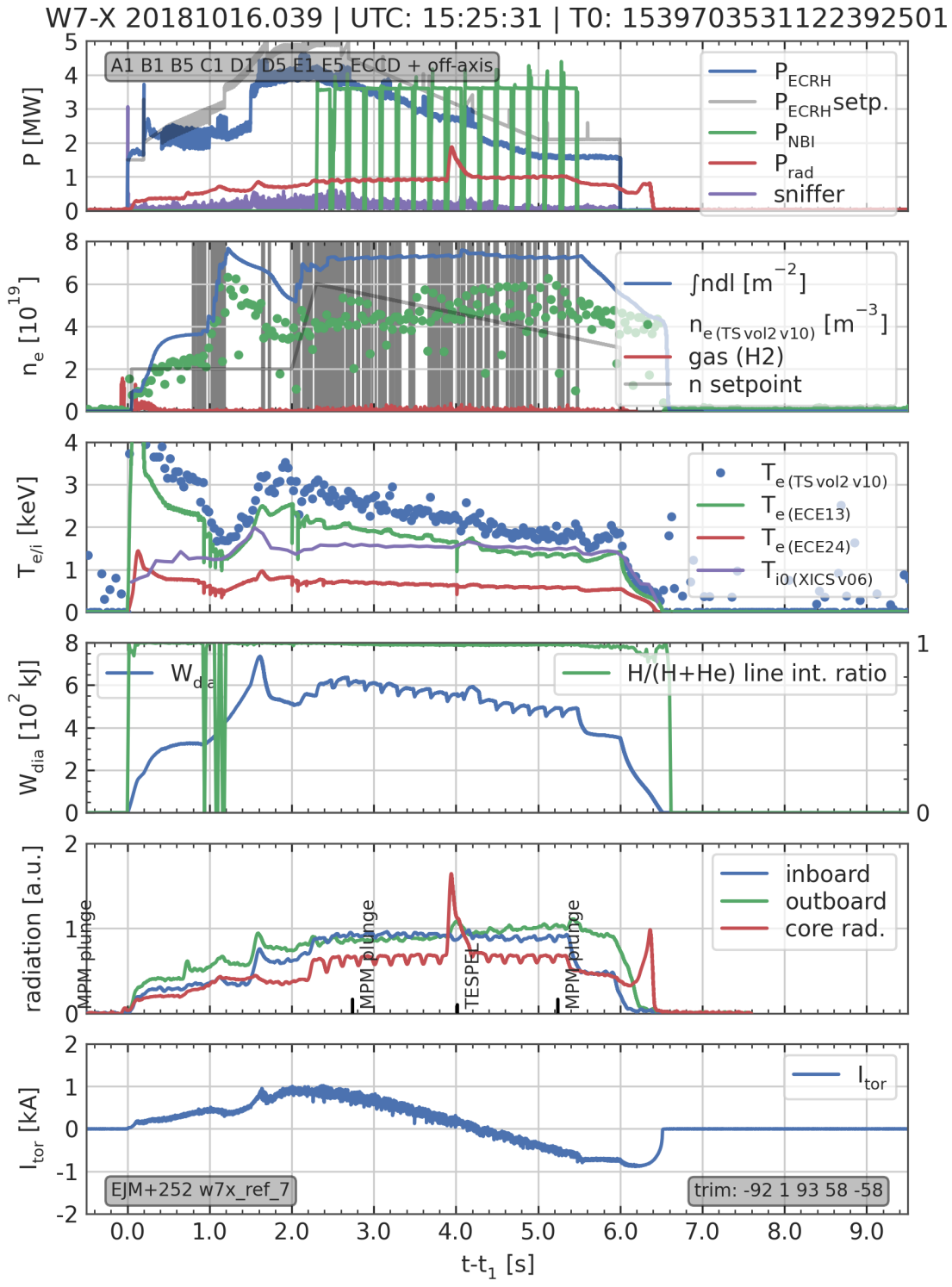

Figure 5.1: Overview of experimental program. Shown are power balance (ECRH and NBI heating, radiative power loss, sniffer interlock for ECRH shinethrough - top), particle balance (integrated electron density from interferometer, peak Thomson Scattering electron density, and fuelling rate - 2nd row), temperatures (electron temperatures from Thomson Scattering and ECE, ion temperatures from XICS, 3rd row), plasma energy (stored energy, 4th row), radiation measured by Bolometer cameras (including times MPM plunge and injection of TRacer Encapsulated Solied PELlet, 5th row), and toroidal plasma current (annotated with vacuum configuration, VMEC reference equilibrium and trim coil currents, bottom row). Figure provided by Adrian von Stechow.

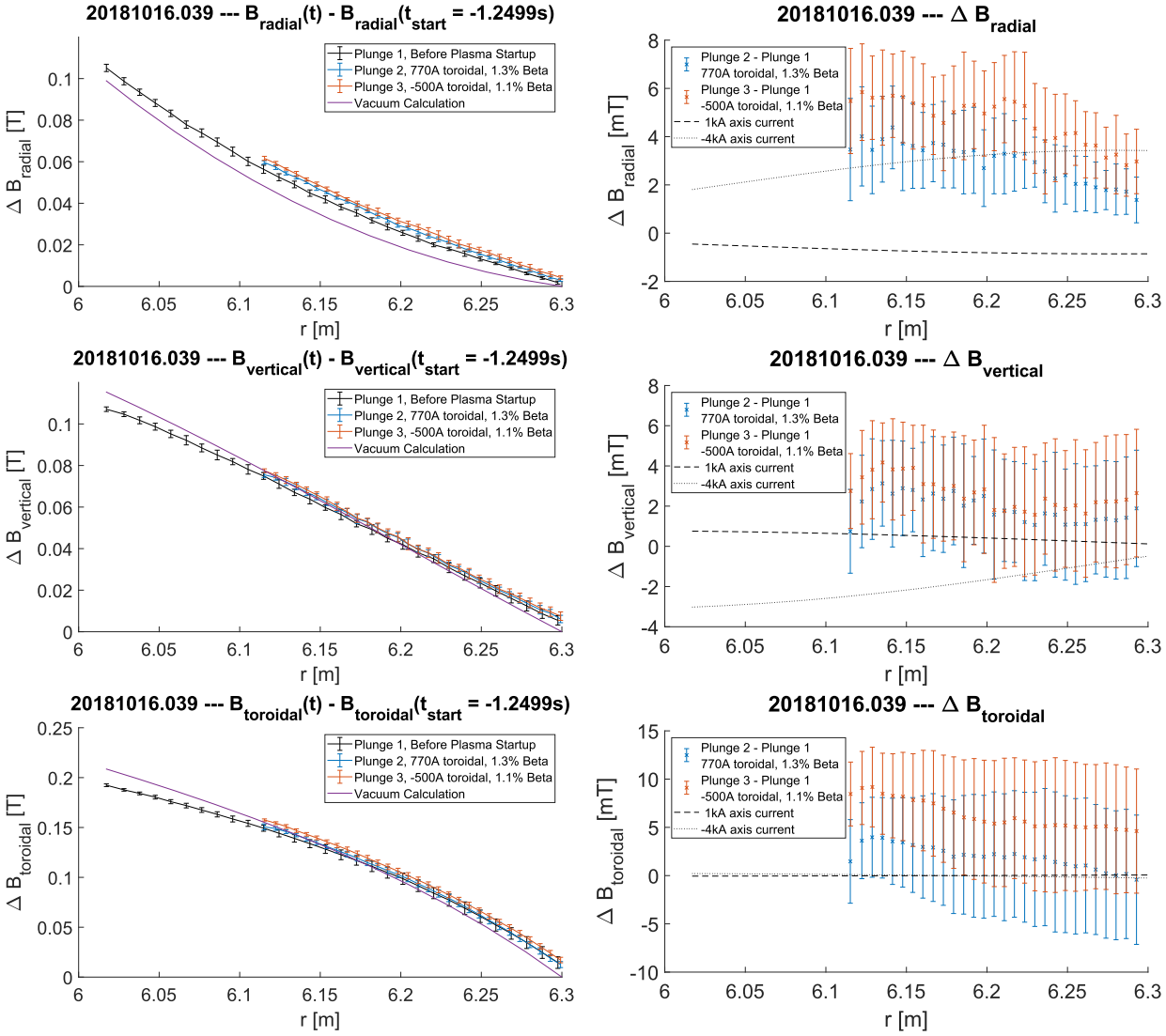

Figure 5.2: Measurements of magnetic field profiles (left) and plasma response (right). Plasma response is calculated as the difference between in-plasma and vacuum magnetic profiles.[63]

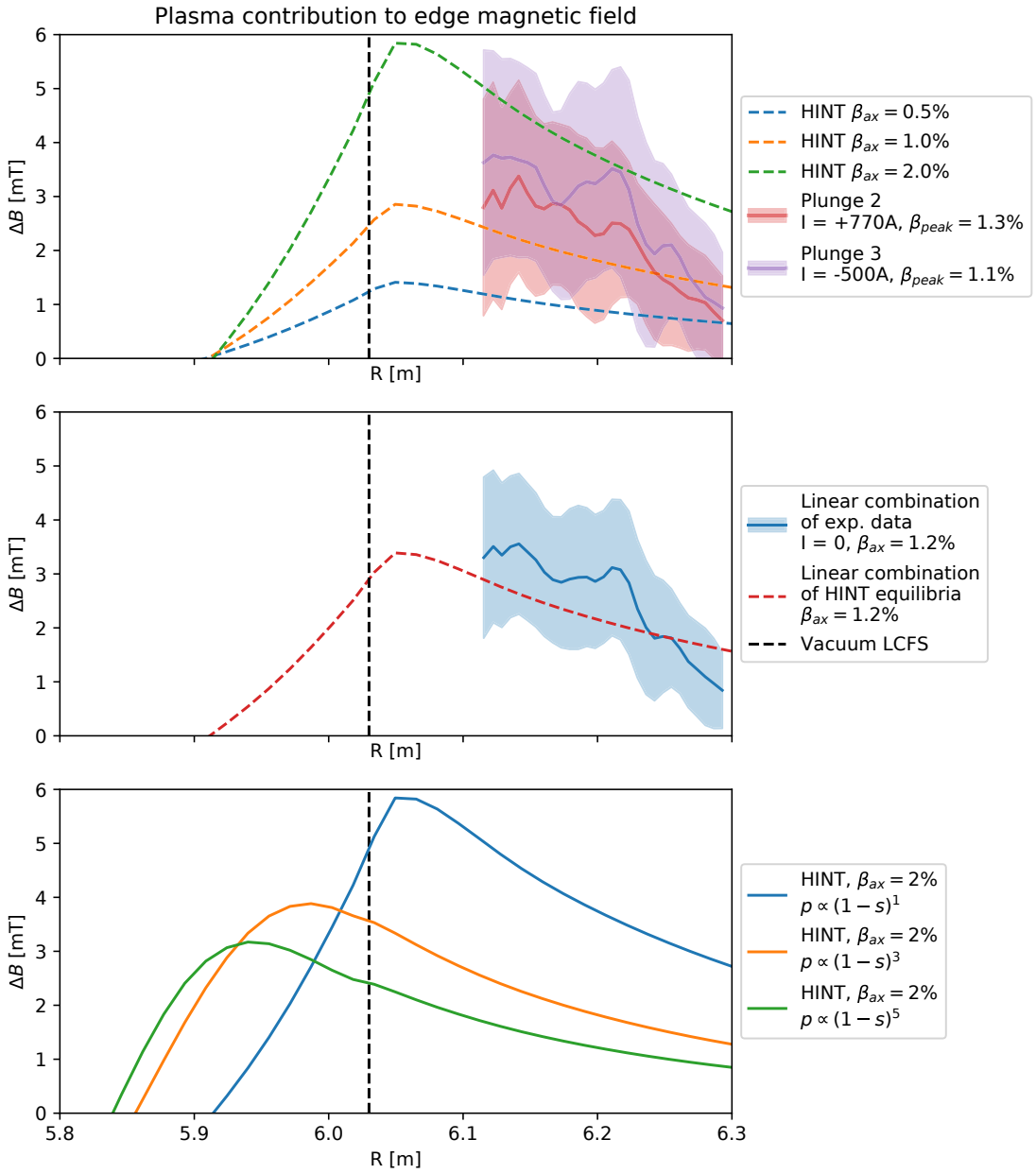

Figure 5.3: Comparison of magnetic probe measurements and HINT calculations for changes in the radial field. Shown are both measurements as well as HINT equilibria ($p \propto 1 - s$) with similar range of central beta (top), linear combinations of measurements and HINT equilibria (middle) and radial magnetic field change predictions for different pressure profile shapes (bottom).

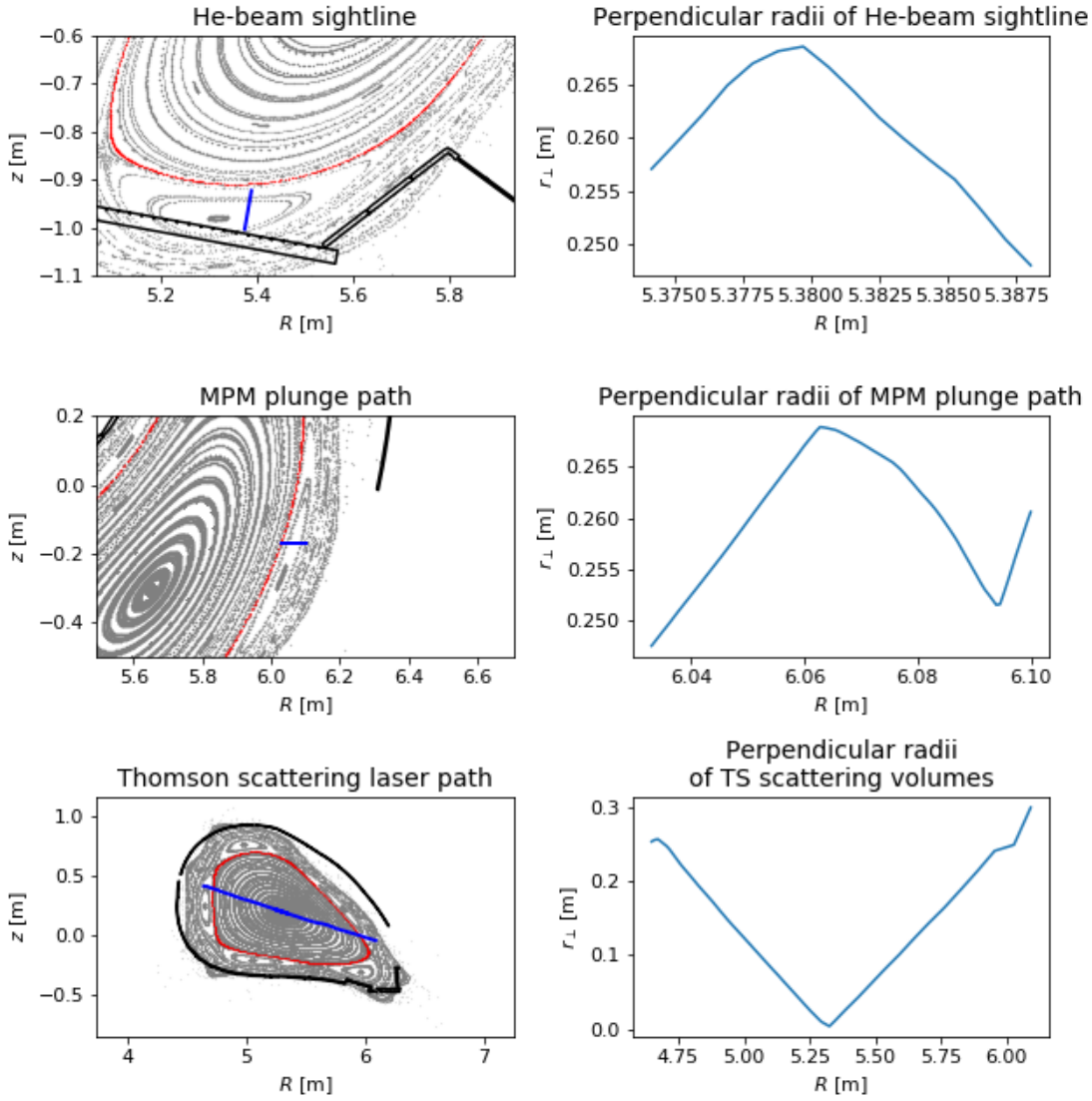

Figure 5.4: Profile / Sight lines of the He-beam, Thomson scattering and the MPM. All sight-lines (including the He-Beam line, which is almost vertical) are sliced against their major radius.

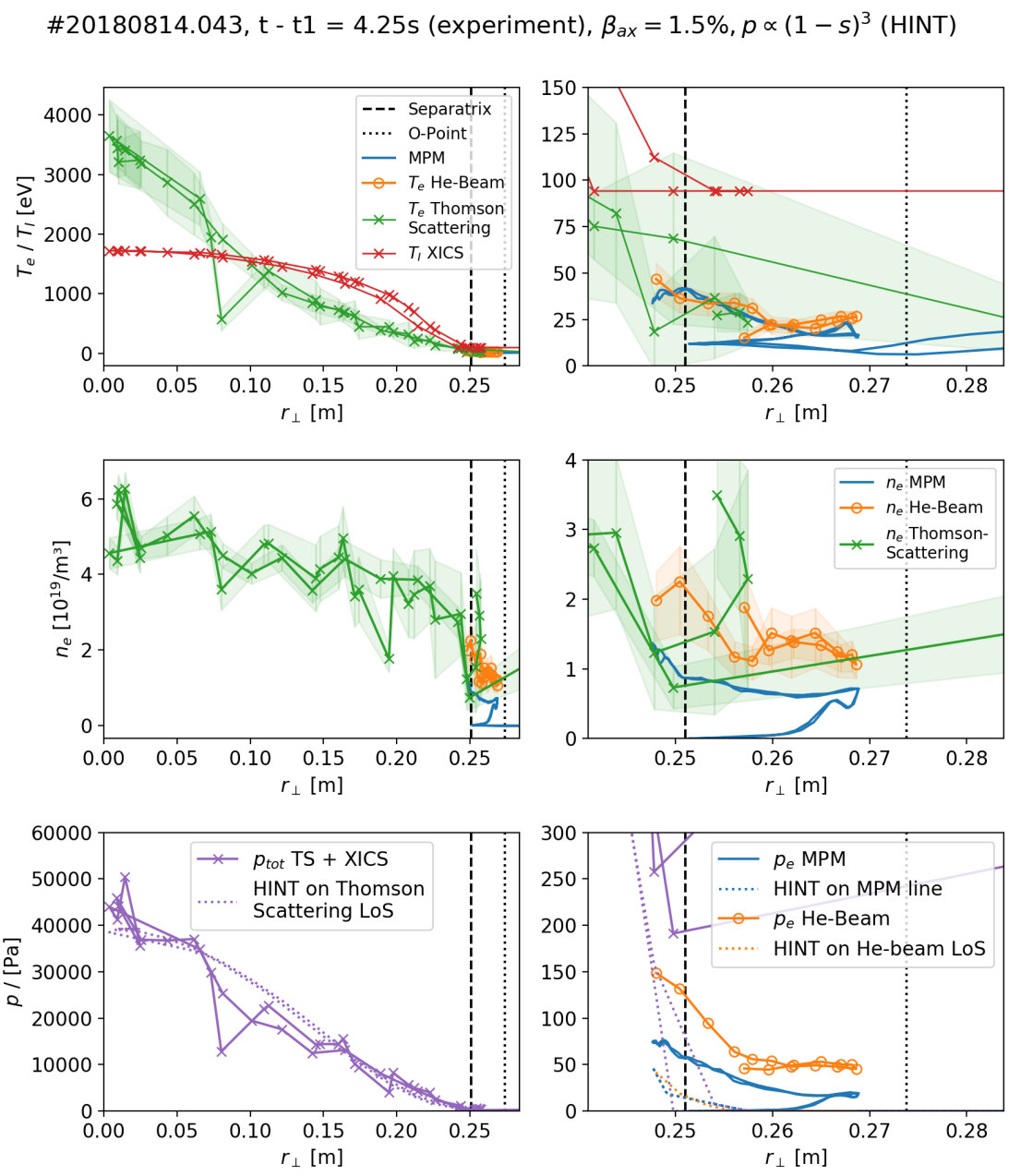

Figure 5.5: Electron temperature and -density profiles for Thomson-Scattering, He-Beam and MPM in $r_\perp$ coordinate. Lines indicate the radial ordering of the observed datapoints. The black lines indicate estimations for the last closed flux-surface and the island O-point based on $r_\perp$ analysis of the $\phi = 0°$ and $\phi = 180°$ planes.

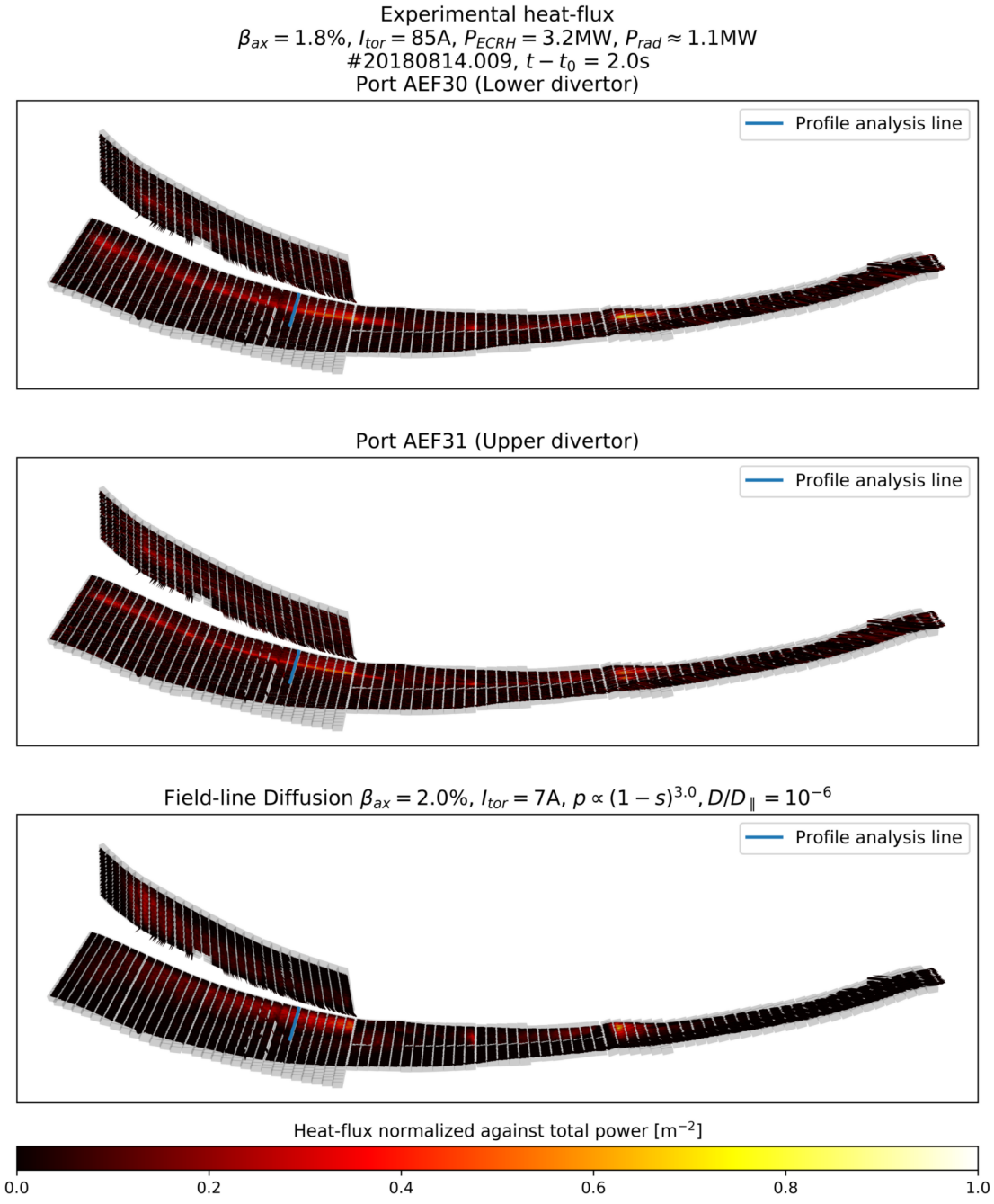

Figure 5.6: Comparison of an infrared observation sample and a corresponding heat-flux simulation. All images show normalized heat-fluxes. For experimental measurements, the convective divertor power was approximated as $P_{\mathrm{ECRH}} - P_{\mathrm{rad}}$

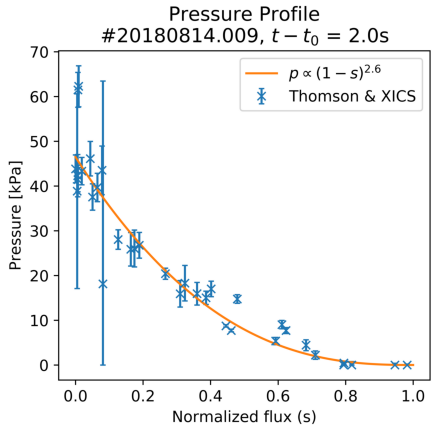

Figure 5.7: Pressure profile obtained from XICS and Thomson Scattering, as well as reduced low-degree-of-freedom fit, both plotted against normalized toroidal flux.

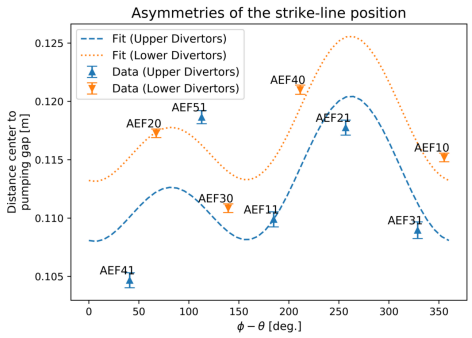

Figure 5.8: Estimation of the systematic port-to-port deviation using up-down asymmetry and 1/1 and 2/2 contributions, plotted against $\iota = 1$ helical angle.

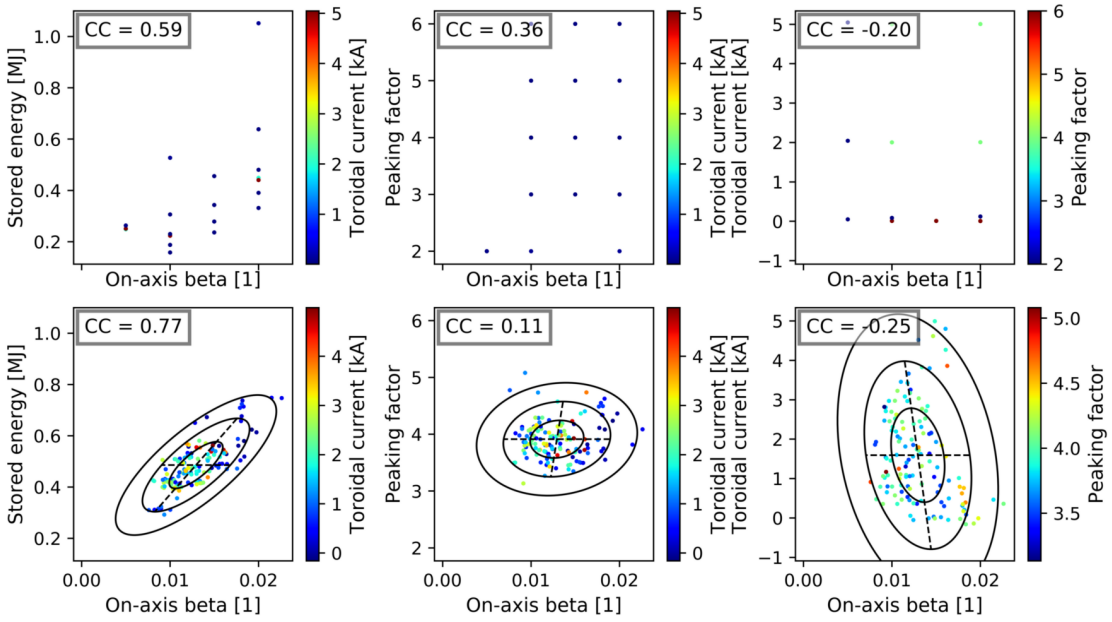

Figure 5.9: Overview of the grid of HINT runs (upper) and corresponding experimental data (lower). Ellipses mark the $1\sigma, 2\sigma$ and 3σ intervals around the data. Dashed lines indicate the principal components. Cross-correlations of x- and y-axis are indicated in the top corner.

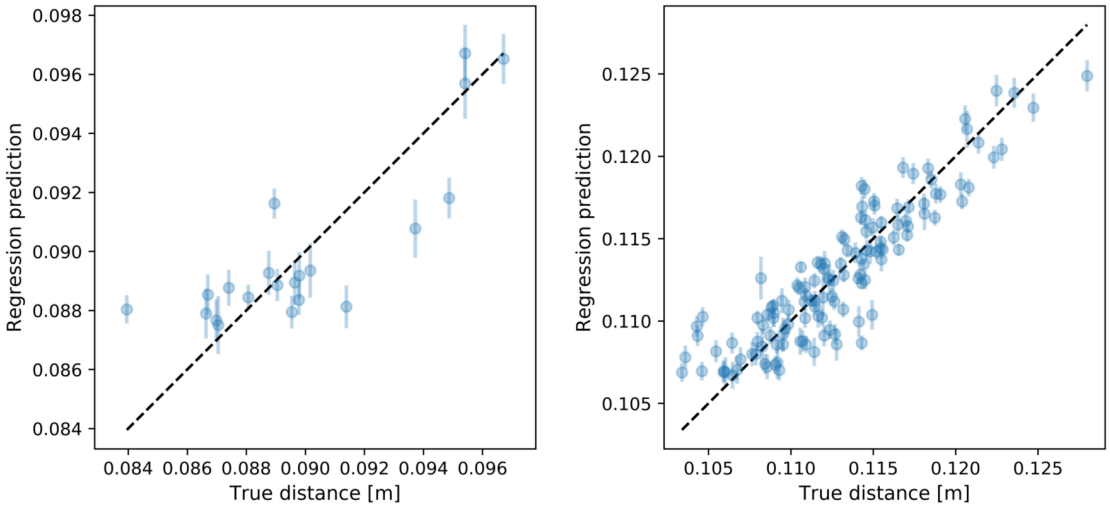

Figure 5.10: Errors (deviation from $x = y$-line) and uncertainties (error bar) for the linear strike-line position regression (y-axis) in the synthetic (left) and the experimental dataset (right) against the actual distances of the strike-line's weighted center from the pumping gap for the synthetic (left) and experimental (right) strike-line data (x-axis).

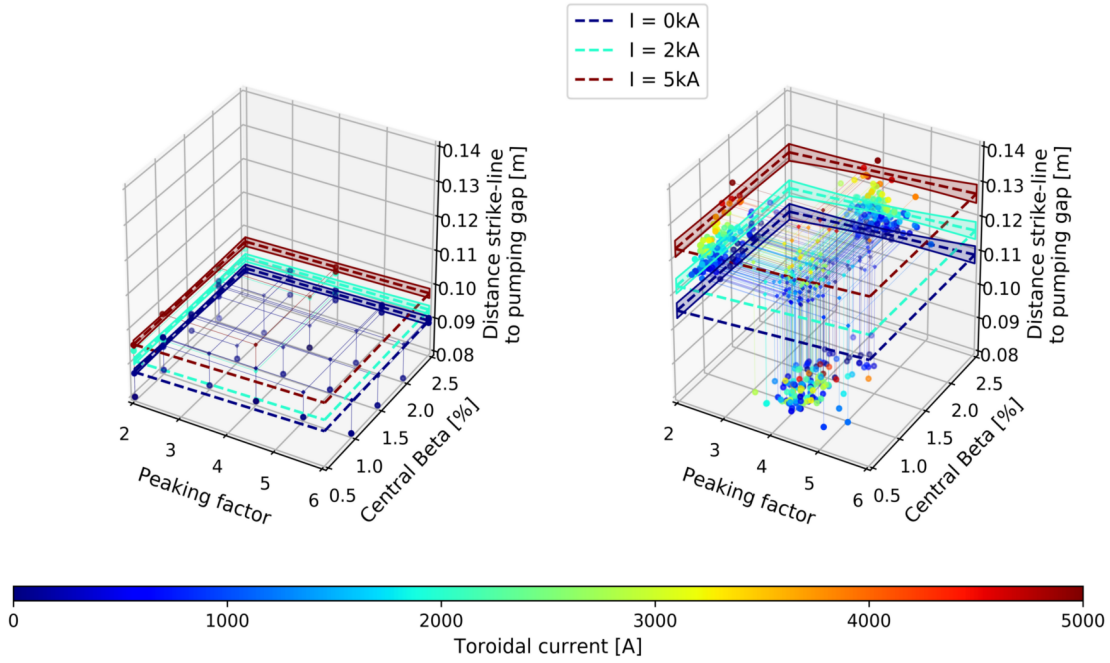

Figure 5.11: 4D dataset plots of central beta, pressure profile peaking factor, toroidal plasma current (via color) and distance from strike-line to pumping gap (thin points), connected to three of their projections into 3D datasets (with the third dimension indicated by color color), together with a linear fit of the dataset indicated with dashed lines

6 Equilibrium magnetic topology and divertor heat-loads in simulated high-beta plasmas

This chapter holds the main result of this thesis, the analysis of plasma beta effects on the edge magnetic field structure, and the derived effects on the divertor heat loads. The results are reviewed on a per-configuration basis for the standard (5/5)-, high-iota (5/4)-, and low-iota-(5/6)-configuration. For each configuration, two main studies were performed. First, central and volume-averaged beta were varied together by varying the on-axis plasma beta from 0 (vacuum case) to 5%. Afterwards, the volume-averaged beta was varied at $\beta_{\mathrm{axis}} = 5\%$ by varying the pressure profile shape. An overview of the obtained heat-load distributions is provided in table 6.1, and discussed in the sections of each individual configuration. The calculated quantities are:

- Expected peak heat-fluxes on individual components, normalized to the total power
- Power-load distribution to the individual components
- Estimated total power limitations for attached divertor conditions derived from the peak-loads, as well as information about the limiting components

Components were abbreviated as follows:

- V = Vertical divertor target plate
- HL = Horizontal target plate, low-iota front section
- HH = Horizontal target plate, high-iota tail section
- HM = Horizontal target plate, center section
- Baf = Divertor baffle tiles
- U-P = Outboard diagnostic port in the triangular ($\phi = 180°$ and equivalent) planes, labeled "U-Port"

These abbreviations match the labels in figure 1.7. Simulations were performed both for $D_\perp = 0.3\,\mathrm{m^2\,s^{-1}}$, where strike-line comparisons match more closely between modeling and experiment, and $D_\perp = 1\,\mathrm{m^2\,s^{-1}}$, which have a more accurate match to the wetted area measurements in [67].

All predictions presented in this chapter are original work performed by the author, based on the tools outlined in chapter 3.

						Limit				Peak Flux							Load							Wetted Area
					$\int pdV$	Divertor		Baf.	U-P.	Divertor					Baf.	U-P.	Divertor					Baf.	U-P.	Divertor
Config.	β_{ax}	$p(s)$	I_{tor} [kA]	$D/D_{\parallel}$		P_{max}	By	P_{max}	P_{max}	V	HL	HM	HH	Total			V	HL	HM	HH	Total			
5/4	0.0	Vac	Vac	10^{-6}	0	0.7	HM	0.8	0.7	0.9	0.1	0.7	1.3	1.3	0.3	0.3	29%	8%	5%	56%	97%	2%	1%	0.8
				10^{-7}	0	0.8	HM	2.2	-	0.9	0.1	0.7	2.1	2.1	0.1	0.1	19%	3%	3%	75%	99%	0%	0%	0.5
	2.0	$(1-s)^{5.0}$	0.0	10^{-6}	221	0.9	HM	0.7	0.3	0.7	0.2	0.5	1.0	1.0	0.4	0.7	22%	10%	4%	52%	88%	4%	8%	0.8
				10^{-7}	221	0.8	HM	3.1	-	0.7	0.1	0.6	2.1	2.1	0.1	0.1	15%	3%	2%	80%	99%	0%	0%	0.5
		$1-s$	0.0	10^{-6}	868	0.8	HM	2.0	0.4	0.5	0.1	0.6	1.3	1.3	0.1	0.5	16%	7%	4%	70%	96%	1%	3%	0.7
				10^{-7}	868	0.9	HM	6.7	1.5	0.3	0.0	0.6	1.9	1.9	0.0	0.1	6%	2%	2%	89%	99%	0%	1%	0.5
	5.0	$(1-s)^{3.0}$	0.0	10^{-6}	768	0.8	HM	3.5	0.5	0.4	0.1	0.6	1.2	1.2	0.1	0.4	12%	7%	4%	73%	96%	1%	3%	0.8
				10^{-7}	768	0.9	HM	0.4	0.0	0.4	1.0	0.5	1.7	1.7	0.6	4.2	6%	4%	1%	73%	84%	3%	13%	0.5
		$(1-s)^{5.0}$	0.0	10^{-6}	541	0.9	HM	1.0	0.6	0.4	0.1	0.6	1.2	1.2	0.2	0.3	14%	8%	4%	70%	96%	1%	3%	0.8
				10^{-7}	541	1.0	HM	5.5	1.1	0.3	0.0	0.5	1.8	1.8	0.0	0.2	9%	3%	2%	85%	98%	0%	1%	0.6
		$1-s$	0.0	10^{-6}	1609	1.0	HM	2.4	0.3	0.1	0.1	0.5	1.1	1.1	0.1	0.8	4%	6%	3%	78%	92%	1%	7%	0.8
				10^{-7}	1609	1.1	HM	8.1	0.1	0.1	0.0	0.5	1.6	1.6	0.0	1.9	1%	2%	1%	91%	95%	0%	4%	0.6
5/5	0.0	Vac	Vac	10^{-6}	0	1.4	HM	1.0	-	0.4	0.5	0.4	0.7	0.7	0.3	0.0	27%	42%	14%	9%	92%	8%	1%	1.3
				10^{-7}	0	1.3	HM	2.1	-	0.6	0.7	0.4	0.4	0.7	0.1	0.0	23%	62%	9%	4%	97%	3%	0%	1.3
	2.0	$(1-s)^{3.0}$	0.0	10^{-6}	480	1.6	HM	1.5	-	0.3	0.5	0.3	0.5	0.5	0.2	0.0	26%	46%	12%	8%	92%	8%	1%	1.7
				10^{-7}	480	1.8	HM	4.4	-	0.5	0.7	0.3	0.3	0.7	0.1	0.0	25%	64%	6%	3%	98%	2%	0%	1.4
		$(1-s)^{5.0}$	0.0	10^{-6}	331	1.4	HM	1.4	-	0.3	0.5	0.4	0.6	0.6	0.2	0.0	26%	45%	13%	8%	92%	8%	1%	1.6
				10^{-7}	331	1.9	HM	3.8	-	0.5	0.7	0.3	0.3	0.7	0.1	0.0	24%	65%	6%	3%	98%	2%	0%	1.3
		$1-s$	0.0	10^{-6}	1052	1.8	HM	1.8	-	0.3	0.4	0.3	0.5	0.5	0.1	0.1	24%	47%	12%	9%	92%	8%	1%	1.7
				10^{-7}	1052	2.1	HM	4.8	-	0.5	0.7	0.2	0.3	0.7	0.1	0.0	23%	65%	6%	3%	98%	2%	0%	1.4
	5.0	$(1-s)^{3.0}$	0.0	10^{-6}	1091	1.8	HM	2.3	-	0.3	0.4	0.3	0.5	0.5	0.1	0.1	26%	49%	10%	7%	92%	8%	1%	2.0
				10^{-7}	1091	2.1	HM	3.1	-	0.5	0.7	0.2	0.3	0.7	0.1	0.0	33%	59%	4%	2%	98%	2%	0%	1.4
		$(1-s)^{5.0}$	0.0	10^{-6}	792	1.7	HM	2.0	-	0.3	0.4	0.3	0.5	0.5	0.1	0.0	26%	48%	11%	7%	92%	8%	1%	1.8
				10^{-7}	792	2.0	HM	5.3	-	0.5	0.7	0.3	0.3	0.7	0.0	0.0	30%	62%	4%	2%	98%	2%	0%	1.4
		$1-s$	0.0	10^{-6}	2584	2.5	HM	0.7	0.7	0.3	0.4	0.2	0.3	0.4	0.3	0.3	19%	52%	8%	8%	86%	12%	2%	2.1
				10^{-7}	2584	2.4	HM	1.2	-	0.5	0.7	0.2	0.2	0.7	0.2	0.1	27%	64%	3%	2%	95%	4%	0%	1.4
			5.0	10^{-6}	2422	2.8	HM	0.9	0.7	0.3	0.3	0.2	0.3	0.3	0.3	0.3	21%	52%	8%	8%	88%	10%	1%	2.7
				10^{-7}	2422	3.0	HM	1.9	-	0.6	0.6	0.2	0.2	0.6	0.1	0.1	28%	64%	3%	2%	97%	3%	0%	1.6
			10.0	10^{-6}	2442	2.5	HM	0.9	0.8	0.3	0.3	0.2	0.3	0.3	0.3	0.2	21%	52%	7%	9%	89%	10%	1%	2.8
				10^{-7}	2442	3.3	HM	2.2	-	0.6	0.5	0.2	0.2	0.6	0.1	0.1	26%	66%	3%	2%	97%	2%	0%	1.7
5/5 HM	0.0	Vac	Vac	10^{-6}	0	2.7	HM	0.3	-	0.9	0.4	0.2	0.6	0.9	0.8	0.0	61%	16%	6%	4%	84%	15%	1%	0.9
				10^{-7}	0	2.5	HM	0.5	-	1.1	0.4	0.2	0.3	1.1	0.6	0.0	79%	12%	2%	2%	93%	7%	0%	0.9
	2.0	$1-s$	0.0	10^{-6}	856	3.1	HM	0.4	-	0.7	0.3	0.2	0.5	0.7	0.6	0.1	63%	16%	5%	5%	87%	12%	1%	1.3
				10^{-7}	856	3.2	HM	0.8	-	1.1	0.4	0.2	0.4	1.1	0.3	0.0	82%	10%	2%	2%	95%	5%	0%	0.9
	5.0	$(1-s)^{3.0}$	0.0	10^{-6}	903	3.2	HM	0.7	-	0.5	0.3	0.2	0.5	0.5	0.4	0.1	61%	18%	5%	4%	87%	12%	1%	1.6
				10^{-7}	903	2.9	HM	0.8	-	0.9	0.5	0.2	0.3	0.9	0.3	0.0	78%	13%	2%	2%	94%	5%	0%	1.1
		$(1-s)^{5.0}$	0.0	10^{-6}	626	2.8	HM	0.5	-	0.6	0.3	0.2	0.5	0.6	0.5	0.1	62%	18%	5%	4%	86%	12%	1%	1.5
				10^{-7}	626	2.8	HM	1.6	-	1.0	0.5	0.2	0.3	1.0	0.2	0.0	79%	13%	2%	2%	95%	5%	0%	1.0
		$1-s$	0.0	10^{-6}	2113	3.4	HM	0.7	0.9	0.6	0.3	0.1	0.4	0.6	0.4	0.2	57%	22%	4%	5%	87%	10%	2%	1.5
				10^{-7}	2113	3.0	HM	0.7	-	0.9	0.5	0.2	0.2	0.9	0.4	0.1	74%	18%	1%	1%	94%	5%	0%	1.0
5/6	0.0	Vac	Vac	10^{-6}	0	5.1	HM	0.2	-	0.1	0.5	0.1	0.1	0.5	1.3	0.0	3%	72%	5%	1%	80%	18%	2%	1.6
				10^{-7}	0	4.4	HM	0.4	-	0.0	0.9	0.1	0.0	0.9	0.7	0.0	1%	92%	2%	0%	95%	5%	0%	1.1
	2.0	$(1-s)^{5.0}$	0.0	10^{-6}	363	5.4	HM	0.3	-	0.1	0.5	0.1	0.1	0.5	0.9	0.0	2%	76%	5%	1%	83%	15%	2%	1.5
				10^{-7}	363	5.6	HM	0.7	-	0.0	0.9	0.1	0.0	0.9	0.4	0.0	1%	94%	2%	0%	96%	3%	0%	1.1
		$1-s$	0.0	10^{-6}	1145	6.0	HM	0.4	-	0.1	0.6	0.1	0.1	0.6	0.6	0.0	1%	82%	4%	1%	88%	11%	1%	1.4
				10^{-7}	1145	8.2	HM	2.0	-	0.0	1.0	0.1	0.0	1.0	0.1	0.0	0%	96%	2%	0%	98%	2%	0%	1.0
	5.0	$(1-s)^{3.0}$	0.0	10^{-6}	1007	6.8	HM	0.6	-	0.1	0.7	0.1	0.0	0.7	0.4	0.0	1%	84%	4%	1%	88%	11%	1%	1.3
				10^{-7}	1007	8.3	HM	3.9	-	0.0	0.9	0.1	0.0	0.9	0.1	0.0	0%	96%	1%	0%	98%	2%	0%	1.1
		$(1-s)^{5.0}$	0.0	10^{-6}	691	6.1	HM	0.4	-	0.1	0.6	0.1	0.0	0.6	0.6	0.0	1%	81%	4%	1%	86%	12%	1%	1.4
				10^{-7}	691	8.1	HM	1.7	-	0.0	0.9	0.1	0.0	0.9	0.1	0.0	0%	95%	2%	0%	97%	2%	0%	1.1
		$1-s$	0.0	10^{-6}	2203	6.3	HM	1.3	-	0.0	0.8	0.1	0.0	0.8	0.2	0.0	0%	83%	3%	0%	87%	12%	1%	1.1
				10^{-7}	2203	8.2	HL	2.5	-	0.0	1.2	0.0	0.0	1.2	0.1	0.0	0%	96%	1%	0%	96%	3%	0%	0.8

Table 6.1: Overview of power limits, peak normalized heat fluxes and heat-flux distributions in calculated scenarios. The first columns indicate magnetic configuration, plasma beta, toroidal current and diffusion coefficients. For convenience, the stored energy is also included. Limits are indicated for divertor plate (including the limiting subsection), divertor baffles and U-port heat-shield. Peak fluxes are indicated for all divertor subtargets, the divertor plate as a whole, divertor baffles and the U-port heat-shield. Likewise, integrated load distributions are reported for these areas.

6.1 Standard configuration (5/5)

Figure 6.1 shows the influence of overall plasma beta on the standard configuration's edge magnetic field structure. As on-axis plasma beta increases, the separatrix of the island chain begins to show stochastization. However, even at high plasma beta, a structured set of nested flux surfaces remains intact both surrounding, as well as in the interior of the island chain. The outboard stochastic side of the island intersects slightly with the U-port in the triangular plane (see figure 1.6 for location of these ports). However, no significant heat-flux was visible on this port in the $p \propto s$ cases even at 5% central beta. At higher plasma beta, the edge islands near the divertor plates are moved slightly inwards (towards the center of the machine, not the magnetic axis). This changes the connection structure of the island. Where in the vacuum field only the bottom left part of the separatrix connected directly to the divertor, the shift of the island causes first a connection to the vertical target plate and then, at higher plasma beta, a connection to the outboard side

of the divertor island. The heat-load distribution on the divertor (shown in figure 6.3[1]) reflects this behavior directly, forming first an additional strike-line on the vertical target plate and then a secondary (albeit weak) strike-line on the horizontal target. While peak heat-loads vary in the high-load areas (mostly HL and V), the load-limiting middle section appears to be subjected to a constant normalized peak-flux of $0.1\,\mathrm{MW\,m^{-2}}$, which limits the convective divertor power to about 2 MW (see table 6.1).The main power-limiting heat-loads in the high-beta simulations, however, are substantial heat loads on the divertor baffle tiles, with peak heat-fluxes on the baffle tiles approaching $0.5\,\mathrm{m^{-2}}$, theoretically limiting the total power to less than 0.5 MW.

The area of the stochastic region in the edge does not appear to have a significant dependence on volume averaged beta at fixed central beta (as shown in the profile scan in figure 6.2). However, the separatrix shape and the position of the island's O-point react to the change in profile like they react to the change in central beta. This indicates that the primary driver for the island shaping effect is the central pressure, while the stochastization depends on volume integrated pressure.

[1] Due to layout constraints, the order of figures in this chapter deviates from the order in which they are mentioned in the main text.

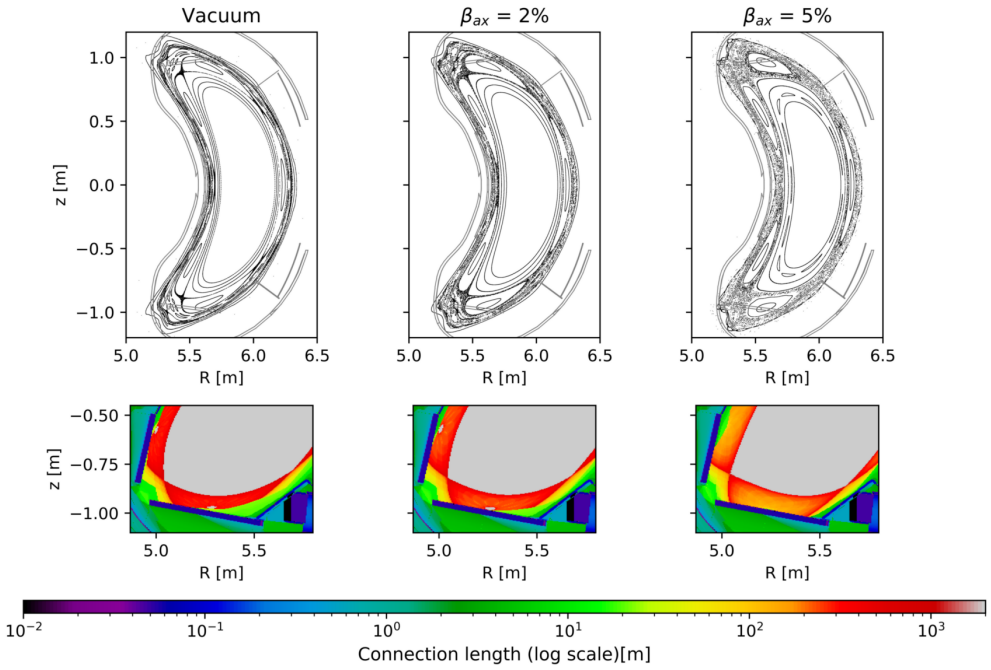

Figure 6.1: : Plasma response in standard configuration at fixed pressure profile ($p \propto 1 - s$) to changes in axial beta for vacuum case (left), $\beta_{ax} = 2\%$ (middle) and $\beta_{ax} = 5\%$ (right). Poincaré-maps are shown in the $\phi = 0°$ plane (bean-plane), while connection-length distributions are plotted at the front (low-iota) end of the divertor plate.

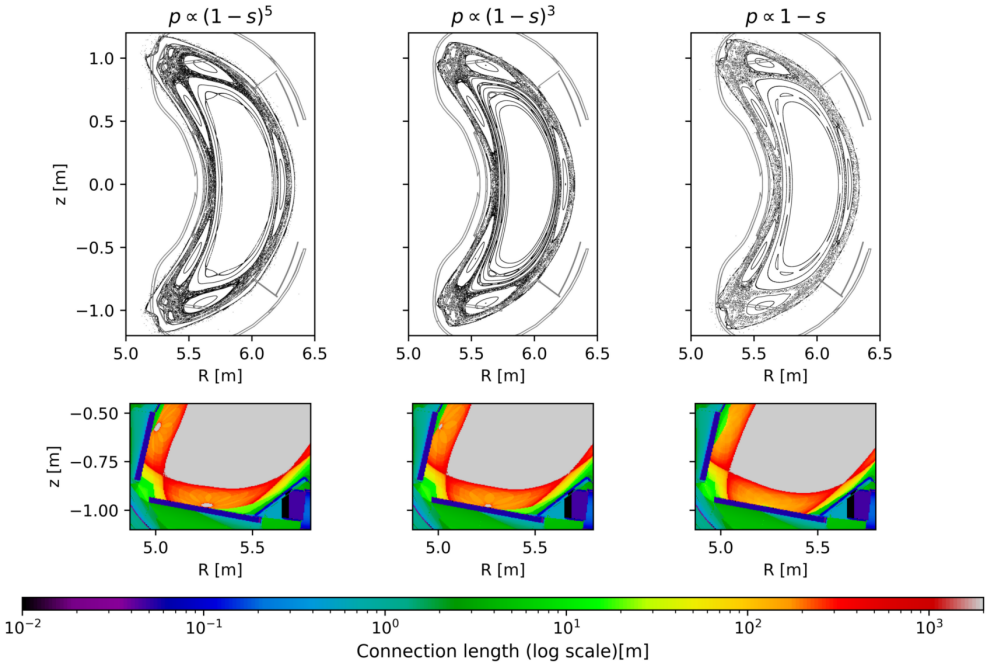

Figure 6.2: : Plasma response in standard configuration at fixed axial beta ($\beta_{\mathrm{ax}} = 5\%$) to changes in pressure profile shape, with $p \propto (1-s)^5$ (left), $p \propto (1-s)^3$ (center) and $p \propto 1 - s$ (right). Poincaré-maps are shown in the $\phi = 0°$ plane (bean-plane), while connection-length distributions are plotted at the front (low-iota) end of the divertor plate.

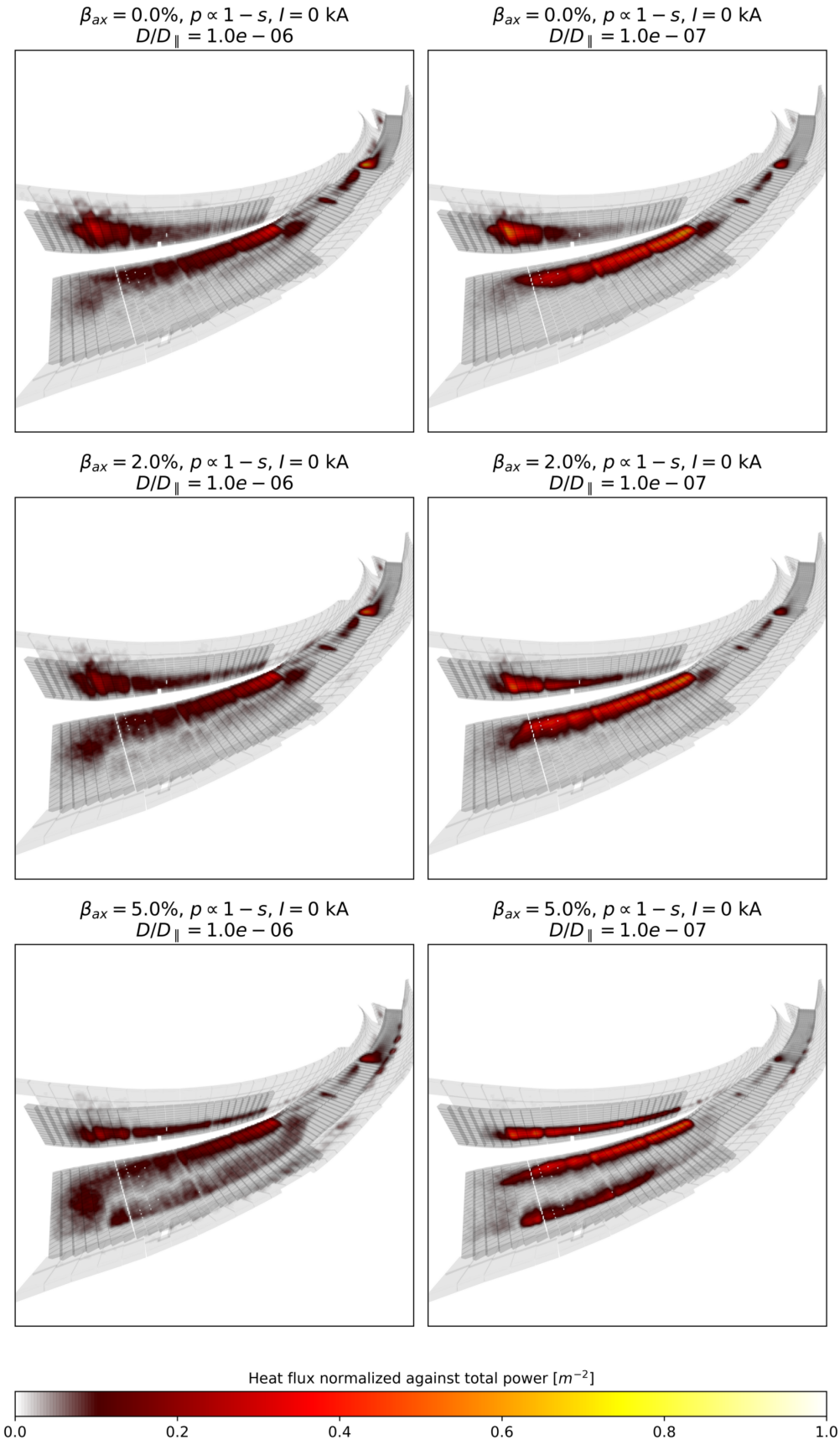

Figure 6.3: Changes in divertor heat-loads in standard configuration with increasing axial beta.

6.2 High-Iota configuration (5/4)

In the $\iota = n/m = 5/4$ configuration, the edge islands form a single flux tube winding helically around the plasma core. The vacuum configuration features no nested flux surfaces outside of the edge islands. Therefore, these islands are highly susceptible to stochastization due to the lack of nested magnetic surfaces outside the island-region [22, 16]. As figure 6.4 shows, the nested magnetic surface structure of the islands is lost with increasing beta. This can be attributed to the growth of the edge islands with increasing beta. As the edge islands grow, the overlap with the outer stochastic region increases, which leads to a loss of the islands' nested flux surface structure. However, the connection-length distribution reveals a deterministic lobe-like structure in the chaotic Poincaré-map. It can also be seen from both figures that, although the microscopic edge structure becomes increasingly chaotic at high beta, the O- and X-point position of the lowest-mode perturbation remains remarkably stable.

Nonetheless, the distortion of the separatrix due to the stochastization has visible effects on the edge magnetic field topology. In the low-beta cases, the separatrix of the island chain passes the vertical target nearly tangentially by less than 1 cm. As plasma beta increases, this part of the separatrix retracts from the vertical target, and the heat flux is redistributed toward the tail of the horizontal divertor plate (see figure 6.5), balancing out the divertor heat-load. The strike-line width itself, however, appears to be mostly unaffected by the stochastization effects. The stochastization of the magnetic island region also appears to have a dependency on the pressure profile at fixed central beta, but the magnetic islands are not fully recovered in the cases with high central plasma beta ($\beta_{\mathbf{ax}} = 5\%$) and low volume-averaged beta ($\beta_{\mathbf{vol}} = 0.5\%$) (figure 6.6).

As seen in table 6.1, the high-iota configuration is subject to the highest peak heat-fluxes (at above $1.5\,\mathrm{m}^{-2}$) onto the divertor target plate. This creates the somewhat unique situation that the divertor heat-loads are sometimes not limited by the loads onto the middle section but by the strongly focused peak loads on the high-iota tail section (HH). The exact limitation scenario is sensitive to the perpendicular diffusion coefficient, as an increase of diffusivity in the edge both defocuses the heat-loads on the high-iota tail and increases the indirect (supplied by diffusion) heat-flow onto the middle section. Similarly sensitive to the diffusivity is the limitation imposed by the baffle heat-loads. As can be seen in figure 6.7, this is mainly related to a set of baffle tiles sitting right above the vertical target. Since the closeby passing separatrix recedes with increasing plasma beta, this area is progressively unloaded as plasma pressure increases. This effect is, however, substantially less pronounced at high edge diffusivity.

At high plasma beta, the outboard side of the triangular-plane cross-section (figure 6.4, middle row) starts - due to the stochastization - overlapping with the plasma-facing components. As can be seen in figure 6.8, this can lead to the deposition of a substantial amount of power onto the horizontal port in this plane, with up to 13% of the total heating power being deposited near the five U-ports (see figure 1.5 for the location of these ports). A significant share of this power is deposited onto small spots (estimated at about $0.7\,\mathrm{dm}^2$ per spot) at the edge of the port. For steady-state operation, care must be taken in this configuration in high-performance scenarios, as these heat-loads could quickly exceed the heat-dissipation ability of the cooling system.

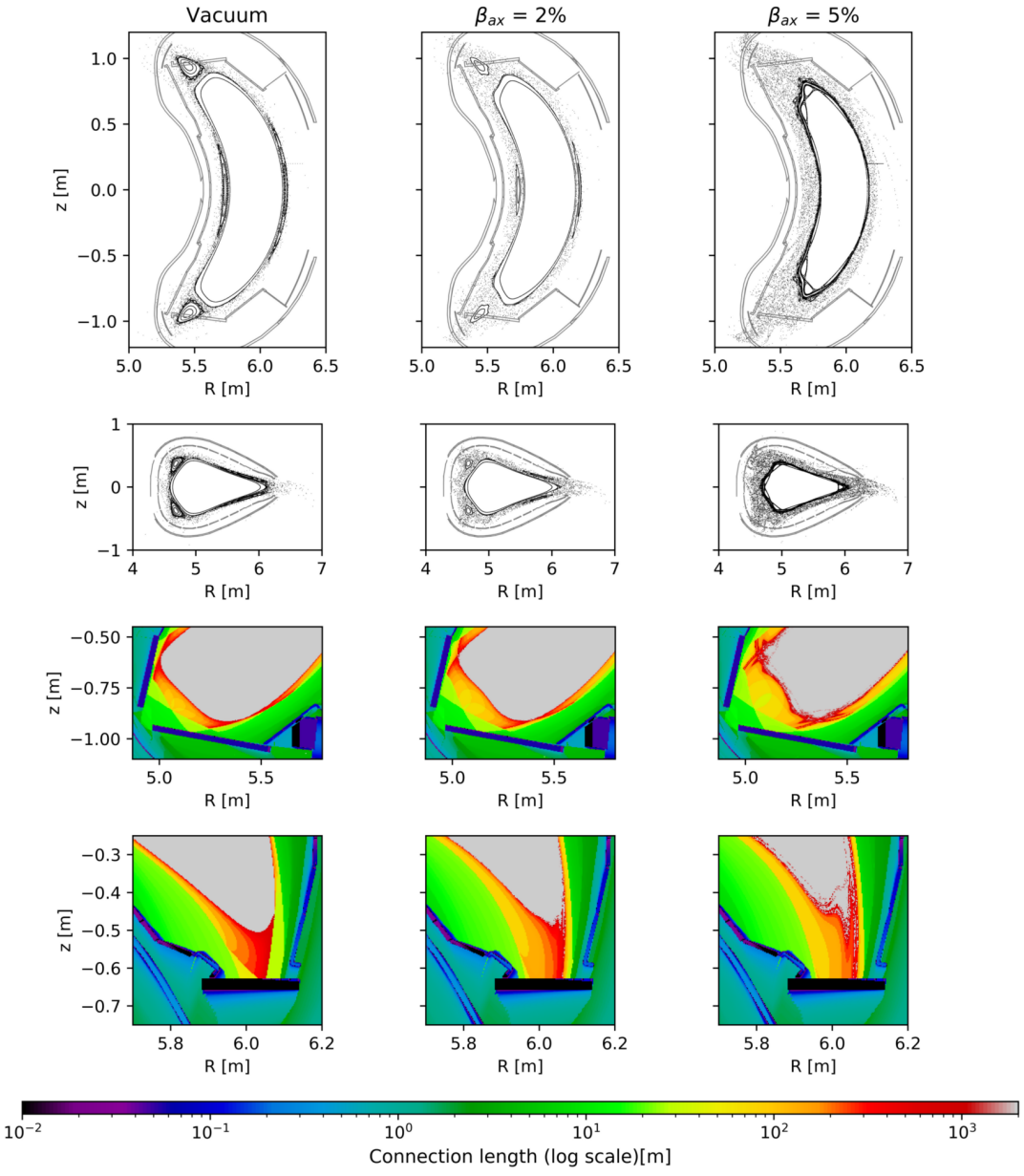

Figure 6.4: Plasma response in high-iota configuration at fixed pressure profile ($p \propto 1 - s$) to changes in axial beta for vacuum case (left), $\beta_{ax} = 2\%$ (middle) and $\beta_{ax} = 5\%$ (right). Poincaré-maps are shown in the $\phi = 0°$ plane (bean-plane, top) and the $\phi = 180°$ plane (triangular plane, middle), while connection-length distributions are plotted at the front (low-iota) end of the divertor plate

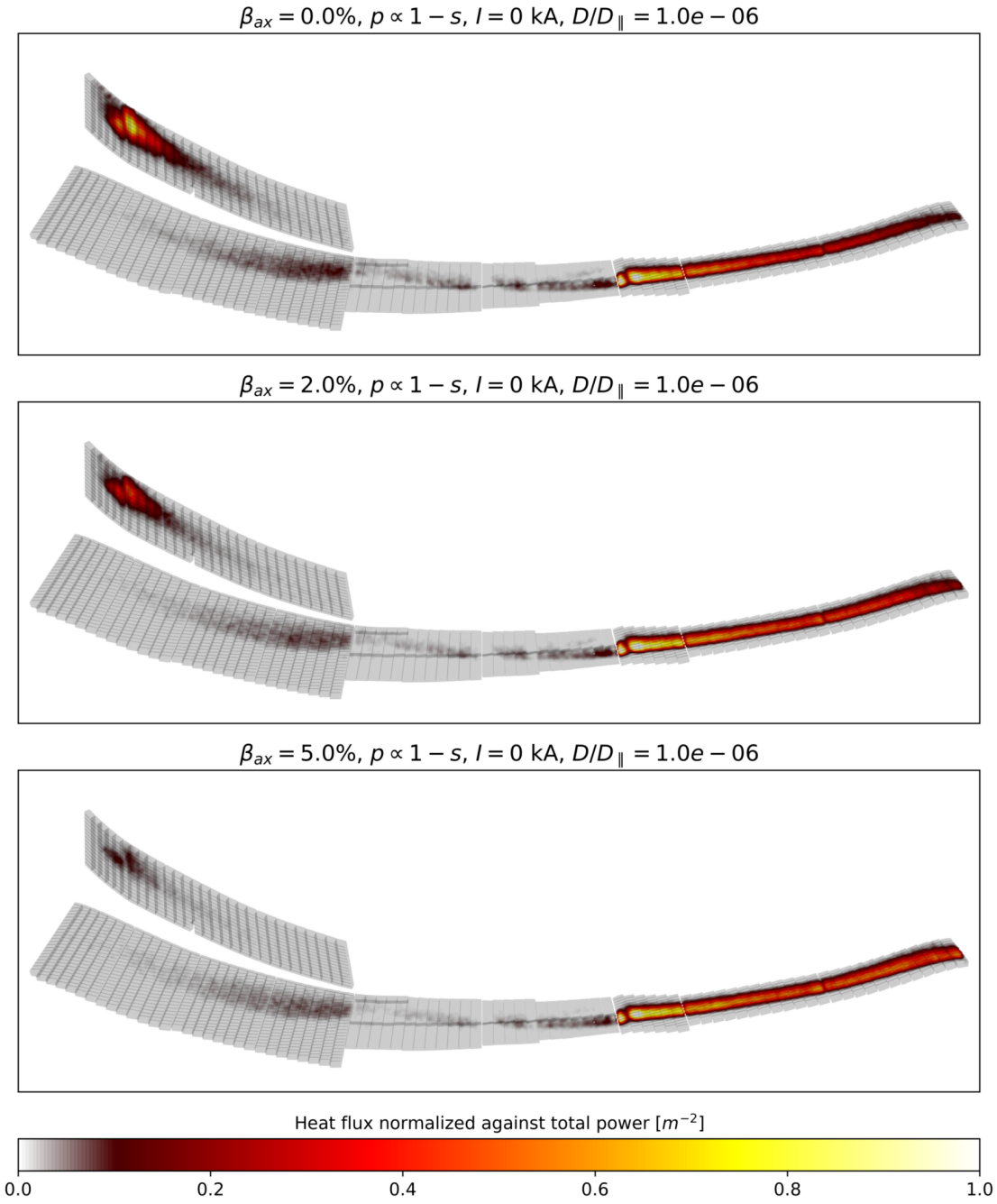

Figure 6.5: Divertor heat-load distributions in high-iota configuration for different central beta values

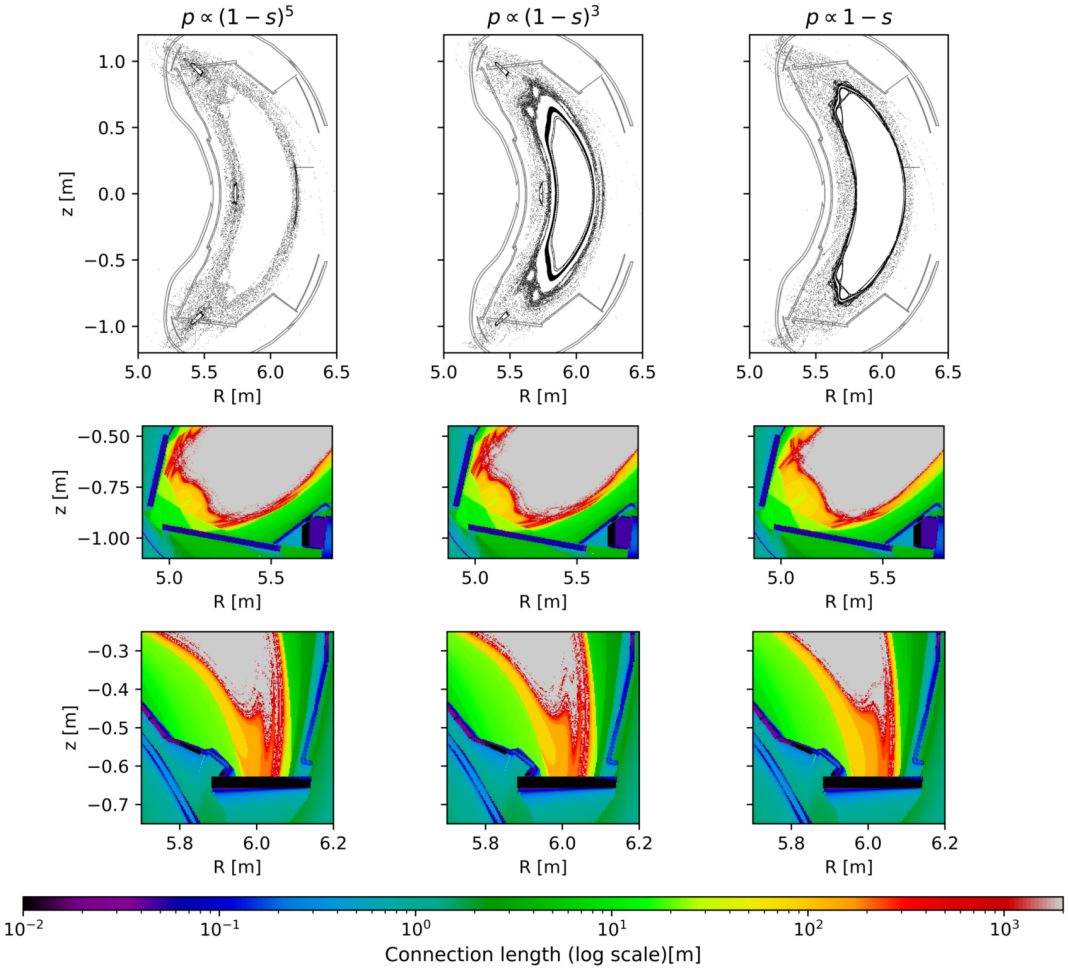

Figure 6.6: Plasma response in high-iota configuration at fixed axial beta ($\beta_{\mathrm{ax}} = 5\%$) to changes in pressure profile shape, with $p \propto (1-s)^5$ (left), $p \propto (1-s)^3$ (center) and $p \propto 1-s$ (right). Poincaré-maps are shown in the $\phi = 0°$ plane (bean-plane), while connection-length distributions are plotted at the front (low-iota) end of the divertor plate.

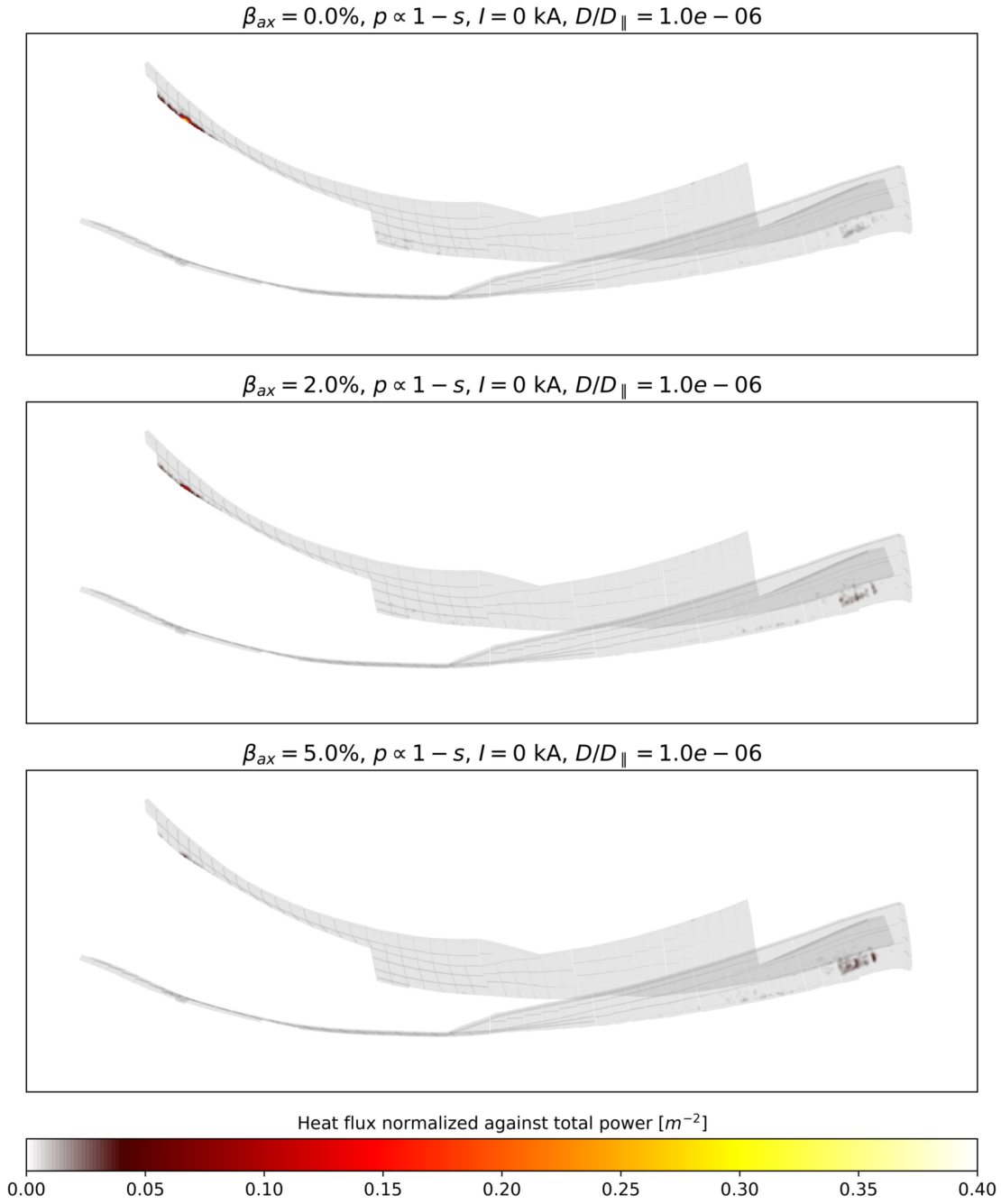

Figure 6.7: Divertor baffle heat-load calculations in high-iota configuration at different central beta values.

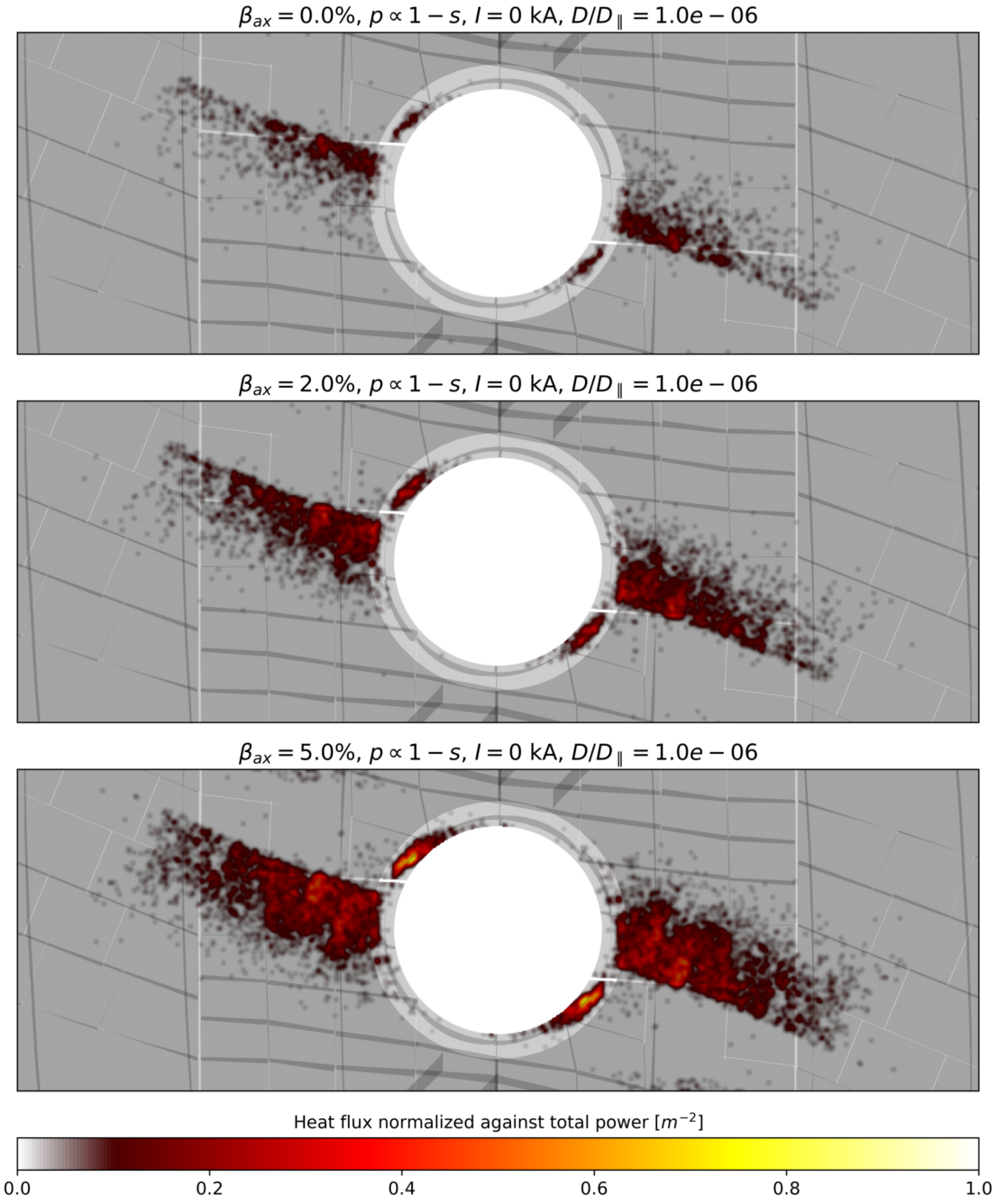

Figure 6.8: Heat-flux distributions on the outer U-port in high-iota configuration for a vacuum-field calculation (top), a $\beta_{\mathrm{ax}} = 5\%, \beta_{\mathrm{vol}} = 1.25\%$ case (middle) and a $\beta_{\mathrm{ax}} = 5\%, \beta_{\mathrm{vol}} = 2.5\%$ case (bottom)

6.3 Low-Iota configuration (5/6)

The 5/6 island ("low-iota") configuration also shows topological sensitivity to the plasma beta. As was first discovered in [24][2], the phase of the beta-driven 5/6 magnetic field component is opposite to the vacuum field's 5/6 component. The resulting annihilation of the 5/6 island chain (at around 5% plasma beta in this study, see figure 6.9) is beneficial for operation in standard configuration (as the presence of 5/6 islands in the core would degrade confinement). However, it has a detrimental effect when these islands are used as an island divertor, as discussed in [26]. As the islands shrink in size, the separatrix mostly disconnects from the divertor target plate (figure 6.9), and the overall magnetic topology changes towards a limiter-like configuration. The profile scan (figure 6.10) shows very similar behavior to the central beta scan, indicating that the change in the 5/6 component is probably related to volume averaged beta, with the $\beta_{\mathrm{ax}} = 5\%$ and $\beta_{\mathrm{vol}} = 0.5\%$ ($p \propto (1-s)^5$)-case showing almost the same magnetic topology as the vacuum case.

According to the field line diffusion simulations, the effect of this transition on the heat flux distribution (figure 6.11) is quite profound. As the pitch angle of the outer separatrix on the target plate decreases due to the shrinking islands, the wetted area increases at first due to a larger strike-line width. After the transition towards the limiter-like configuration, however, the heat flux is focused into a wide spot in front of the usual strike-line position. This circular structure was already observable in lower-beta experiments and showed a strong up-down asymmetry, which can be attributed to particle drifts in the magnetic field (see [69] for an in-depth discussion of these observations).

Due to the reduction in island width and the resulting transition towards a limiter-like configuration, the outboard baffle tiles near the front of the divertor experience additional heat-loads. While the total load on the baffles varies with the volume-averaged beta, the peak normalized heat-flux density is near $0.1m^{-2}$ in almost all of the scenarios (see table 6.1). As the circular divertor heat pattern lies on the same flux surface as the baffle hot-spots, particle drift effects might create similar up-down asymmetries in heat-flux intensity here.

It should be noted that the islands disappear due to a fairly precise cancellation of the plasma-driven- and vacuum magnetic field component. The island return at higher plasma beta at opposite island phase due to the plasma-driven magnetic field component overcoming the vacuum magnetic field. The required central beta values (around 7%) are, however, probably outside of the near-term experimentally achievable range.

[2] This initial work relied on a preliminary version of the planned W7-X coil set, which was changed afterwards. The same effect was then confirmed for the finalized coils in [68] and [16]

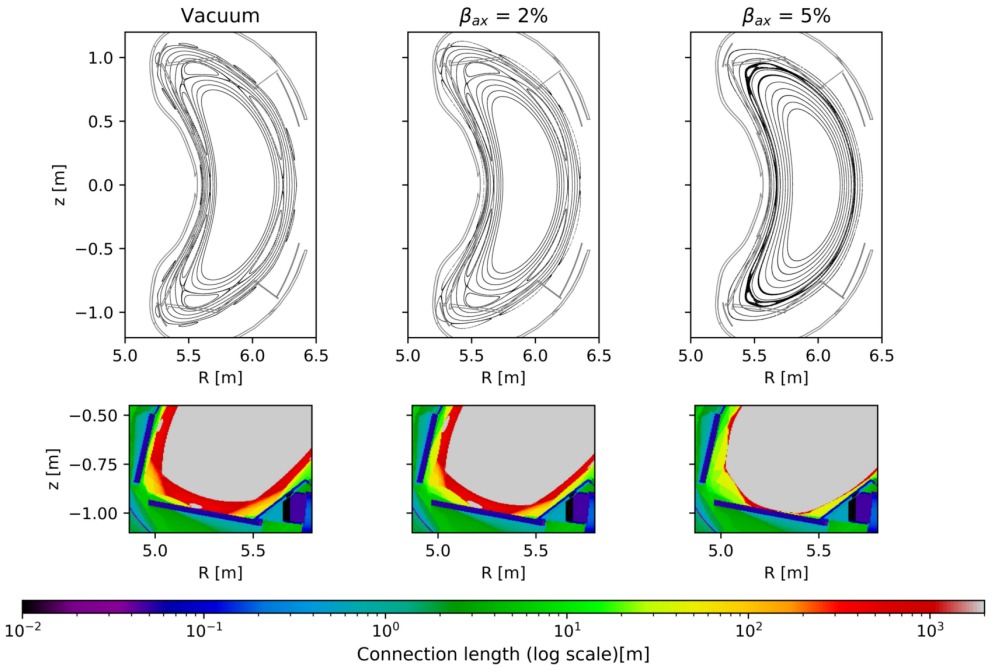

Figure 6.9: Plasma response in low-iota configuration at fixed pressure profile ($p \propto 1-s$) to changes in axial beta for vacuum case (left), $\beta_{ax} = 2\%$ (middle) and $\beta_{ax} = 5\%$ (right). Poincaré-maps are shown in the $\phi = 0°$ plane (bean-plane), while connection-length distributions are plotted at the front (low-iota) end of the divertor plate.

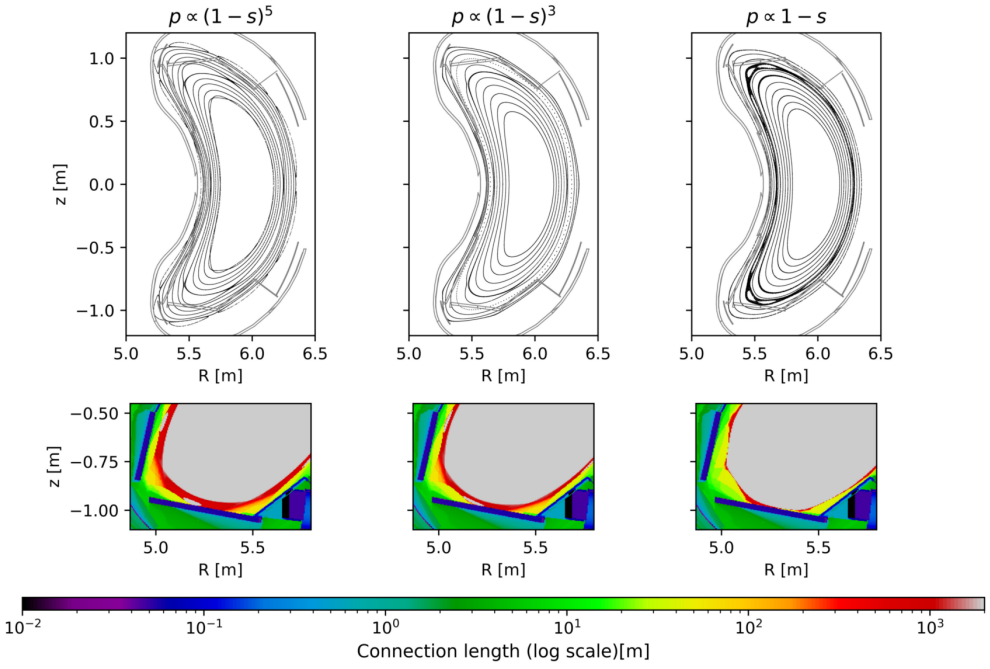

Figure 6.10: Plasma response in low-iota configuration at fixed axial beta ($\beta_{\mathrm{ax}} = 5\%$) to changes in pressure profile shape, with $p \propto (1-s)^5$ (left), $p \propto (1-s)^3$ (center) and $p \propto 1-s$ (right). Poincaré-maps are shown in the $\phi = 0°$ plane (bean-plane), while connection-length distributions are plotted at the front (low-iota) end of the divertor plate.

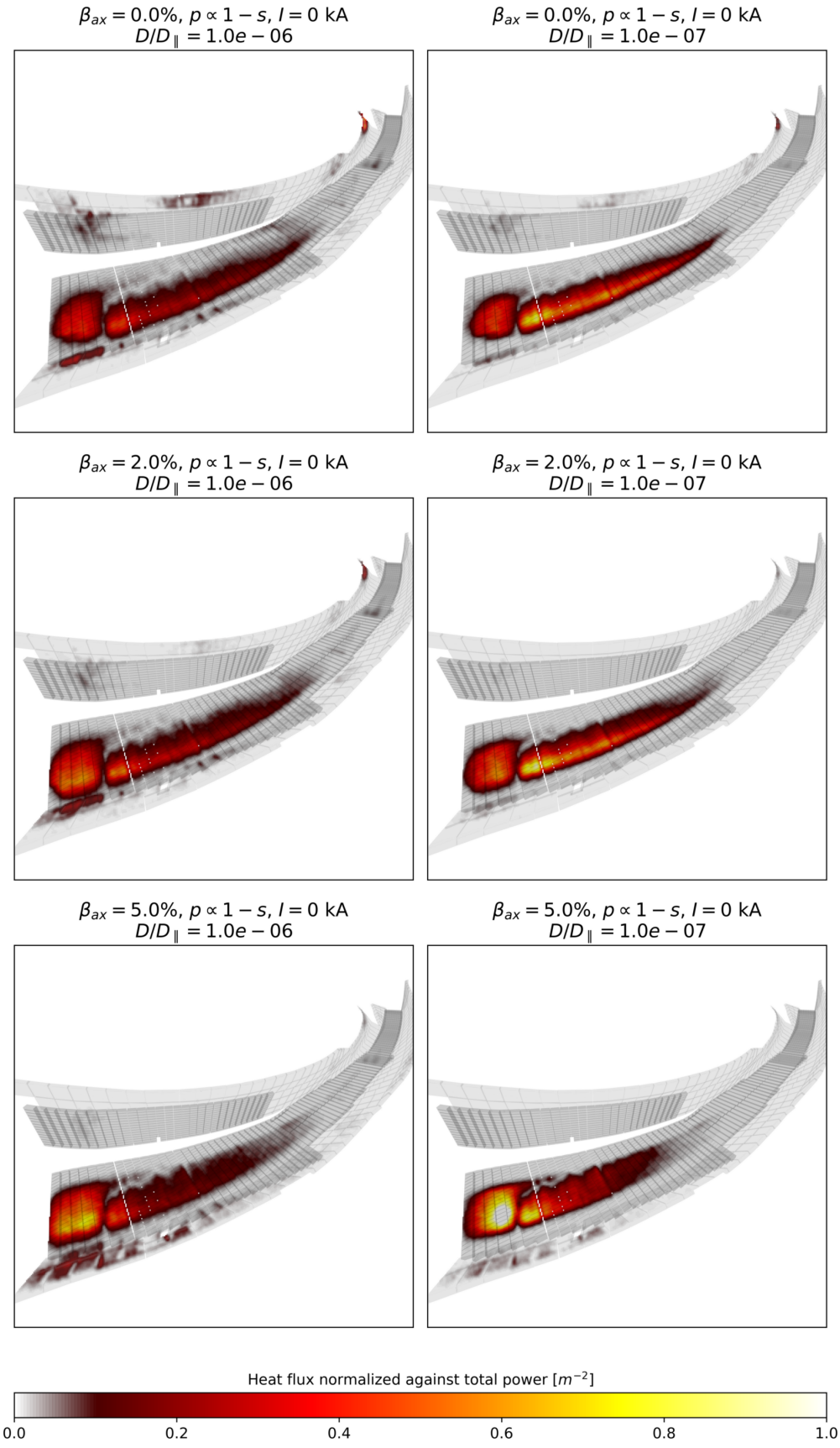

Figure 6.11: Divertor heat-load distributions in low-iota configuration for different central beta values

6.4 Summary

Applying the numerical methods introduced in chapter 3, this chapter showcased a detailed study of plasma-beta effects on heat-loads on the divertor of W7-X (and some other plasma-facing components). The standard-, high-iota-, and low-iota configurations were compared and systematically searched for detrimental heat-load changes. Out of the three compared configurations, it is clear that the standard configuration is by far the most stable candidate for high-beta operation, with the other two configurations showing significant degradation of the edge magnetic islands at higher plasma beta. The PFC heat-load distributions at high beta are summarized in the following points:

- The high- and low-iota sections of the divertor plate appear to be safe for high-power operation in all scenarios except low $D_\perp$ high-iota operation, where the narrow strike-line on the high-iota tail limits the power to about 6 MW.
- The middle section, which has a restricted heat flux limitation of $1\,\mathrm{MW\,m^{-2}}$, generally imposes the strictest divertor load limit of all four target sections.
- In almost all scenarios, the power-limit related to hot-spots on the baffles is far below the limit of the divertor plates themselves. The relevance of this limit is difficult to assess, as the baffles do not form a smooth geometry, and most of the loads are on or near the edges of the baffle tiles. Subtle erosion of the tiles during operation might sufficiently even out these loads.
- In high-iota configuration, care must be taken not to overload the U-port, as more heat flows into this region during high-beta operation.
- Depending on the edge diffusion coefficient, large heat-loads should be expected on the baffles during high-beta low-iota operation due to the limiter-like equilibrium topology. These loads are not toroidally elongated and focus a significant fraction of the heat onto a few tiles.

7 Conclusion, discussion & outlook

7.1 Conclusion

As defined in 1.6, the key objective of this thesis was to *assess the effects of finite plasma beta on the magnetic topology of the edge islands and the resulting changes in the heat load distribution on plasma facing components.* Towards this end, the following contributions were made to achieve this objective:

- Finite-beta equilibria were simulated with the HINT code for a systematic study of pressure profiles up to a central beta of 5% and a volume-averaged beta of 2.5% (chapter 3, chapter 6).
- Based on the simulated equilibria, the heat-loads on the plasma-facing components of W7-X were estimated using the W7-X web service's field-line tracer and a new synthetic camera for accurate interpretation of the field-line diffusion results (chapter 3, chapter 6)
- The simulated changes in the edge magnetic field were measured during the first campaign using a newly developed reciprocating magnetic probe and compared with the predictions from HINT (chapter 4, chapter 5).
- The predicted stability of heat-loads in the standard magnetic configuration was experimentally verified using a statistical analysis across multiple discharges (chapter 5, 6).
- The pressure distributions of the HINT equilibria were compared with pressure profile measurements derived from Thomson Scattering and XICS observations in the core, as well as Helium-beam and reciprocating probe measurements in the edge (chapter 4, chapter 5).
- In addition to comparison with HINT measurements, profile diagnostics were mapped into an island-aware magnetic surface coordinate via a machine-learning algorithm and compared against each other (chapter 3, chapter 5).

7.2 Discussion of results

W7-X will be facing significant new challenges in its first steady-state campaign as discharge duration and heating power increase. According to field-line diffusion calculations, the standard

configuration is significantly better-suited for these operational scenarios than its high- and low-iota counterparts. In high-iota configuration, the primary concern are the leading-edge loads on the heat-shield tiles in the outboard triangular plane, which are directly related to a nearly complete stochastization of the edge islands in high-beta scenarios. In the current time-frame, the geometry of these tiles can still be modified to move these leading edges out of the incoming plasma flow. In the low-iota case, the primary concern is a transition from a divertor- to a limiter-configuration due to the loss of the divertor islands around $\beta_{\mathrm{ax}} = 5\%$ (although the islands should return at higher pressures). This limiter-like configuration imposes significant heat-loads onto the divertor baffle regions, and should either be transitioned through of avoided through modification of the magnetic geometry.

It was shown in chapter 6 of this thesis, that the standard configuration shows a significantly higher degree of stability against plasma-beta driven effects than its high- and low-iota peers. While all three configurations exhibited the appearance of baffle loads in high-beta scenarios, the other two configurations showed additional detrimental effects on top. Both low- and high-iota configuration experience a loss of their nested magnetic islands due to different physical mechanisms. Due to interactions between the growing magnetic islands and the chaotic outer magnetic domain, in high-iota configuration, the island region is fully taken over by stochastization, which directs substantial amounts of heat on small sections of the heat-shield near the triangular plane. In low-iota configuration, the vacuum magnetic Fourier component establishing the edge islands was found to be cancelled out at high plasma beta, resulting in a substantial reduction in island width and an eventual transition to a limiter-like configuration, which changed the strike-line pattern from a line-like to a spot-like shape with substantially smaller area.

The standard configuration's relative stability could be confirmed in chapter 5, where a statistical analysis of multiple discharges confirmed a very weak variation of the strike-line with plasma beta at achieved moderate-beta plasmas, completely dominated by the shifts induced by the toroidal plasma current. Furthermore, radial magnetic profile measurements were found to roughly agree with the predictions made by the HINT code, which builds confidence in the accuracy of the underlying equilibria for the core-driven changes in the edge magnetic field. However, a final analysis in this area is outstanding and requires a more accurate magnetic probe system.

Measurements with the magnetic probe during the second divertor campaign measured changes in the edge magnetic field in agreement with the predictions with HINT and not in agreement with simpler models purely assuming a toroidal current. These measurements also demonstrated a deviation in the vacuum field profile from the ideal magnetic fields based on CAD coil geometries. This information could be used in the future as a diagnostic to validate models for magnetic-load driven deformations of the main coils.

Potential improvements

Accuracy of the pressure distributions

The 2-degree structure of the pressure profiles used in this thesis has served well in the process of separately analyzing the effects related to central and volume-averaged plasma beta. However, the space of experimental profiles is too constrained to achieve an exact match to the experimental profiles, mostly due to the separate dynamics of the ion- and electron-pressure, which both contribute to the total plasma pressure. Constructing a larger parameter space will be vital in achieving

a proper match between experiment and theory. Similarly, the pressure distributions currently employed in the edge are entirely artificial and are mostly related to HINT's pressure averaging scheme. To achieve a proper match between experiment and simulation in this region, further reduction of the averaging length will be required. However, this length can not be arbitrarily lowered without affecting the stability of the distribution in the plasma core.

Transport model accuracy

HINT relies on a simple field-line following method as a surrogate transport model. Similarly, the field-line diffusion method used to calculate the heat load only gives a simplified view of the transport in the scrape-off layer. Both steps, but especially the latter, would greatly benefit from the inclusion of more sophisticated transport models. Two key physical elements of interest are the parallel transport model and the interaction between plasma and neutral particles as well as impurities. Switching from a convective to a diffusive parallel flow model would lift the current restriction prohibiting counter-streaming flows (due to the particles performing U-turns in the parallel direction) and provide more accurate simulations of the heat-loads in attached conditions. The influence of neutral particles is the key to modeling the physics of attached divertor conditions. Currently, the interaction between equilibrium effects (e.g. stochastization in the edge) and detachment is not fully understood. Combined modeling of these two effects is, however, a key requirement to guarantee safe operation in the finally envisioned high-performance scenarios with up to 5% volume-averaged beta, which will very likely require steady-state detachment.

Configuration space

The work of this thesis was mainly focused on characterizing the standard-, high-, and low-iota configuration. There is, however, a large, mostly unexplored configuration space surrounding these three configurations. Examples include inward- and outward-shifted configurations, intermediate iota configurations to mimic high-current scenarios, and high- and low-mirror configurations. Particularly, there are two operationally relevant configurations missing from this analysis. The first one is the high-mirror configuration, which features - out of all designed configurations - the lowest bootstrap current. The poor suitability of high- and low-iota for high-beta operation and the similarity of the high-mirror to the standard configuration (both feature a $^5/_5$ island divertor) further increase the relevance of this configuration for future high-performance scenarios. The second missing configuration is an intermediate limiter-like configuration between standard and high-iota, in which the rotational transform is lifted just enough to separate the magnetic islands from the divertor plate. This configuration has been, during the past campaign, particularly subject to discussion by research groups focused on studying edge plasma turbulence. Here, the equilibrium calculation should primarily serve to provide an accurate mapping of the plasma edge, which is required to correlate the spatial structure of turbulent dynamics to the magnetic topology.

7.3 Outlook

Through predictive modeling and experimental comparisons, HINT has clearly demonstrated its usefulness in the modeling of high-beta plasmas. A particular strength the code has shown is the ease of coupling to other fusion-related simulation tools such as field-line tracers, as it already gives

the full 3D magnetic field as an output. This strength will be substantially exploited in the near future, with analyses based on equilibria obtained through HINT already being worked on with the plasma- and impurity-transport code EMC3-EIRENE, the wall-erosion and re-deposition code ERO (and potentially its successor ERO 2.0), and various instances of the field-line tracing system for W7-X.

Accuracy of the pressure distributions

There are already ongoing activities to improve the accuracy of equilibrium pressure distributions in the plasma edge. On the parametric side, these activities particularly involve the tuning of the pressure profile's edge component and HINT's pressure averaging length. However, further adjustments will likely be necessary to achieve the desired match. A significant limitation is the resolution of the HINT code, which operates on a uniform cylindrical grid. Increasing the resolution is directly penalized by increases in the code's run-time. This pressure can be alleviated by decoupling the grids used by different sub-systems (particularly for the resolution of the divertor geometry) or by introducing an adaptive grid into the code. The latter in particular is, unfortunately, a substantial investment and could potentially require a nearly complete re-write of the code (as the structure of the grid is intricately coupled to its discretization scheme).

Improving the match of the core pressure profiles primarily mandates the design of a new, higher-dimensional representation space for the plasma profiles. The main challenge here lies in the likely non-linear structure of such a space. A promising approach that might work well in tandem with the already developed mapping approach lies in the application of variational autoencoders (VAEs, [70]) for this purpose. Not only have these models already proven their ability to capture complex but low-dimensional manifolds in computer vision, but their root in Bayesian modeling theory also makes them compatible with the Bayesian forward modeling approaches already popular in diagnostic modeling.

Transport model accuracy

Heat- and particle-transport in the plasma edge has already been the subject of intensive research in the past decades, which has led to the development of multiple edge transport simulation codes. Of particular interest as a replacement for field-line diffusion is the edge transport code EMC3-EIRENE, which is a joint development between many European research agencies, and a proven work-horse of Stellarator research. The main issue in coupling this code to HINT is that EMC3-EIRENE relies on a field-line aligned grid to sample the equilibrium state of its Monte-Carlo simulations. The alignment of this grid with the magnetic surface structure is particularly important to correctly estimate the fluxes across these magnetic surfaces. However, the complex edge topology of W7-X still necessitates a large amount of manual intervention in the grid generation process, which makes an automatic coupling nearly impossible, and limits it to a two-digit number of selected cases. This area would, therefore, greatly benefit from research into fully automatic grid generation for EMC3-EIRENE as well as constraint relaxations on the grid (potentially by using other means to extract fluxes).

Configuration space

Simulations of the high-mirror configuration are already on-going and partially completed, while simulations of the intermediate configuration between the standard- and high-iota-configuration are still pending for the future. Beyond the different vacuum field and VMEC input, there are no major modifications to the simulation pipe-line required for the evaluation of these two configurations. Therefore, results in this area should be provided quickly. Considerably more challenging would be the extension towards configurations that violate the Stellarator symmetry, which would multiply the size of the grid, and also the lower bound on the computation time, by a factor of five (a factor of ten for the field-line diffusion calculations). Studies in this domain would probably be limited to the detailed modeling of a select few runs.

Bibliography

[1] J. Wit, C.M. Straaten, and W.G. MOOK. "Determination of the absolute isotopic ratio of V-SMOW and SLAP". In: *Geostandards Newsletter* 4 (May 2007), pp. 33–36. DOI: 10.1111/j.1751-908X.1980.tb00270.x.

[2] Mohamed A. Abdou. "Tritium Breeding in Fusion Reactors". In: *Nuclear Data for Science and Technology*. Ed. by K. H. Böckhoff. Dordrecht: Springer Netherlands, 1983, pp. 293–312. ISBN: 978-94-009-7099-1.

[3] N. Baluc. "25 - Corrosion issues in thermonuclear fusion reactors and facilities". In: *Nuclear Corrosion Science and Engineering*. Ed. by Damien Féron. Woodhead Publishing Series in Energy. Woodhead Publishing, 2012, pp. 906–938. ISBN: 978-1-84569-765-5. DOI: 10.1533/9780857095343.6.906.

[4] *Statistischer Bericht E IV 4 – j / 16 - Energie- und CO2-Bilanzen Berlin 2016*. Tech. rep. 2019. Amt für Statistik Berlin-Brandenburg, 2019.

[5] R. Paul Drake. *High-Energy-Density Physics*. 2006. ISBN: 978-3-540-29314-9. DOI: 10.1007/3-540-29315-9.

[6] Alireza Bahadori and Hari B. Vuthaluru. "Estimation of performance of steam turbines using a simple predictive tool". In: *Applied Thermal Engineering* 30.13 (2010), pp. 1832–1838. ISSN: 1359-4311. DOI: https://doi.org/10.1016/j.applthermaleng.2010.04.017.

[7] L Jr Spitzer. *U.S. Atomic Energy Commission Report No. NYO-993*. Tech. rep. July 1951.

[8] "Stability and Heating of Plasmas in Toroidal Chambers." In: *Proceedings of the 2nd Geneva Conference on the Peaceful Uses of Atomic Energy* (1961).

[9] M. Lehnen et al. "Disruptions in ITER and strategies for their control and mitigation". In: *Journal of Nuclear Materials* 463 (2015). PLASMA-SURFACE INTERACTIONS 21, pp. 39–48. ISSN: 0022-3115. DOI: https://doi.org/10.1016/j.jnucmat.2014.10.075.

[10] John David Jackson. *Klassische Elektrodynamik*. Third. De Gruyter, 2002, p. 779. ISBN: 3-11-016502-3.

[11] Oliver Schmitz et al. "Stable heat and particle flux detachment with efficient particle exhaust in the island divertor of Wendelstein 7-X". In: *Nuclear Fusion* (2020). URL: http://iopscience.iop.org/10.1088/1741-4326/abb51e.

[12] T. Sunn Pedersen et al. "First divertor physics studies in Wendelstein 7-X". In: *Nuclear Fusion* 59.9 (July 2019), p. 096014. DOI: 10.1088/1741-4326/ab280f.

[13] A.V. Bazaeva et al. "Magnetic configuration of a poloidal divertor tokamak". In: *Nuclear Fusion* 20.1 (Jan. 1980), pp. 83–90. DOI: 10.1088/0029-5515/20/1/009.

[14] H. Vernickel et al. "ASDEX upgrade: A poloidal divertor tokamak adapted to reactor requirements". In: *Journal of Nuclear Materials* 128-129 (1984), pp. 71–77. ISSN: 0022-3115. DOI: https://doi.org/10.1016/0022-3115(84)90330-1.

[15] H.Y. Guo et al. "Recent progress on divertor operations in EAST". In: *Journal of Nuclear Materials* 415.1, Supplement (2011). Proceedings of the 19th International Conference on Plasma-Surface Interactions in Controlled Fusion, S369–S374. ISSN: 0022-3115. DOI: https://doi.org/10.1016/j.jnucmat.2010.11.048.

[16] H Renner et al. "Divertor concept for the W7-X stellarator and mode of operation". In: *Plasma Physics and Controlled Fusion* 44.6 (May 2002), pp. 1005–1019. DOI: 10.1088/0741-3335/44/6/325.

[17] N Ohyabu et al. "The Large Helical Device (LHD) helical divertor". In: *Nuclear Fusion* 34.3 (Mar. 1994), pp. 387–399. DOI: 10.1088/0029-5515/34/3/i07.

[18] A. Bader et al. "HSX as an example of a resilient non-resonant divertor". In: *Physics of Plasmas* 24.3 (2017), p. 032506. DOI: 10.1063/1.4978494.

[19] T. Sunn Pedersen et al. "Confirmation of the topology of the Wendelstein 7-X magnetic field to better than 1:100". In: *Nature Communications* 7.1 (Nov. 2016). DOI: 10.1038/ncomms13493.

[20] T. Andreeva, J. Kisslinger, and H. Wobig. "Characteristics of main configurations of Wendelstein 7-X". In: *Problems of Atomic Science and Technology. Series: Plasma Physics* 35 (7 2002), pp. 45–47.

[21] E Strumberger. "Finite- magnetic field line tracing for Helias configurations". In: *Nuclear Fusion* 37.1 (Jan. 1997), pp. 19–27. DOI: 10.1088/0029-5515/37/1/i03.

[22] E. Strumberger. "Stochastic Magnetic Field Structure in the Edge Region of W7-X". In: *Contributions to Plasma Physics* 38.1-2 (1998), pp. 106–111. DOI: 10.1002/ctpp.2150380115.

[23] Y. Suzuki et al. "Three-Dimensional Effects on Stochasticity in Non-Axisymmetric Tori". In: *Contributions to Plasma Physics* 50.6-7 (2010), pp. 576–581. DOI: 10.1002/ctpp.200900058.

[24] T. Hayashi et al. "Formation and 'self-healing' of magnetic islands in finite-beta Helias equilibria". In: *Physics of Plasmas* 1.10 (1994), pp. 3262–3268. DOI: 10.1063/1.870478.

[25] M Drevlak, D Monticello, and A Reiman. "PIES free boundary stellarator equilibria with improved initial conditions". In: *Nuclear Fusion* 45.7 (July 2005), pp. 731–740. DOI: 10.1088/0029-5515/45/7/022.

[26] Y Suzuki and J Geiger. "Impact of nonlinear 3D equilibrium response on edge topology and divertor heat load in Wendelstein 7-X". In: *Plasma Physics and Controlled Fusion* 58.6 (May 2016), p. 064004. DOI: 10.1088/0741-3335/58/6/064004.

[27] Hauke Hölbe. "Control of the magnetic topology and plasma exhaust in the edge region of Wendelstein 7-X: A numerical study". PhD thesis. Ernst-Moritz-Arndt-Universität Greifswald, 2015.

[28] Yu Gao et al. "Effects of toroidal plasma current on divertor power depositions on Wendelstein 7-X". In: *Nuclear Fusion* 59.10 (Aug. 2019), p. 106015. DOI: 10.1088/1741-4326/ab32c2.

[29] H. Grad and H. Rubin. "Hydromagnetic equilibria and force-free fields". In: *Proceeding of the second United Nations International Conference on the Peaceful Uses of Atomic Energy* 31 (1958).

[30] V. Shafranov. "On magnetohydrodynamical equilibrium configurations". In: *Soviet Physics JETP* 6 (1958).

[31] Martin S. Alnæs et al. "The FEniCS Project Version 1.5". In: *Archive of Numerical Software* 3.100 (2015). DOI: 10.11588/ans.2015.100.20553.

[32] Anders Logg, Kent-Andre Mardal, Garth N. Wells, et al. *Automated Solution of Differential Equations by the Finite Element Method*. Springer, 2012. ISBN: 978-3-642-23098-1. DOI: 10.1007/978-3-642-23099-8.

[33] Alexander Knieps. *alexrobomind/gs_solver: Initial release*. 2020. DOI: 10.5281/ZENODO.4099981.

[34] Yasuhiro Suzuki. "Effect of pressure profile on stochasticity of magnetic field in a conventional stellarator". In: *Plasma Physics and Controlled Fusion* 62.10 (Aug. 2020), p. 104001. DOI: 10.1088/1361-6587/ab9a13.

[35] L. L. Lao, S. P. Hirshman, and R. M. Wieland. "Variational moment solutions to the Grad–Shafranov equation". In: *The Physics of Fluids* 24.8 (1981), pp. 1431–1440. DOI: 10.1063/1.863562.

[36] M Drevlak, D Monticello, and A Reiman. "PIES free boundary stellarator equilibria with improved initial conditions". In: *Nuclear Fusion* 45.7 (July 2005), pp. 731–740. DOI: 10.1088/0029-5515/45/7/022.

[37] V.D. Shafranov and L.E. Zakharov. "Use of the virtual-casing principle in calculating the containing magnetic field in toroidal plasma systems". In: *Nuclear Fusion* 12.5 (Sept. 1972), pp. 599–601. DOI: 10.1088/0029-5515/12/5/009.

[38] Yasuhiro Suzuki. "HINT modeling of three-dimensional tokamaks with resonant magnetic perturbation". In: *Plasma Physics and Controlled Fusion* 59.5 (Mar. 2017), p. 054008. DOI: 10.1088/1361-6587/aa5adc.

[39] Yasuhiro Suzuki et al. "Development and application of HINT2 to helical system plasmas". In: *Nuclear Fusion* 46.11 (Sept. 2006), pp. L19–L24. DOI: 10.1088/0029-5515/46/11/l01.

[40] Sergey Bozhenkov et al. "Service oriented architecture for scientific analysis at W7-X. An example of a field line tracer". In: *Fusion Engineering and Design* 88 (2013).

[41] Vinod Nair and G E Hinton profile. "Rectified linear units improve restricted boltzmann machines". In: *ICML'10: Proceedings of the 27th International Conference on International Conference on Machine Learning*. 2010, pp. 807–814. DOI: 10.5555/3104322.3104425.

[42] Bing Xu et al. *Empirical Evaluation of Rectified Activations in Convolutional Network*. 2015. arXiv: 1505.00853 [cs.LG]. URL: https://arxiv.org/abs/1505.00853.

[43] Martín Abadi et al. *TensorFlow: Large-Scale Machine Learning on Heterogeneous Distributed Systems*. 2016. arXiv: 1603.04467 [cs.DC].

[44] Diederik P. Kingma and Jimmy Ba. *Adam: A Method for Stochastic Optimization*. 2017. arXiv: 1412.6980 [cs.LG].

[45] Takuya Akiba et al. *Optuna: A Next-generation Hyperparameter Optimization Framework*. 2019. arXiv: 1907.10902 [cs.LG].

[46] James Bergstra et al. "Algorithms for Hyper-Parameter Optimization". In: *Advances in Neural Information Processing Systems*. Dec. 2011.

[47] Liam Li et al. *A System for Massively Parallel Hyperparameter Tuning*. 2020. arXiv: 1810.05934 [cs.LG].

[48] S.A. Bozhenkov et al. "The Thomson scattering diagnostic at Wendelstein 7-X and its performance in the first operation phase". In: *Journal of Instrumentation* 12.10 (Oct. 2017), P10004–P10004. DOI: 10.1088/1748-0221/12/10/p10004.

[49] E. Pasch et al. "The Thomson scattering system at Wendelstein 7-X". In: *Review of Scientific Instruments* 87.11 (2016), 11E729. DOI: 10.1063/1.4962248.

[50] E.R. Scott et al. "Demonstration of an absolute Rayleigh scattering spectral calibration on the W7-X Thomson scattering system". In: *Journal of Instrumentation* 14.10 (Oct. 2019), pp. C10033–C10033. DOI: 10.1088/1748-0221/14/10/c10033.

[51] N A Pablant et al. "Measurement of core plasma temperature and rotation on W7-X made available by the x-ray imaging crystal spectrometer (XICS)". In: *Invited papers to be published in a special issue of Plasma Physics and Controlled Fusion* (July 2014).

[52] A. Langenberg et al. "Argon impurity transport studies at Wendelstein 7-X using x-ray imaging spectrometer measurements". In: *Nuclear Fusion* 57.8 (June 2017), p. 086013. DOI: 10.1088/1741-4326/aa70f4.

[53] T. Barbui et al. "The He/Ne beam diagnostic for line-ratio spectroscopy in the island divertor of Wendelstein 7-X". In: *Journal of Instrumentation* (July 2019). DOI: 10.1088/1748-0221/14/07/c07014.

[54] M. Endler et al. "Engineering design for the magnetic diagnostics of Wendelstein 7-X". In: *Fusion Engineering and Design* 100 (2015), pp. 468–494. ISSN: 0920-3796. DOI: 10.1016/j.fusengdes.2015.07.020.

[55] K. Rahbarnia et al. "Diamagnetic energy measurement during the first operational phase at the Wendelstein 7-X stellarator". In: *Nuclear Fusion* 58.9 (July 2018), p. 096010. DOI: 10.1088/1741-4326/aacab0.

[56] Marcin Jakubowski et al. "Infrared imaging systems for wall protection in the W7-X stellarator (invited)". In: *Review of Scientific Instruments* 89.10 (2018), 10E116. DOI: 10.1063/1.5038634.

[57] B. Sieglin et al. "Real time capable infrared thermography for ASDEX Upgrade". In: *Review of Scientific Instruments* 86.11 (2015), p. 113502. DOI: 10.1063/1.4935580.

[58] Carsten Killer et al. "Characterization of the W7-X scrape-off layer using reciprocating probes". In: *Nuclear Fusion* 59.8 (June 2019), p. 086013. DOI: 10.1088/1741-4326/ab2272.

[59] Dirk Nicolai et al. "A multi-purpose manipulator system for W7-X as user facility for plasma edge investigation". In: *Fusion Engineering and Design* 123 (Nov. 2017), pp. 960–964. DOI: 10.1016/j.fusengdes.2017.03.013.

[60] G. Satheeswaran et al. "A PCS7-based control and safety system for operation of the W7-X Multi-Purpose Manipulator facility". In: *Fusion Engineering and Design* 123 (Nov. 2017), pp. 699–702. DOI: 10.1016/j.fusengdes.2017.05.125.

[61] P. Drews et al. "Operation of probe heads on the Multi-Purpose-Manipulator at W7-X in OP 1.2a". In: *Fusion Engineering and Design* 146 (2019). SI:SOFT-30, pp. 2353–2355. ISSN: 0920-3796. DOI: https://doi.org/10.1016/j.fusengdes.2019.03.188.

[62] P. Drews et al. "Edge plasma measurements on the OP 1.2a divertor plasmas at W7-X using the combined probe". In: *Nuclear Materials and Energy* 19 (May 2019), pp. 179–183. DOI: 10.1016/j.nme.2019.02.012.

[63] A. Knieps et al. "Design and characteristics of a low-frequency magnetic probe for magnetic profile measurements at Wendelstein 7-X". In: *Review of Scientific Instruments* 91.7 (2020), p. 073506. DOI: 10.1063/5.0002193.

[64] Thomas W. Fredian and Joshua A. Stillerman. "MDSplus. Current developments and future directions". In: *Fusion Engineering and Design* 60.3 (2002), pp. 229–233. ISSN: 0920-3796. DOI: 10.1016/S0920-3796(02)00013-3.

[65] T. Fredian, J. Stillerman, and G. Manduchi. "MDSplus extensions for long pulse experiments". In: *Fusion Engineering and Design* 83.2 (2008). Proceedings of the 6th IAEA Technical Meeting on Control, Data Acquisition, and Remote Participation for Fusion Research, pp. 317–320. ISSN: 0920-3796. DOI: 10.1016/j.fusengdes.2007.08.022.

[66] Samuel A. Lazerson et al. "Tuning of the rotational transform in Wendelstein 7-X". In: *Nuclear Fusion* 59.12 (Sept. 2019), p. 126004. DOI: 10.1088/1741-4326/ab3df0.

[67] H. Niemann et al. "Large wetted areas of divertor power loads at Wendelstein 7-X". In: *Nuclear Fusion* 60.8 (July 2020), p. 084003. DOI: 10.1088/1741-4326/ab937a.

[68] E Strumberger et al. *First Survey of Finite-beta Magnetic Fields of W7-X*. Tech. rep. Max-Planck-Institut für Plasmaphysik, Germany, 1997. URL: http://hdl.handle.net/11858/00-001M-0000-0028-CFB7-1.

[69] K C Hammond et al. "Drift effects on W7-X divertor heat and particle fluxes". In: *Plasma Physics and Controlled Fusion* 61.12 (Oct. 2019), p. 125001. DOI: 10.1088/1361-6587/ab4825.

[70] Diederik P. Kingma and Max Welling. "An Introduction to Variational Autoencoders". In: *Foundations and Trends® in Machine Learning* 12.4 (2019), pp. 307–392. ISSN: 1935-8237. DOI: 10.1561/2200000056.

Acknowledgements

First and foremost, I would like to express my heartfelt gratitude to my PhD supervisor, Prof. Dr. Yunfeng Liang, for constantly being available for me when I had questions concerning research methodology and academic questions. His guidance was immeasurably valuable to the scientific and academic work I performed throughout my thesis project, and I would have gotten nowhere near the point I am at not without his support. I would also like Prof. Dr. Georg Pretzler for the engaging discussions and for putting up with my sometimes rather poor organiziational skills.

Many thanks go to Dr. Yasuhiro Suzuki for introducing me to and laborously maintaining the HINT code, keeping it in a shape beyond what I thought possible in Fortran. Likewise, I would like to thank Joachim Geiger for always helping me sorting out various issues to MHD equilibria, both in theory and in numerics. This thesis would have come nowhere near its final volume without the constant discussions I enjoy with Dr. Philipp Drews. Likewise, I would also thank him as the lead designer for the combined probe.

For their constant work on the combined probe, the manipulator and the magnetic integrator system, I would like to thank Dr. Shaocheng Liu, Dirk Nicolai, Guruparan Satheeswaran and Norbert Sandri, as well as Dr. Carsten Killer. I would also like to thank Dr. Sergey Bozhenkov and Michael Grahl for bearing with me when I once again enjoyed my personal vendetta with the fieldlinetracing webservices, and Sergey especially for providing convenient access to W7-X diagnostic data with his W7-X diagnostic library.

Special thanks also go to the IR camera team on W7-X (Dr. Marcin Jakubowski, Dr. Peter Drewelow, Dr. Yu Gao, and, especially, Dr. Holger Niemann) who provided to me and assisted me in accessing and interpreting the heat-fluxes calculated from IR camera data. I would also like to thank the teams of the experimental fusion devices which I had the pleasure to perform experiments on during my PhD research time, including the teams of Large Helical Device at the National Institute for Fusion Science (Japan), Wendelstein 7-X at the Institut for Plasma Physics in Greifswald (Germany), and the J-TEXT tokamak at the Huazhong University in Wuhan (China).

Finally, I would like to thank my family for supporting me over the last three years (and also before). A special thank you goes towards my aunt, for being an immovable pillar I could always rely on in the last twelve years.

A Derivation of the full transfer model for the magnetic probe

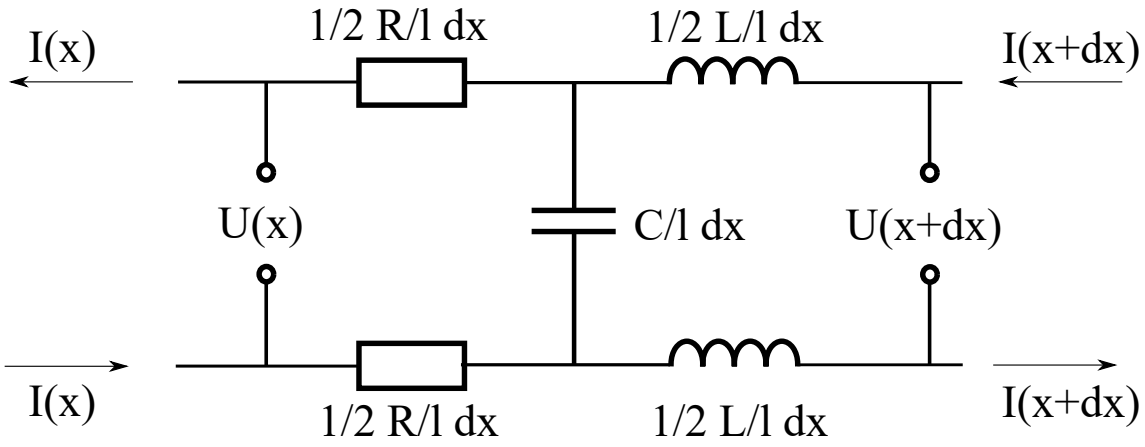

Figure A.1: Schematic of the continuous cable model

Assuming the twisted wire pair to follow a standard differential LCR model, the differential signal propagation equations can be extracted from figure A.1 as:

$$\begin{aligned} \frac{dU}{dx} &= -\frac{R_{\text{cable}}}{l} I(x) - \frac{L_{\text{cable}}}{l} \frac{d}{dt} I(x) \\ \frac{dI}{dx} &= -\frac{C_{\text{cable}}}{l} \frac{d}{dt} U(x) \end{aligned} \tag{A.1}$$

Using a propagating wave Ansatz $U, I(x,t) = U, I_{\pm} \exp(i(\omega t \pm kx))$ yields the wave dispersion relation

$$
\begin{aligned}
\pm ikU_{\pm} &= -\frac{R_{\text{cable}}}{l} I_{\pm} - i\omega \frac{L_{\text{cable}}}{l} I_{\pm} \\
\pm ikI_{\pm} &= -i\omega \frac{C_{\text{cable}}}{l} U_{\pm} \\
&\Rightarrow \\
-k^2 &= i\omega \frac{R_{\text{cable}}}{l} \frac{C_{\text{cable}}}{l} - \omega^2 \frac{L_{\text{cable}}}{l} \frac{C_{\text{cable}}}{l} \\
&\Rightarrow \\
k(\omega) &= \sqrt{\omega^2 \frac{L_{\text{cable}} C_{\text{cable}}}{l^2} - i\omega \frac{R_{\text{cable}} C_{\text{cable}}}{l^2}}
\end{aligned}
\tag{A.2}
$$

Assuming that the coil is connected at $x = 0$ and the integrator input at $x = l$, one gets:

$$
\begin{aligned}
\tilde{U}_{\text{coil}} &= U_+ + U_- \\
\tilde{U}_{\text{input}} &= U_+ \exp(ikl) + U_- \exp(-ikl) \\
\tilde{I}_{\text{coil}} &= \frac{\omega}{k} \frac{C_{\text{cable}}}{l} (U_- - U_+) \\
&= Z(\omega)^{-1} (U_- - U_+) \\
\tilde{I}_{\text{input}} &= Z(\omega)^{-1} (\exp(-ikl) U_- - \exp(ikl) U_+)
\end{aligned}
$$

with the frequency-dependent cable impedance

$$
\begin{aligned}
Z(\omega) &= \left(\frac{\omega}{k} \frac{C_{\text{cable}}}{l} \right)^{-1} \\
&= \sqrt{\frac{L_{\text{cable}}}{C_{\text{cable}}} - \frac{i}{\omega} \frac{R_{\text{cable}}}{C_{\text{cable}}}}
\end{aligned}
$$

The coil follows a linear differential equation and can be subjected to the same rotating wave Ansatz

$$
\begin{aligned}
V_{\text{coil}} &= \frac{d}{dt} \left[A_{\text{coil}} B - L_{\text{coil}} I_{\text{coil}} \right] - R_{\text{coil}} I_{\text{coil}} \\
\tilde{V}_{\text{coil}} &= i\omega \left(A_{\text{coil}} \tilde{B} - L_{\text{coil}} \tilde{I}_{\text{coil}} \right) - R_{\text{coil}} \tilde{I}_{\text{coil}} \\
&= i\omega A_{\text{coil}} \tilde{B} - (R_{\text{coil}} + i\omega L_{\text{coil}}) \tilde{I}_{\text{coil}}
\end{aligned}
$$

while the integrator has a fixed input impedance of $R_{\text{meas}} = 10\,\text{k}\Omega$, along with an optional capacitor C_{meas} used in characterization to determine the coil inductance.

$$
\tilde{I}_{\text{input}} = \left(R_{\text{meas}}^{-1} + i\omega C_{\text{meas}} \right) \tilde{U}_{\text{input}}
$$

Expanding for $U_{\pm}$ yields:

$$
\begin{aligned}
U_+ + U_- &= i\omega A_{\text{coil}} \tilde{B} - (R_{\text{coil}} + i\omega L_{\text{coil}}) \frac{U_- - U_+}{Z} \\
\frac{\exp(-ikl) U_- - \exp(ikl) U_+}{Z} &= \left(R_{\text{meas}}^{-1} + i\omega C_{\text{meas}} \right) \left[U_+ \exp(ikl) + U_- \exp(-ikl) \right]
\end{aligned}
$$

$$U_- = \frac{1 + Z\left(R_{\text{meas}}^{-1} + i\omega C_{\text{meas}}\right)}{1 - Z\left(R_{\text{meas}}^{-1} + i\omega C_{\text{meas}}\right)} \exp\left(2ikl\right) U_+$$

Let $\kappa = Z\left(R_{\text{meas}}^{-1} + i\omega C_{\text{meas}}\right)$ and $\lambda = Z^{-1}\left(R_{\text{coil}} + i\omega L_{\text{coil}}\right)$ be the normalized dimensionless output- and input-impedances. Then

$$\begin{aligned}
\left[1 + \frac{1+\kappa}{1-\kappa}\exp\left(2ikl\right)\right] U_+ &= i\omega A_{\text{coil}}\tilde{B} + \lambda\left[1 - \frac{1+\kappa}{1-\kappa}\right] U_+ \\
&\Rightarrow \\
\left[1 - \lambda + \frac{1+\kappa}{1-\kappa}\left(\lambda + \exp\left(2ikl\right)\right)\right] U_+ &= i\omega A_{\text{coil}}\tilde{B} \\
U_+ &= \frac{1}{1 - \lambda + \frac{1+\kappa}{1-\kappa}\left(\lambda + \exp\left(2ikl\right)\right)} i\omega A\tilde{B} \\
U_- &= \frac{\frac{1+\kappa}{1-\kappa}\exp\left(2ikl\right)}{1 - \lambda + \frac{1+\kappa}{1-\kappa}\left(\lambda + \exp\left(2ikl\right)\right)} i\omega A\tilde{B}
\end{aligned}$$

This then gives an input voltage on the integrator of

$$\begin{aligned}
\tilde{U}_{\text{input}} &= \frac{\left(1 + \frac{1+\kappa}{1-\kappa}\right)\exp\left(ikl\right)}{1 - \lambda + \frac{1+\kappa}{1-\kappa}\left(\lambda + \exp\left(2ikl\right)\right)} i\omega A_{\text{coil}}\tilde{B} \\
&= \frac{2\exp\left(ikl\right)}{\left(1-\lambda\right)\left(1-\kappa\right) + \left(1+\kappa\right)\left(\lambda + \exp\left(2ikl\right)\right)} i\omega A_{\text{coil}}\tilde{B}
\end{aligned} \tag{A.3}$$

In the case of $kl \approx 0$ (neglecting forward and backward phase delays due to the cable), one can simplify this expression to:

$$\begin{aligned}
\tilde{U}_{\text{input}} &\approx \frac{2}{\left(1-\lambda\right)\left(1-\kappa\right) + \left(1+\kappa\right)\left(\lambda + 1\right)} i\omega A_{\text{coil}}\tilde{B} \\
&= \frac{i\omega A_{\text{coil}}\tilde{B}}{1 + \lambda\kappa} \\
&= \frac{i\omega A_{\text{coil}}\tilde{B}}{1 + \frac{R_{\text{coil}}}{R_{\text{meas}}} + i\omega\left(R_{\text{coil}}C_{\text{meas}} + \frac{L_{\text{coil}}}{R_{\text{meas}}}\right) - \omega^2 L_{\text{coil}}C_{\text{meas}}}
\end{aligned} \tag{A.4}$$

B Running HINT: A short manual

B.1 Compiling and installing HINT

HINT is an MPI-based FORTRAN code. At this thesis's time of writing, the code is maintained in a central repository, and the maintainer should be directly contacted to gain access to this repository (currently the maintainer of the code is Dr. Yasuhiro Suzuki). In the newest versions, HINT is distributed with a CMake file, which will automatically detect and set up MPI and optionally OpenMP. CMake does not allow in-source builds (where the top-level source directory and the build directory are identical), but building in a subdirectory of the source dir is permitted. CMake builds have two separate phases: A configuration step, where CMake generates build files for a third party build tool (supported targets include "make", "ninja" and - on Windows - Visual Studio, which can also build cmake projects by itself), followed by an independent build step in the external build tool. If one just wishes to build HINT, the standard command line is:

```
cmake {path to HINT source}
make -j {number of build processes}
```

If a specific FORTRAN compiler should be used, one can select the preferred compiler with the FC environment variable

```
FC=ifort cmake {path to HINT source}
make -j {number of build processes}
```

If one wishes to install HINT, one can simply run

```
make install
```

after the build process. On most machines, this will fail as installing into system-level program directories requires administrator rights. One can also specify a custom install directory by setting the CMAKE_INSTALL_PREFIX option of CMake using the -D flag.

```
cmake -DCMAKE_INSTALL_PREFIX={path to target directory} ...
  {path to HINT source}
make -j {number of build processes}
make install
```

B.2 Required inputs & input formats

HINT has two run modes, which require different inputs:

- The *follow* mode is intended to continue a previous run, optionally with new parameters. It requires a vacuum magnetic field, a machine geometry description and a snapshot of a previous run to initialize the equilibrium field and the pressure distribution from.
- The *initial* mode is intended if one wishes to start a run from scratch. This mode requires a vacuum magnetic field, a machine geometry description and an initial estimate for the vacuum magnetic flux surfaces.

HINT supports reading input data in multiple formats, but all formats contain essentially the same data. I describe here only the data layout of the netCDF classes. The data layout of the other formats can be easily gleamed from the source code.

- All input files have the variables *rminb, rmaxb, zminb, zmaxb* parametrizing the ranges of the R (major radius) and z axes. Additionally, the variable *mtor* holds the toroidal symmetry descriptions. In the netCDF input format, the number of elements per direction is inferred from the dimensions of the field variables. All variables are, in netCDF, stored in ϕ, z, R order. Note that in the FORTRAN code itself, the data are handled in R, z, ϕ order. This is because FORTRAN stores data in column major order, while the rest of the world uses a row-major format. All grid variables (coordinate ranges, toroidal symemtry, grid size) of the input files must be exactly identical to the grid parameters chosen to execute the run. This also implies that a different grid also requires different input files. NetCDF also supports variables named identically do dimensions, which contain the dimension values. HINT does not require these variables, and but writing them into the file is needed to use visualization programs (e.g. Panoply) to visualize its contents. **Even if present, HINT does not read these files and assumes equidistant coordinate grids described by the files above**.
- The vacuum field files additionally contain three variables, *Bv_R, Bv_Z* and *Bv_phi*, which hold the R, z and ϕ components of the magnetic field, unnormalized.
- Machine geometry files additionally contain an integer-type variable *limiter*. This variable must have the same dimensions as all other field variables, and contains a voxel-based description of the machine geometry. It should be set to 1 in every voxel occupied by machine parts, and 0 everywhere else.
- Flux estimate files should additionally hold a variable *flux*, which holds a number between in the $[0, 1]$ range describing the normalized magnetic flux.

B.3 Configuration

The parametrization of the requested run is passed into the code in the form of FORTRAN namelist inputs on the standard input (*stdin*) of the HINT processes. This information must be fed to each worker process individually, and must be globally identical. Individual sections may be left out, and individual variables may be left out or re-ordered within the same namelist section, **but the**

order of individual namelist sections may not be changed. Passing in sections in the wrong order will cause the input pipeline to drop / ignore some sections and the code being configured incorrectly. Lines starting with *!* are ignored by the reader and can be used to comment lines.

```
!----------------------------------------
! set MPI process numbers along R, Z, phi
!----------------------------------------
&mpi_inp1
  iprocs = 2,  ! along R idrection
  jprocs = 4,  ! along Z direction
  kprocs = 16, ! along phi direction
&end
```

The first section specifies the distribution of the grid among the MPI nodes. This distribution must satisfy iprocs $\cdot$ jprocs $\cdot$ kprocs $= n$ with n being the number of MPI processes assigned to the parallel task. If the code is run sequentially (single node, not recommended due to the high resource usage), $n = 1$. The grid size along each dimension is not required to be a multiple of this number, HINT supports creating balanced uneven grid partitions. **However, not all grid partitions executed successfully**. In some parallel grid configurations, the code diverged on the second macrocycle and crashed due to numerical explosion. A closer examination of the magnetic field before the crash revealed block-like patterns aligned with the partition boundaries. Therefore, it is likely that one of the parallel exchanges routines misbehaves for certain parallelization setups. However, even after multiple thorough multi-person reviews of the related code sections show no possible scenario which might allow this to happen. In principle, this could also relate to a bug in the underlying MPI implementation, but this is itself also highly unlikely.

```
&nlinp1
  !-----------------------------------------------------
  ! "initial": calculation set up from vacuum field
  ! "follow" : following up job
  !-----------------------------------------------------
  run_mode = 'initial',

  !-------------------------------------------------------------
  ! "file": normalized toroidal flux,
  !   s, is read from the file
  ! "calc": s is claulated from the pressure
  !   distribution
  !-------------------------------------------------------------
  flx_type = 'file',

  !-----------------------------------
  ! lresetp: redistribute the pressure
  !-----------------------------------
  lresetp  = .true.,
```

```
  p_type   = 'parabolic',
  j_type   = 'power_series',
  lfile = .true.
&end
```

This section specifies some general setup parameters for the code. The *run_mode* setting is used to distinguish between an initial and follow-up run as mentioned above. This mainly concerns the source of the initial equilibrium field. Note that the vacuum field is also required in a follow-up run, as the code calculates some additional information based on that field. The *flx_type* setting specifies how the magnetic flux, which is used to set the pressure profile from the configuration, should be obtained. *file* mandates the flux to be read from a specified magnetic flux file, while *calc* instrHowever, sucts the code to calculate the magnetic flux values of the isobaric contours of the pressure field, and use those surface as flux surfaces. Note that the *calc* setting only works with *follow*-type runs, as *initial*-type runs have no pressure distribution specified at this stage.

The settings *p_type* and *j_type* determine the shape of pressure- and current-profile to be used. Supported values are:

- *linear*: Interpolate the profile shape from s and p/j values specified as input arrays. **The s coordinates of the profile have to be equi-distant. Otherwise the interpolation will be performed incorrectly**
- *parabolic* (only pressure profile): The pressure profile is of the shape $p(s) \propto c_1 + (1 - c_1) \cdot (1 - s^{c_3})^{c_2}$. Using $c_2 < 1$ or $c_3 < 1$ is not recommended. This will create square-root-like or inverse profiles, which have infinite gradient near $s = 0$ or $s = 1$.
- *power_series*: Use a polynomial in s. Up to 20 polynomial coefficients are supported.

```
!------------------------
! set control parameters
!------------------------
&nlinp2
  !---------------------------------------------------------------------
  ! beta:   toroidal beta value on axis
  ! bt0:    toroidal magnetic field to prescribe the beta
  ! am0:    polynominal coefficients to prescribe the
  !   pressure profile
  ! nprofp: # of support points in pressure profile
  ! profp:  pressure profile
  ! nstep:  step number of overall loops
  ! npchg:  step number to rump up the beta
  ! nsvae:  interval to save the magnetic field
  !   and other equilibrium fields
  ! npset:  interval to redistribute the pressure
  !---------------------------------------------------------------------
  beta   = 0.05,
```

```
  !---- 'parabolic'-type pressure profile ----
  am0    = 0.02, 1.00, 1.00,
  !---- 'linear'-type pressure profile ----
  ! nprofp = 5,
  ! profp  = 5.0, 4.0, 3.0, 2.0, 1.0,
  ! torfp  = 0.0, 0.25, 0.5, 0.75, 1.0,
  nstep  = 80,
  npchg  = 1,
  nsave  = 5,
  npset  = 10,
&end
```

This section describes the requested profiles, as well as the timing behavior of the data writeout.

- *beta*: This value holds the target on-axis plasma beta.
- *am0*: If the pressure profile type is *parabolic*, this variable holds the coefficients c_1, c_2 and c_3
- *nprofp, torfp, profp*: If the pressure profile is *linear*, these three variable hold respectively the no. of interpolation points, their s (x) coordinates and the pressure (y) values on the interpolation points
- *nstep*: This number describes the total no. of macrocycles (Step A, Step B) iterations, which the code should perform.
- *npchg*: HINT supports a "slow-start" protocol for ramping up the pressure. If *npchg* is set to a value larger than one, the first k iterations (starting at $k = 1$) will have the on-axis beta target $\beta_{\text{intermediate}} = \frac{\beta_{\text{ax}}}{1000} \cdot 1000^{\frac{k}{\text{npchg}}}$.
- *nsave*: No. of macrocycles to perform between writing out output snapshots.
- *npset*: No. of macrocycles after which the pressure distribution is modified by first calculating the magnetic flux surfaces from the pressure surfaces, and then re-creating the pressure distribution according to the specified pressure profile. This process is repeated every *npset* macrocycles.

```
&nlinp3
!-----------------------------------------------
! nr:    grid number along R
! nz:    grid number along Z
! ntor:  grid number along phi
! rminb: minimum R of the computational domain
! rmaxb: maximum R of the computational domain
! zminb: minimum Z of the computational domain
! zmaxb: maximum Z of the computational domain
! mtor:  toroidal field period
!-----------------------------------------------
  nr     =  256,
```

```
  nz     =  256,
  ntor   =  128,
  rminb  =  4.0,
  rmaxb  =  7.0,
  zminb  = -1.5,
  zmaxb  =  1.5,
  mtor   =  5,
&end
```

This section describes the coordinate distribution of the grid. The computational domain specified here must match the structure of the input files.

```
&nlinp4
  rstart =  5.9,
  zstart =  0.3
&end
```

This section holds the starting values for the magnetic axis search. If the code is working properly, these settings don't have to be very accurate. The points should, however, lie on a flux surface that surrounds the magnetic axis. Preferably, this surface should have $\iota \neq 1$, as the axis search might otherwise become a bit unstable.

```
&nlinp5
&end
```

Pending

```
!---------------------------------
! set control parameters in step-A
!---------------------------------
&stepa_inp1
  !-------------------------------------------------------------
  ! h_in:  step size of the Runge-Kutta integrator
  !   for field line tracing
  ! lc_in: length of field line tracing
  !-------------------------------------------------------------
  h_in  =  1.0E-02,
  lc_in =  1.0E+01,
&end
!------
```

This section controls the behavior of the *Step A* (field-line averaging) part of the code. The *h_in* parameter controls the step-size of the field-line tracing, which sets both the step-size of the Runge-Kutta integrator of the magnetic field and the step-size of the averaging process itself. The *lc_in* parameter controls the distance along which the field-line is followed during the averaging process.

```
&stepb_inp1
  !-------------------------------------------------------
```

```
  ! lhistoryb: switch to write debugging information
  ! nstepb:    step number to evole MHD equations
  ! nrefb:     interval to save refrences for smoothing
  ! nsmoothb:   interval to apply smoothing filter
  ! nenergyb:  interval to caluclate debugging information
  ! dt_b:      time step to evole MHD equations
  ! eta0:      resistivity in the plasma
  ! eta1:      resistivity in the vacuum
  ! nu1:       viscosity
  !-------------------------------------------------------
  lhistoryb = .true.,
  nstepb    = 1000,
  nrefb     = 1000,
  nsmoothb  = 1,
  nenergyb  = 100,
  dt_b      = 1.0E-03,
  eta0      = 1.0E-03,
  eta_diff  = 1.0E-00,
  ! eta1      = 1.0E-08,
  nu1       = 1.0E-08
  ! kappa_divb = 1.0E-03
&end
```

This section controls the behavior of the *Step B* (magnetic relaxation) part of HINT.

- *lhistoryb* is a boolean switch that enables the write-out of a diagnostic file in CSV (comma-separated-value) format, which contains information about the changes in magnetic field, flow velocity as well as a large set of energy-like quadratic functional values. These values are extremely usedful for judging whether the code has converged. I would therefore recommend them to be written out at all times.
- *nstepb* controls the total number of relaxation iterations that are performed in the *Step B* part of each macrocycle.
- *nrefb* and *nsmoothb* together control an auxiliary smoothing system that stabilized the computation of the magnetic field. The smoother updates the magnetic field as $B \leftarrow B + B_{\text{corr}}$ every *nsmoothb*'th iteration and the reference field $B_{\text{corr}} \leftarrow \Delta B$ (vector Laplacian) every *nrefb*'th iteration.
- *dt_b* is the time-step size assumed for the MHD equations' explicit integrator in the magnetic relaxation process
- *eta_0* is the artificial resistivity assumed for the magnetic relaxation
- *nu_1* is the artificial viscosity used to dampen initial oscillations in the flow. This is neccessary as initially the force balance condition is strongly violated, and therefore strong flows are generated. This term dampens these flow oscillations and speeds up convergence against equilibrium (note that it is required not just for convergence speed, but also stabilization)

- *kappa_divb* is a magnetic stabilization term used in the magnetic relaxation process to eliminate magnetic monopoles. It is set by default to $\kappa_{\nabla \cdot B} = 10^{-3}$.

```
&fopen_stepb
  historyb_file = 'testrun.historyb'
&end
```

This section controls the filename of the history CSV file mentioned above. If *lhistoryb* is not set to true, this section can be ommitted.

```
&fopen
  vac_file = '../../../shared/w7x/op12-standard-cw1cm.vacfile.nc',
  flx_file = '../../../shared/w7x/vmec-w7x_ref_7-15640562fb7feb4b0411d5da7db381f0df15475a.fluxfile.n
  ! mag_file = 'v2test6.1/snapfile.40.nc',
  limiter_file = '../../../shared/w7x/divertor-config-star.limiter.nc'
&end
```

This section tells HINT where to find the input files for vacuum field (*vac_file*), magnetic flux (*flx_file* only required if *flx_type* is set to *file* in section *nlinp1*, which is usually the case in *initial*-type runs), previous run output (*mag_file*, required only for *follow*-type runs) and the machine geometry (*limiter_file*).

B.3.1 Running the code

If the *hint* executable was placed in a location where the operating system can find it (usually this means that the directory *{CMAKE_INSTALL_PREFIX}/bin* must be in the system's *PATH* environment variable), executing the code is simply a matter of running HINT either via MPI:

```
mpiexec -n {Number of cores} hint < {Input control file}
```

If a job scheduler like SLURM is used, the submission command must be adapted accordingly. **If your super-computer supports batch submission, please do not use the mpiexec command shown above**. The command shown above will usually start up HINT on the cluster's login nodes, which will most likely drain significant amounts of CPU cycles and RAM from the node. Your IT will not like it! (I speak from experience here).

B.4 Interpreting the output files

Depending on the selected output file types, after HINT has finished executing, you will now find the following files in the working directory:

- A CSV file corresponding to the name requested in *fopen_stepb/historyb_file*
- A number of *snapfile.{step no.}.nc* or *snapfile.{step no.}* files containing the equilibrium snapshots, depending on whether the code was configured to use netCDF or FORTRAN-type output files. Only the netCDF format is discussed further.

An example netCDF format summarized by ncdump is shown below:

```
[user@node workdir]$ ncdump -h snapfile.80.nc
netcdf snapfile.80
{
dimensions:
       R = 256 ;
       Z = 256 ;
       phi = 128 ;
variables:
       int kstep ;
       double time ;
       int mtor ;
       double rminb ;
       double rmaxb ;
       double zminb ;
       double zmaxb ;
       double B_R(phi, Z, R) ;
       double B_phi(phi, Z, R) ;
       double B_Z(phi, Z, R) ;
       double v_R(phi, Z, R) ;
       double v_phi(phi, Z, R) ;
       double v_Z(phi, Z, R) ;
       double P(phi, Z, R) ;
}
```

- *kstep* and *time* hold information about the macrocycle step number and the time at the end of the macrocycle (defined by the time stepping in the magnetic relaxation step)
- *mtor*, *rminb*, *rmaxb*, *zminb*, *zmaxb* contain the toroidal symmetry and the extent of the calculation domain as usual
- *B_R*, *B_Z* and *B_phi* hold the magnetic equilibrium field.
- *v_R*, *v_Z*, and *v_phi* hold the plasma flow of the equilibrium. Note that this field usually does not correspond to the physical plasma flow, as the resistivity and viscosity (which are irrelevant for the equilibrium itself) are artido not correspond to their physical counterparts.